Exploring the electronic and optical properties of semiconducting graphene

Brun, Søren Jacob

DOI (link to publication from Publisher):
10.5278/vbn.phd.engsci.00184

Publication date:
2016

Document Version
Publisher's PDF, also known as Version of record

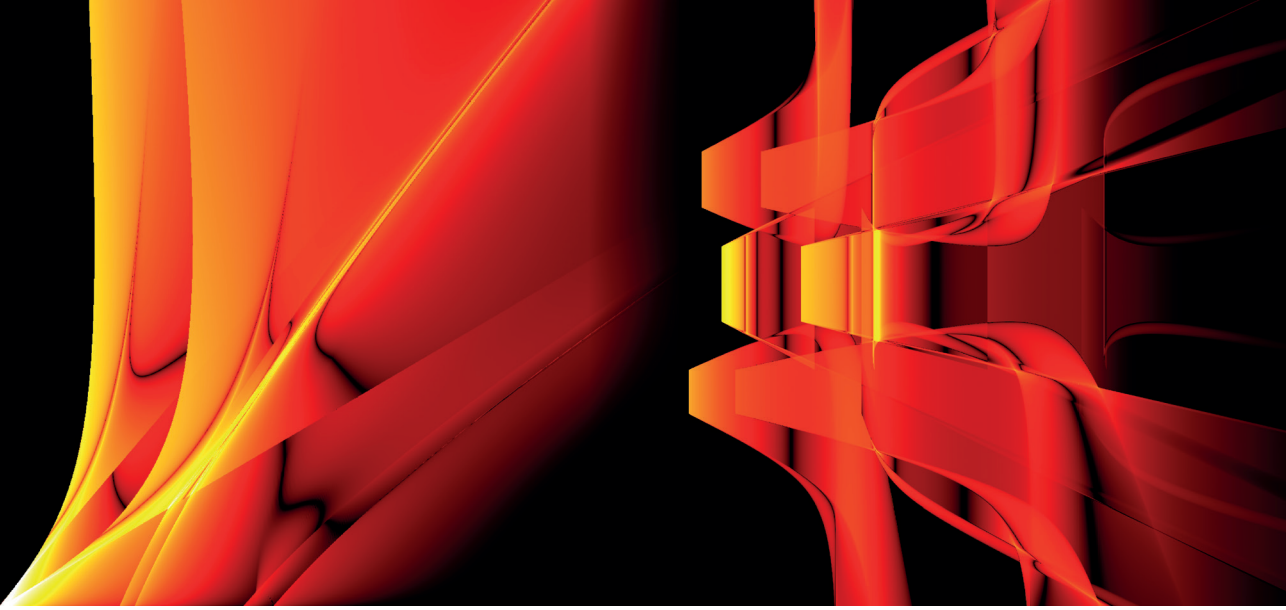

EXPLORING THE ELECTRONIC AND OPTICAL PROPERTIES OF SEMICONDUCTING GRAPHENE

BY
SØREN JACOB BRUN

DISSERTATION SUBMITTED 2016

AALBORG UNIVERSITY
DENMARK

Exploring the electronic and optical properties of semiconducting graphene

Søren Jacob Brun

Department of Physics and Nanotechnology
Aalborg University

AALBORG UNIVERSITY
DENMARK

Dissertation submitted:	September 2016
PhD supervisor:	Prof. Thomas Garm Pedersen, Aalborg University
PhD committee:	Associate Professor Esben Skovsen (chairman) Aalborg University
	Professor Friedhelm Bechstedt Friedrich-Schiller-University of Jena
	Professor Niels Asger Mortensen DTU – Technical University of Denmark
PhD Series:	Faculty of Engineering and Science, Aalborg University

ISSN (online): 2246-1248
ISBN (online): 978-87-7112-806-2

Published by:
Aalborg University Press
Skjernvej 4A, 2nd floor
DK – 9220 Aalborg Ø
Phone: +45 99407140
aauf@forlag.aau.dk
forlag.aau.dk

Printed in Denmark by Rosendahls, 2016

Abstract

The two-dimensional material graphene consists of a single atomic layer of carbon arranged in a honeycomb lattice. This material has attracted tremendous attention since it was discovered in 2004 due to its remarkable electronic and optical properties. However, developing new nanoelectronic devices based on graphene requires experimental studies together with a thorough theoretical understanding in order to fully exploit the properties of the material.

The focus of this thesis is on simulations of the electronic properties of nanostructured graphene and the optical properties of bilayer graphene. The Dirac approximation is used to construct a continuum description of graphene antidot lattices (GALs) and graphene antidot barriers, where an analysis shows good agreement for armchair-edged antidots when compared with tight-binging results. The advantage of this model is that it is scale invariant, meaning that structures of any size may be evaluated without adding computational difficulty. The disadvantage is that all atomistic features are missing from the model, and consequently the localized states on zigzag edges may lead to discrepancies between the models for such systems.

GALs are technologically interesting, as they may turn graphene from a semimetal to a semiconductor. In that connection, doping is investigated for a GAL to study the activation energy for different doping parameters. A Green's function method is developed for efficiently calculating the activation energy of completely isolated dopants, and disorder is found to only slightly affect the properties at moderate doping concentrations.

Furthermore, the stability and magnetization of monolayer iron formed in a graphene pore is studied using density functional theory. It is found that small iron membranes may form a square lattice and keep a high magnetization even for membranes consisting of just a few atoms. The second-harmonic response of biased bilayer graphene is also investigated, and it is found that this shows a strong response that is tunable by the strength of the electric field.

Resumé

Det todimensionelle materiale grafen består af et enkelt atomlag af kulstof, som er arrangeret i et bikubemønster. Dette materiale har tiltrukket enorm interesse siden det blev opdaget i 2004 på grund af dets usædvanlige elektroniske og optiske egenskaber. Udviklingen af nye grafenbaserede nanoelektroniske komponenter kræver både eksperimentelle studier og en grundig teoretisk forståelse for fuldt at kunne udnytte dets egenskaber.

Denne tese er fokuseret på simuleringer af elektroniske egenskaber af nanstruktureret grafen og optiske egenskaber af dobbeltlag grafen. Dirac approksimationen benyttes til at konstruere en kontinuumbeskrivelse af hullet grafen og barrierer af hullet grafen, hvor en analyse viser god overensstemmelse med tight-binding resultater for huller med lænestolskanter. Fordelen ved denne model er at den er uafhængig af strukturens skala, hvilket vil sige at man kan studere systemer af vikårlig størrelse uden at øge beregningsvanskeligheden. Ulempen er at alle atomistiske detaljer mangler i modellen, og derfor kan lokaliserede tilstande på zigzagkanter føre til uoverensstemmelser mellem modellerne for sådanne systemer.

Hullet grafen er teknologisk interessant, da det kan ændre grafen fra at være halvmetallisk til at være halvledende. Derfor undersøges dotering i hullet grafen for at studere aktiveringsenergien for forskellige doteringsparametre. En metode baseret på Greens funktioner er blevet udviklet til effektivt at beregne aktiveringsenergien for fuldstændigt isolerede dopanter, og uorden ved moderate doteringskoncentrationer viser sig kun at påvirke egenskaberne i lille grad.

Ydermere undersøges stabiliteten og magnetiseringen af monolag jern, der dannes i grafen nanoporer, ved hjælp af tæthedsfunktionalteori. Små jernmembraner kan dannes i et kvadratisk gitter og bevare en høj magnetisering selv for membraner, der kun består af få atomer. Det andenharmoniske respons fra dobbeltlag grafen er også undersøgt, og det viser at der er et kraftigt respons, der kan justeres ved at ændre på styrken af det vinkelrette elektriske felt.

Contents

Thesis Details

Thesis Title:	Exploring the electronic and optical properties of semiconducting graphene
PhD Student:	Søren Jacob Brun
Supervisor:	Professor Thomas Garm Pedersen, Aalborg University

This thesis is based on the following papers.

[I] **S. J. Brun**, M. R. Thomsen and T. G. Pedersen, "*Electronic and optical properties of graphene antidot lattices: comparison of Dirac and tight-binding models,*" Journal of Physics: Condensed Matter, **26**, 265301 (2014).

[II] M. R. Thomsen, **S. J. Brun** and T. G. Pedersen, "*Dirac model of electronic transport in graphene antidot barriers,*" Journal of Physics: Condensed Matter, **26**, 335301 (2014).

[III] M. R. Thomsen, **S. J. Brun** and T. G. Pedersen, "*Stability and magnetization of free-standing and graphene-embedded iron membranes,*" Physical Review B, **91**, 125439 (2015).

[IV] **S. J. Brun** and T. G. Pedersen, "*Intense and tunable second-harmonic generation in biased bilayer graphene,*" Physical Review B, **91**, 205405 (2015).

[V] **S. J. Brun**, V. M. Pereira and T. G. Pedersen, "*Boron and nitrogen doping in graphene antidot lattices,*" Physical Review B, **93**, 245420 (2016).

This thesis has been submitted for assessment in partial fulfillment of the PhD degree. The thesis is based on the published scientific papers which are listed above. Parts of the papers are used directly or indirectly in the extended summary of the thesis. As part of the assessment, co-author statements have

been made available to the assessment committee and are also available at the Faculty. The thesis is not in its present form acceptable for open publication but only in limited and closed circulation as copyright may not be ensured.

Preface

This thesis summarizes my research as a PhD student in the period $2013-2016$ at the Department of Physics and Nanotechnology, Aalborg University, under the supervision of Professor Thomas Garm Pedersen. The research has been carried out as part of the Center for Nanostructured Graphene (CNG). Working in a large group has been a great experience, and in spite of the distance to the main facilities, frequent meetings have lead to great discussions.

My time as a PhD student would have been much less enjoyable without the help and support from many people. First of all, I would like to thank my supervisor Thomas Garm Pedersen. You have inspired me to pursue research ever since I attended your courses as an undergraduate. I really appreciate your visit during my stay in Singapore, where our bike trip around Pulau Ubin with many animal encounters will not be forgotten. I would also like to thank CNG leader Professor Antti-Pekka Jauho for the assistance in setting up an exchange programme with the National University of Singapore (NUS) that facilitated my stay abroad. Furthermore, Professor Vitor Manuel Pereira at NUS deserves a special thanks for his hospitality and for many useful discussions. I wish to thank my office-mate Morten Rishøj Thomsen for our joint work on our master's thesis and for always being helpful in any way possible. We have had many good discussions on research-related as well as non-scientific topics. René Petersen has also contributed greatly to a pleasant atmosphere in the office, and I really enjoyed our time when I visited you in Barcelona. I would like to thank Farzad Bonabi for our workout routine that has given us a nice break from work and for enjoying a beer together every now and then. Last, but not least, I would like to thank my family and friends for supporting me during this time. I hope you all know how much I appreciate your company.

Søren Jacob Brun
Aalborg, September 2016

Chapter 1

Introduction

Graphene is a two-dimensional (2D) material consisting of a single atomic layer of carbon atoms arranged in a honeycomb lattice. It was discovered quite recently and has lead to a plethora of research within graphene and other 2D materials. The first graphene samples were fabricated in 2004 by Andre Geim and Kostya Novoselov by exfoliating layers from a bulk sample [1]. The bulk material used was highly oriented pyrolytic graphite (HOPG) which consists of numerous stacked graphene layers. Their exfoliation method was extremely simple and consisted of first using scotch tape to pull off a thin layer of graphite from the HOPG and then continue the cleaving process with scotch tape until only a single atomic layer remained. Their discovery of this new material earned them the Nobel Prize in physics in 2010.

Mechanical exfoliation provides high-quality graphene samples, but the drawback is the high price and small sample size. Other methods have been developed for fabricating graphene in larger sheets. The most prevalent method is chemical vapor deposition (CVD) of some carbon source, usually methane, on metal films, which produces large areas of graphene, however, with a much higher degree of defects than mechanically exfoliated graphene. The CVD procedure is often carried out on copper foil, as this can lead to large areas of monolayer graphene [2, 3]. CVD growth of graphene on metals such as copper and nickel was discovered quite recently and began in 2008 [2–7]. However, CVD on nickel has been reported as far back as 1966 to produce thin ($\sim$50 nm) crystalline graphite films [8]. Graphite and graphene have also been interesting for theoretical studies for a long time, where the band theory was investigated as far back as 1947 [9].

The discovery of graphene has also triggered a wealth of research in other layered materials which are suited for producing monolayers via mechanical exfoliation or CVD. The most widely studied materials are the transition metal dichalcogenides (TMDs), where the unit cell consists of a transition metal atom, such as molybdenum or tungsten, and two chalcogen atoms, such as sulfur or selenium. The most popular of these TMDs is molybdenum disulfide MoS_2 [10–13], but e.g. tungsten disulfide WS_2 [14, 15] and molybdenum diselenide $MoSe_2$ [16, 17] are also being studied intensely. The list of 2D materials is constantly expanding, and monolayers of phosphorus (phosphorene), silicon (silicene), germanium (germanene) and tin (stannene) are also attracting a lot of interest in the research society [18–21].

After the discovery of graphene, research quickly lead to measurements of several impressive and intriguing properties. Among other, the ultra-high mobility (excess of 200,000 $\mathrm{cm^2\,V^{-1}\,s^{-1}}$) [1, 22], the half-integer quantum Hall effect [23, 24], the high transparency [25] and its record-breaking mechanical strength [26] are very remarkable properties. Especially the electronic and optical properties make it a promising material for electronic and optoelectronic devices, e.g. transistors with high on/off ratios for logic applications. However, the major problem is that graphene in its pristine form is semimetallic and therefore not directly suitable for semiconductor applications. One great challenge has therefore been to find a method for introducing a band gap in graphene while preserving as much as possible its intrinsic characteristics. One way is to use biased bilayer graphene (BLG) where a perpendicular electric field breaks the sublattice symmetry of the graphene layers and induces a band gap. It has been shown both theoretically [27–29] and experimentally [28–32] that this can lead to band gaps of a few hundred meV. The band gap is tunable depending on the strength of the electric field and measurements have shown values up to 250 meV [31]. This method has even been used to demonstrate a working field-effect transistor at room temperature [33]. Another proposal for opening a band gap is to periodically gate the graphene in two dimensions. Unfortunately, for realistic gating profiles, this was found to not open a band gap large enough for practical applications [34]. Alternatively, an energy gap may be created using graphene quantum dots, or graphene nanodisks, which also show promising results as hosts for spin qubits [35–38].

A more promising method for creating a band gap is based on restricting graphene in one direction, meaning that it is cut into thin strips called graphene nanoribbons (GNRs). Such systems were studied both theoretically [39, 40]

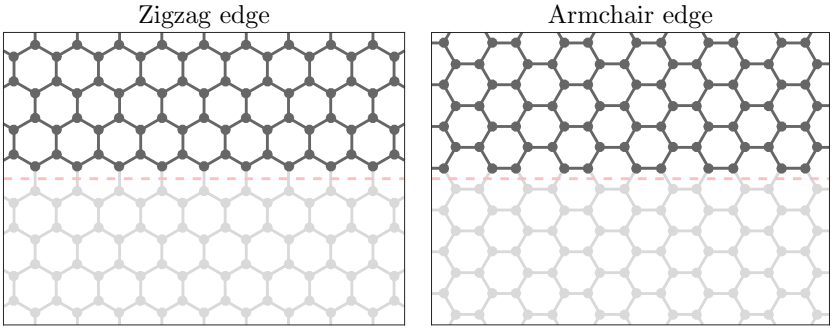

Fig. 1.1: Graphene cut perpendicular to the bonds results in zigzag edge type (left panel) while graphene cut parallel to bonds results in armchair edge type (right panel).

and experimentally [41] soon after graphene was discovered. Depending on the edge type, there are two basic kinds of GNRs, namely armchair-edged GNRs, where graphene is cut parallel to carbon bonds, and zigzag-edged GNRs, where graphene is cut perpendicular to carbon bonds, see Fig. 1.1. Ribbons with intermediate edge types are called chiral. It has been predicted theoretically that zigzag-edged GNRs always have a band gap, while it was shown that every third armchair-edged GNR is metallic [40]. Han *et al.* [41] have investigated the band gap dependence on the ribbon width experimentally. They measured the transport properties of lithographically fabricated GNRs with different widths and found an inverse relation in agreement with theoretical studies [40, 41].

Another promising and widely studied method is to periodically modify graphene in two dimensions. One route is hydrogen adsorption onto graphene on an iridium surface, which has been shown experimentally to create a periodic pattern and open a band gap [42]. A more investigated method for creating a tunable band gap in graphene is by introducing nanoscale perforations in a periodic fashion, known as graphene antidot lattices (GALs) or graphene nanomeshes [43–45]. Examples of such structures are shown in Fig. 1.2. The magnitude of the band gap depends on the size of the antidots, size of the unit cell and on edge chirality [43, 46–48]. It has been shown theoretically that the band gap of GALs with relatively small antidots follows a simple scaling rule [43]. Other studies have investigated other antidot lattice geometries [49, 50]. It was found that while regular GAL structures are always semiconducting [43], so-called rotated GALs are only semiconducting for every third lattice [50]. Furthermore, a universal rule based on tight-binding (TB) determining if a given GAL is metallic or semiconducting has been presented [51].

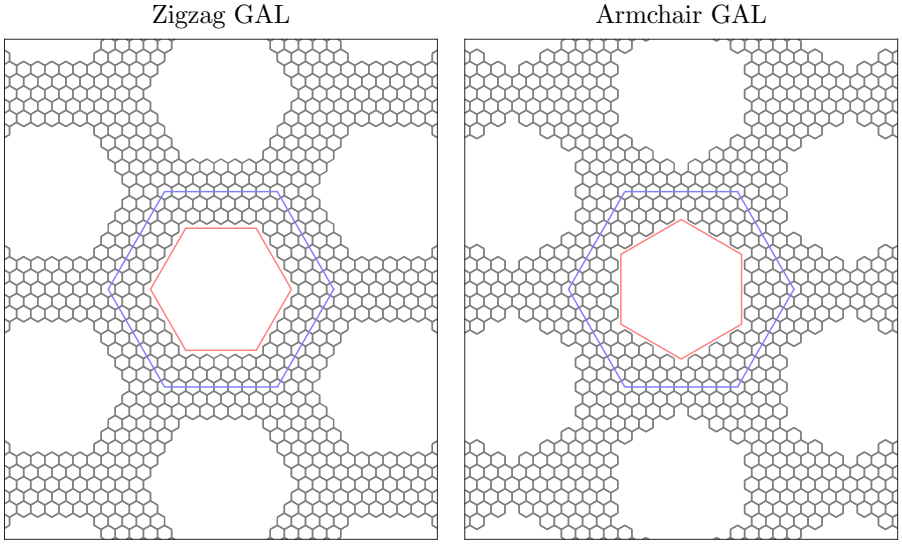

Fig. 1.2: Examples of graphene antidot lattices, where the holes have either zigzag (left panel) or armchair (right panel) edges. Blue hexagons mark the unit cells of the structures and red hexagons mark the antidot region within which all atoms are removed.

One parameter that has a great effect on the band gap of GALs is the edge chirality of the holes. Continuous segments of zigzag edges have been shown to give rise to localized edge states, which significantly quench the band gap [47]. Edge states in graphene are known from GNRs with zigzag edges [52, 53] and has even been shown experimentally by scanning tunneling spectroscopy measurements [54]. Vanević *et al.* [47] have shown that GALs with triangular zigzag-edged antidots give rise to flat bands, while Trolle *et al.* [48] have used density functional theory (DFT) and Hubbard TB to show that localized edge states emerge in GALs containing hexagonal antidots with zigzag edges.

Lattices obtained experimentally are typically much larger than the theoretically studied ones. Graphene has an unusual linear dispersion around the Fermi level, which has lead to a simplified theoretical description called the Dirac approximation, as electrons in graphene behave as massless Dirac fermions. Fürst *et al.* [45] have presented an analysis based on the Dirac equation (DE), in which they used finite-element analysis to calculate the electronic properties of GALs with circular antidots. This model is a continuum approximation, meaning that GALs of arbitrary size may be treated, however, with the drawback that all atomistic features are omitted. The computational time of their method depends only on the ratio between the radius of the antidot

and the size of the unit cell. Although they find reasonable agreement with TB, their method only qualitatively predicts the band structure.

Several methods have been used to produce GALs experimentally, including e-beam lithography [55, 56], diblock copolymer templates [57–59], anodic aluminum oxide templates [60], nanosphere lithography [61] and nanoimprint lithography [62]. Depending on the fabrication method, the antidots range in size between a few dozen and several hundred nanometers. Very small antidots with diameters down to 2 nm may be fabricated using a scanning transmission electron microscope [63]. However, this is a very time-consuming method and is not suited for large scale production. Antidots synthesized in experiments are often round, but it has been demonstrated experimentally that armchair and zigzag edges in GALs are stable and can be synthesized selectively [64–66]. Oberhuber *et al.* [64] have used an etching technique that selectively etches armchair edges to produce GALs with hexagonal antidots with zigzag edges. Joule heating has also been shown to reconstruct graphene edges into either zigzag or armchair configurations [65]. Theoretical studies based on DFT show that GNRs in an oxygen-rich atmosphere leads to armchair edges, while water-saturated GNRs have zigzag edges [67]. Although some edge roughness may still remain, this shows that the edge chirality of GNRs and GALs is controllable to some degree. Furthermore, transport gaps have been measured by Eroms *et al.* [58] of 6 meV and by Kim *et al.* [55] of 102 meV in GALs produced using e-beam lithography.

The electronic transport properties of GALs have also been studied both experimentally and theoretically. Experimental studies of transport in GALs have shown on/off ratios in the range between 4 and 100 [57, 60, 62]. Such ratios are still not high enough for logic applications [68], but the results indicate that devices based on GALs could be used to make efficient transistors. Theoretically, the transport through graphene antidot barriers (GABs), i.e. pristine graphene with one-dimensional periodic antidot structures, has been studied using a TB formalism for small systems [69, 70]. In these studies, it was shown that GABs with unit cells containing just a few antidots suppress the transport for energies within the band gap. Electronic waveguides have also been modeled by exploiting the suppressed transport in antidot regions [71]. In that case, a transport channel of pristine graphene is used as a guide for electrons in a GAL structure. Their results show that the conductance of GAL waveguides is higher than corresponding GNRs. Furthermore, Berreda *et al.* [72] have simulated three different graphene field-effect transistors based

on GALs with band gaps of about 500 meV. Their simulations showed that such devices had on/off ratios as high as 7400, which is not far from the value $10^4 - 10^7$ that silicon based MOSFETs show [68].

One major problem when fabricating graphene nanostructures using top-down methods, such as e-beam lithography, is the inevitable disorder. Fabricating GNRs along this route can lead to scattering of electrons from edge imperfections, which has been shown to degrade the transport properties [73, 74]. An alternative way of fabricating GNRs is by unzipping carbon nanotubes, which produces much more regular edges [75, 76]. Nevertheless, the exact edge chirality of such GNRs is still hard to control and disorder could still pose a problem to the electronic properties. The same applies for GALs, which also lack full periodicity when fabricated using top-down methods. This has been shown theoretically to be problematic with respect to the electronic properties of GALs, as the band gap vanishes or is significantly lowered [77]. Transport calculations support this finding and show that leakage currents can form through disordered graphene antidot devices [78].

A promising strategy for overcoming the problematic disorder is to fabricate the nanostructures using bottom-up self-assembly. However, research in bottom-up fabrication of graphene nanostructures is still limited. Nonetheless, such methods have actually been utilized by several groups to synthesize atomically precise graphene nanostructures. GNRs and chevron-shaped GNRs, so-called graphene nanowiggles (GNWs), have been fabricated using surface-assisted coupling of two different precursors on an Au(111) surface followed by cyclodehydrogenation [79]. This yielded narrow, fairly long GNRs and GNWs on the surface. Other versions of the GNW precursor with pyridine-like nitrogen at one or two edge sites have been used to fabricate doped GNWs [80] as well as GNW heterojunctions and heterostructures [81]. These structures were studied theoretically by Lherbier *et al.*, who found reasonably high mobilities [82]. Bottom-up methods have also been used to fabricate 2D graphene structures. A nitrogenated GAL with C_2N stoichiometry has been synthesized with a measured band gap of 1.96 eV [83] and a BN-substituted heteroaromatic network has been fabricated using another precursor [84]. Finally, the precursor hexaiodo-substituted macrocycle cyclohexa-m-phenylene has been used by Bieri *et al.* [85] to produce a GAL on an Ag(111) surface with sub-nanometer periodicity. These results on bottom-up fabrication of atomically precise and even doped structures are promising results for overcoming the problem of disorder from top-down methods. Despite the high level of control on the atomic

scale, these methods still have some drawbacks. Grain boundaries occur between domains in the crystal, and the structures should be transferred after synthesis because this takes place on metal surfaces.

As mentioned above, doping in bottom-up fabricated graphene nanostructures has drawn interest in the recent years. However, other methods are also being pursued for doping graphene. Usual dopants are boron and nitrogen, as they fit in the lattice easily, but other types of doping have also been studied, such as aluminum, sulfur and phosphorus [86]. Furthermore, nitrogen doped carbon nanotubes [87] and GNRs [88] have been realized experimentally. Graphene doped with nitrogen has been synthesized from CVD using various precursors [89, 90]. Doping in graphene has been studied theoretically to some extent, e.g. transport properties and unbalanced sublattice doping [91, 92]. Theoretical studies of isolated boron and nitrogen dopants in graphene and near graphene edges have also been carried out [93, 94]. Doping in GNRs has been studied theoretically to a large extent [95–98]. The most stable configuration of boron and nitrogen was found to be at the edges of the ribbon, where nitrogen would be either pyridine- or pyridinium-like.

Another subject that will be discussed in this thesis is the magnetic properties of graphene, specifically iron membranes in graphene pores. Several strategies have been suggested on how to give the non-magnetic pristine graphene magnetic properties DFT calculations have shown that graphene can become ferromagnetic by e.g. semi-hydrogenation [99], adding vacancies [100, 101] or adding adatoms [101–106]. Fully hydrogenating only one sublattice leads to an imbalance, which induces a magnetic moment of 1 μ_B per unit cell [99]. Recent experimental results by Zhao *et al.* [107] show that monolayer iron membranes can form in graphene nanopores. These monolayer membranes both form and collapse under e-beam irradiation while imaged in a transmission electron microscope. The iron is provided via leftover residue from the transfer process, where graphene is transferred from growth substrate to target substrate. They find that the iron forms membranes in a square lattice with a lattice constant of about 2.65 Å. These ferromagnetic iron membranes combined with the electrical properties of graphene, might make this a suitable system for graphene-based spintronics.

Graphene systems have also been studied optically using theoretical models and experimental setups. Pristine graphene was shown experimentally to absorb 2.3 % of the incident light [25]. This shows a very high transparency, yet graphene absorbs a significant amount of light when considering that it is a

single atomic layer. The optical properties of gapped graphene (graphene with broken sublattice symmetry from a mass term) and GALs have also been studied theoretically [108, 109], and biased BLG has shown tunable optical properties both theoretically and experimentally [28, 29, 32]. Another topic that will also be discussed in this thesis is nonlinear optics with focus on second-harmonic generation (SHG). Dipole-allowed even order optical processes, such as SHG, require materials that are non-centrosymmetric. SHG in the 2D materials MoS_2, WS_2 and WSe_2 has been demonstrated and used to identify grain boundaries and crystal lattice orientation in polycrystalline samples [110–115]. This shows that SHG may act as a useful noninvasive characterization method for atomically thin samples. Calculations of SHG in MoS_2 have been compared to experiments with good agreement [116]. SHG has also been studied theoretically in carbon nanotubes, where the it was shown to depend strongly on diameter and chirality [117]. Monolayer graphene does not show any dipole-allowed SHG as it has inversion points at hexagon centers and between neighbor atoms. However, graphene has been shown theoretically to display SHG when the valley symmetry is broken [118]. Furthermore, theoretical studies of SHG from graphene at oblique incidence of radiation have shown large values when compared with typical 2D semiconductor structures [119]. Strong third-harmonic generation (THG) has been measured from monolayer graphene, and it was reported that the SHG from the same sample was two orders of magnitude lower than the THG [120]. BLG is also centrosymmetric with an inversion point between the two layers, meaning that it does not show strong SHG unless the symmetry is broken, which may be achieved by applying a perpendicular electric field. The nonlinear optical properties of BLG have only been studied to a limited extent. Wu *et al.* [121] have used a Dirac model description to study SHG in BLG and find that it shows SHG when an in-plane current is included in order to break the symmetry. They also found that the second-harmonic (SH) susceptibility is zero when omitting the in-plane current even with a non-vanishing perpendicular electric field, and argue that the contributions from opposite momenta (K and K' valleys) cancel.

The focus of this thesis is on the electronic and optical properties of nanostructured graphene and BLG. This is a purely theoretical study, which means that various numerical methods have been used to calculate the physical properties of the systems. The thesis is organized as follows. In Chap. 2 the main theoretical models and methods used for the calculations are outlined. Chapter 3 summarizes the results from the papers found at the end of the thesis.

This chapter is further divided into several sections concerning different topics. First, the electronic properties of GALs are described using the DE and compared with TB. Second, the transport properties of GABs are described using the DE and also compared with TB. Then the effect of doping in GALs is studied using DFT and TB. The fourth section concerns the stability and magnetic properties of graphene-embedded iron membranes. Finally, the SH optical response from biased bilayer graphene is studied. Chapter 4 sums up the conclusions from this study and, as mentioned earlier, all papers for this thesis are collected at the end of the thesis.

Chapter 2

Theory and methods

Different theoretical methods and models with varying accuracies have been used to produce the results presented in this thesis. This chapter contains brief descriptions of these methods including their advantages and disadvantages. Additionally, the theory will be applied to the case of graphene and a comparison of the band structure will be presented.

1 Density functional theory

As the technology has advanced in recent years, especially within computer power, so has the possibilities for exploring physical properties of materials computationally. One very important tool within condensed matter physics is density functional theory (DFT). This method is *ab initio* or "first principles", meaning that it fundamentally does not rely on any assumptions or fitting parameters. The theory of DFT is based on the two Hohenberg-Kohn theorems [122]. The first theorem shows that the electron density uniquely determines the Hamiltonian operator, and consequently the ground state of the system is a unique functional of the electron density. This leads to a great reduction in complexity, and facilitates studies of much more complicated structures. The second theorem states that minimizing the energy as a functional of the electron density leads to the correct electron density of the ground state. The theory was further improved in the Kohn-Sham framework, where a set of self-consistent equations are used to solve for the electron density [123]. Here, the system is modeled as a set of non-interacting electrons moving in an effective potential background which is a functional of the electron density. This

method is also useful for calculating the total energy of the system. A pseudopotential is normally used for such calculations to reduce the computational effort needed [124]. The physical properties of solids mostly depend on the valence electrons and are only affected by the core electrons to a limited extent. For this reason, most DFT calculations only include valence electrons and replace the core electrons and ionic potential by a pseudopotential.

Even though DFT has proven to be a strong tool for solid state physics, a few problems still remain. Although DFT is "first principles", the energy functional, specifically the exact functionals for exchange and correlation, are not known [125]. In stead, approximations are used for these functionals, such as the local density approximation (LDA) where the functional depends only on the density at the point it is evaluated. Furthermore, DFT is a ground state calculation and it does therefore not accurately describe states at higher energies. This means that especially the energies of the conduction bands may differ from what is observed experimentally, leading to the well-known band gap problem when describing semiconductors. Experimental results from e.g. photoemission and optical absorption show that the band gap from DFT can be much too small [126, 127]. For silicon, the DFT band gap is only half of the experimentally observed value. The model may be expanded by the GW approximation [128] or using hybrid functionals [129] to describe this much more accurately, and even more accurate methods, such as quantum Monte Carlo [130], exist for describing the physical properties of solids.

DFT software needs several input parameters for defining the calculation. Convergence should be ensured in e.g. the size of the basis and number of k-points. DFT has been widely used to explore electronic and optical properties of solids in the last decades, and today there is plenty of software packages available for performing DFT calculations, such as VASP, ABINIT and SIESTA.

2 Tight-binding

Another approach for calculating physical properties of solids is the tight-binding (TB) model, which is much simpler than DFT, yet rather accurate [131]. In this model, the total wave function is approximated as a linear combination of atomic orbitals. In some cases, this may be simplified even further by only considering certain orbitals [131]. Because of its structure, it is only necessary to consider a single π orbital for graphene. This significantly lowers the computational cost, which means that a TB description of graphene is able to handle much more complicated systems than DFT.

The atomic orbitals ϕ satisfy the Schrödinger equation with the atomic Hamiltonian $H_{at}\phi_n = E_n\phi_n$. The electronic states are expanded as Bloch functions [131]

$$\Phi_n(\mathbf{r}) = \frac{1}{\sqrt{N}} \sum_{\mathbf{R}} e^{i\mathbf{k}\cdot\mathbf{R}} \phi_n(\mathbf{r}-\mathbf{R}), \tag{2.1}$$

which satisfy Bloch's theorem. The wave function is now described by a linear combination of Bloch functions

$$\psi(\mathbf{r}) = \sum_n b_n \Phi_n(\mathbf{r}), \tag{2.2}$$

where b_n are the expansion coefficients. The problem is then turned into a matrix equation by inserting the wave function in the Schrödinger equation $H\psi = E\psi$, multiplying by $\Phi_m^*(\mathbf{r})$ from the left and integrating over space. This yields the matrix equation

$$\sum_n H_{mn} b_n = E \sum_n S_{mn} b_n, \tag{2.3}$$

which is easily solved for eigenvalues once H_{mn} and S_{mn} are known. The Hamilton matrix elements are given by

$$H_{mn} = \int \Phi_m^*(\mathbf{r})\, H\, \Phi_n(\mathbf{r})\, d\mathbf{r}. \tag{2.4}$$

Inserting Eq. 2.1 in Eq. 2.4 and exploiting that the matrix element only depends on $\mathbf{R}_n - \mathbf{R}_m = \mathbf{R}$ because of periodicity (meaning that one sum disappears giving a factor of N) leads to

$$H_{mn} = \sum_{\mathbf{R}} e^{i\mathbf{k}\cdot\mathbf{R}} \int \phi_m^*(\mathbf{r})\, H\, \phi_n(\mathbf{r}-\mathbf{R})\, d\mathbf{r} = \sum_{\mathbf{R}} e^{i\mathbf{k}\cdot\mathbf{R}}\, t(\mathbf{R}). \tag{2.5}$$

Here, the so-called hopping matrix element $t(\mathbf{R})$ and, analogously from the right-hand side of Eq. 2.3, overlap matrix element $s(\mathbf{R})$ are given by

$$\begin{aligned} t(\mathbf{R}) &= \int \phi^*(\mathbf{r})\, H\, \phi(\mathbf{r}-\mathbf{R})\, d\mathbf{r}, \\ s(\mathbf{R}) &= \int \phi^*(\mathbf{r})\, \phi(\mathbf{r}-\mathbf{R})\, d\mathbf{r}. \end{aligned} \tag{2.6}$$

TB models of solids rely on these hopping and overlap parameters, which are normally obtained by fitting some physical property, e.g. the band structure, to experimental data or DFT results. Because the interaction decays with the distance between atoms, it is only necessary to include interactions up to

some distance in the TB model. Many models include only nearest neighbors and even neglect overlap between atoms (orthogonal approximation), which in many cases is sufficient for a satisfactory description. Other models include up to third nearest neighbors with non-zero overlap elements, which provides a more accurate description of the material.

For graphene, the TB model takes a quite simple form because of its planar structure leading to sp^2 hybridization. In this configuration, the 2s and two 2p orbitals hybridize and are used for the network of bonds, leaving only the third 2p orbital unhybridized. The nearest neighbor Hamiltonian and overlap matrices for graphene are given by [108, 132]

$$\begin{aligned} \mathbf{H} &= \begin{pmatrix} 0 & -t\, f(\mathbf{k}) \\ -t\, f^*(\mathbf{k}) & 0 \end{pmatrix}, \\ \mathbf{S} &= \begin{pmatrix} 1 & s\, f(\mathbf{k}) \\ s\, f^*(\mathbf{k}) & 1 \end{pmatrix}, \end{aligned} \tag{2.7}$$

where $f(\mathbf{k}) = \exp\left(ik_x \frac{a}{\sqrt{3}}\right) + 2\exp\left(-ik_x \frac{a}{2\sqrt{3}}\right)\cos\left(k_y \frac{a}{2}\right)$ and a is the graphene lattice constant.

Graphene is semimetallic, but may be phenomenologically be turned into a semiconductor by breaking the sublattice symmetry. This is called gapped graphene, and requires the addition of a mass term Δ such that the Hamiltonian becomes [108]

$$\mathbf{H} = \begin{pmatrix} \Delta & -t\, f(\mathbf{k}) \\ -t\, f^*(\mathbf{k}) & -\Delta \end{pmatrix}. \tag{2.8}$$

It may easily be shown that this leads to a band gap of $E_g = 2\Delta$.

3 Dirac approximation

The band structure at the K-point of the Brillouin Zone is linear around the Fermi level. This entails that electrons behave as massless Dirac fermions in graphene. The Dirac model is based on approximating the band structure in the low-energy regime. This is carried out by expanding $f(\mathbf{k})$ around the K-point, which leads to the Dirac Hamiltonian

$$\mathbf{H} = \hbar v_F \begin{pmatrix} 0 & q_x - iq_y \\ q_x + iq_y & 0 \end{pmatrix}, \tag{2.9}$$

where $v_F = \sqrt{3}\, a\, t/(2\hbar) \simeq c/300$ is the Fermi velocity and $\mathbf{q} = \mathbf{k} - \mathbf{K}$.

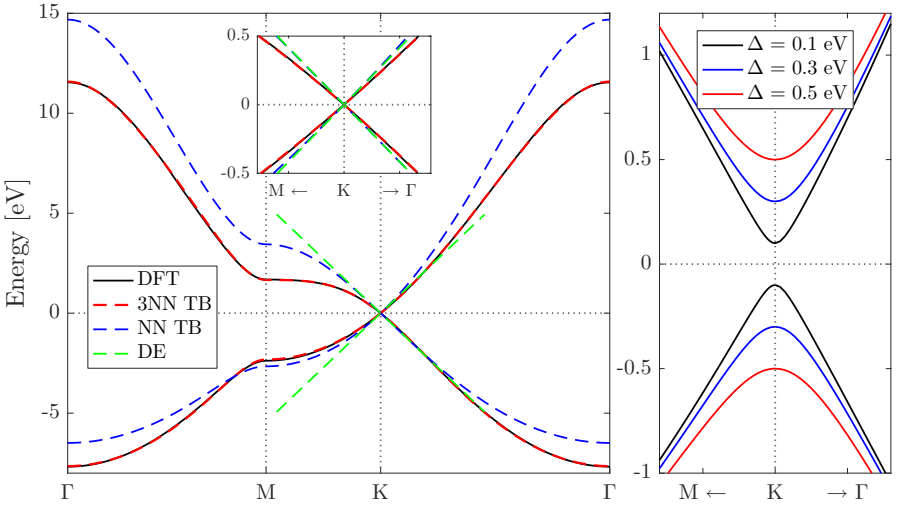

Fig. 2.1: Band structures of pristine graphene (left panel) calculated using DFT, TB and the DE. The non-orthogonal third nearest neighbor TB (3NN TB) is obtained by fitting to DFT. The nearest neighbor TB (NN TB) is calculated using $t = 3$ eV and $s = 0.129$. The band structure of gapped graphene (right panel) near the K-point is shown for different values of the mass term.

Figure 2.1 shows a comparison of the band structure of graphene from the different models. DFT is the most accurate model and is used for fitting the parameters of the TB models. The nonorthogonal third nearest neighbor TB model almost coincides with the DFT result and thus describes the entire band structure well. The nonorthogonal nearest neighbor TB model deviates at energies far away from the Fermi level, but still provides a good description at low energies. The Dirac model is sufficient in the linear regime, as seen in the inset, but quickly deviates away form the Fermi level. The right panel shows gapped graphene near the K-point calculated using Eq. 2.8 for different values of the mass term where it is clear that a band gap proportional to the mass term emerges.

4 Dirac model of graphene antidot lattices

The Dirac equation (DE) together with a spatially varying mass term are used to build a continuum model describing graphene antidot lattices (GALs). A band gap is introduced artificially in the model by adding a mass term Δ to the DE. The Hamiltonian then becomes the Dirac Hamiltonian in Eq. 2.9 with an

added mass term as in Eq. 2.8. This leads to energies $E = \pm\sqrt{(\hbar v_F q)^2 + \Delta^2}$, which means that the band gap is $E_g = 2\Delta$. The antidot lattices are modeled by introducing a spatially varying mass term, which is large in the antidot areas and zero elsewhere. Examples of the atomistic structures used in TB and their equivalents for the continuum model are shown in Fig. 2.2. The large mass term means that there are no states available in the antidot region for energies $-\Delta < E < \Delta$, thus mimicking regions with no graphene material. The Dirac Hamiltonian is converted to a real space operator and the spatially varying mass term is added such that

$$\mathbf{H} = \begin{pmatrix} \Delta(\mathbf{r}) & -\hbar v_F \left(i\partial_x - \partial_y\right) \\ -\hbar v_F \left(i\partial_x + \partial_y\right) & -\Delta(\mathbf{r}) \end{pmatrix}, \tag{2.10}$$

where the mass term is Δ_0 inside the antidot and vanishing elsewhere. The wave function satisfies the Bloch condition when described as $\Psi(\mathbf{r}) = e^{i\mathbf{k}\cdot\mathbf{r}}u(\mathbf{r})$, where $u(\mathbf{r})$ is a lattice-periodic spinor. The Schrödinger equation containing the Dirac Hamiltonian now contains two lattice-periodic parts, namely the mass term and the periodic part of the wave function. Both these functions are now expanded as Fourier series with the same periodicity

$$\begin{aligned} \Delta(\mathbf{r}) &= \sum_{\mathbf{G}} \Delta_{\mathbf{G}} e^{i\mathbf{G}\cdot\mathbf{r}}, \\ u(\mathbf{r}) &= \sum_{\mathbf{G}} u_{\mathbf{G}} e^{i\mathbf{G}\cdot\mathbf{r}}. \end{aligned} \tag{2.11}$$

Here, $u_{\mathbf{G}}$ are the Fourier coefficients expressed as a spinor with the elements $u^A_{\mathbf{G}}$ and $u^B_{\mathbf{G}}$, and $\mathbf{G} = p\mathbf{g}_1 + q\mathbf{g}_2$ is the reciprocal lattice vector constructed from the primitive reciprocal lattice vectors $\mathbf{g}_1$ and $\mathbf{g}_2$ of the antidot lattice. The Fourier coefficients of the mass term $\Delta_{\mathbf{G}}$ are determined by the geometry of the antidot. Expressions for the Fourier coefficients of an N-sided polygon is derived in Ref. 133. For a GAL with a hexagonal antidot with zigzag edges (i.e. the top right geometry in Fig. 2.2), this gives the coefficient

$$\Delta_{\mathbf{G}} = \frac{2\sqrt{3}\Delta_0\left[G_- \cos(G_- S/2) + G_+ \cos(G_+ S/2) - 2G_x \cos(G_x S)\right]}{A_{uc} G_x G_- G_+}, \tag{2.12}$$

where $G_\pm = G_x \pm \sqrt{3}G_y$ and S is the side length of the hexagon. For armchair antidots the expression is slightly different, and for circular antidots the coefficients are $\Delta_{\mathbf{G}} = 2\pi R\Delta_0 J_1(GR)/(A_{uc}G)$, where R is the radius of the antidot, J_1 is the first order Bessel function of the first kind, $G = \|\mathbf{G}\|$ and A_{uc} is the

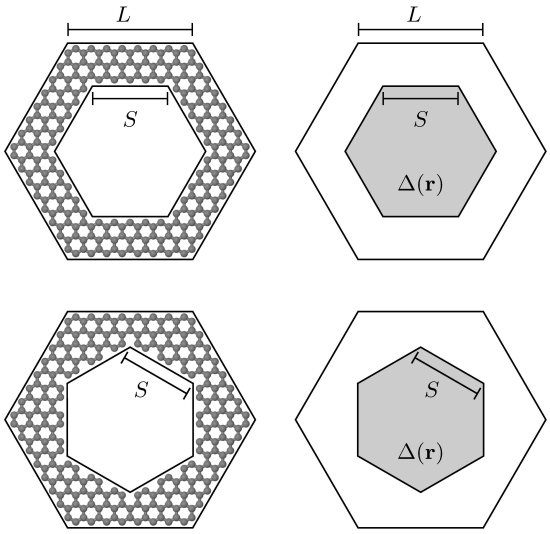

Fig. 2.2: Examples of unit cells used in TB (left) and DE (right) for hexagonal antidots with zigzag (top) and armchair (bottom) edges in triangular antidot lattices.

area of the unit cell. Combining the mass term and wave function in the Dirac equation $\mathbf{H}\Psi = E\Psi$ leads to the following system of equations

$$\begin{aligned} \sum_{\mathbf{G}'} \mathbf{H}_{\mathbf{G},\mathbf{G}'}\, u_{\mathbf{G}'} &= E\, u_{\mathbf{G}}, \\ \mathbf{H}_{\mathbf{G},\mathbf{G}'} &= \begin{pmatrix} \Delta_{\mathbf{G}-\mathbf{G}'} & T_{\mathbf{G}}\delta_{\mathbf{G},\mathbf{G}'} \\ T^*_{\mathbf{G}}\delta_{\mathbf{G},\mathbf{G}'} & -\Delta_{\mathbf{G}-\mathbf{G}'} \end{pmatrix}, \end{aligned} \tag{2.13}$$

where $T_{\mathbf{G}} = \hbar v_F[k_x + G_x - i(k_y + G_y)]$. This is set up as matrices and solved for eigenvalues at each desired k-point. This may be used to produce band structures as well as optical spectra for GALs. One very crucial observation of Eq. 2.13 is that if the lengths are scaled by some factor and all energies are scaled inversely by the same factor, the problem is unchanged. This system is therefore scale invariant.

The band gap may also be estimated analytically by making an approximation to the Dirac model with a spatially varying mass term. The problem is symmetrized by assuming cylindrical symmetry such that both the antidot and unit cell are circular with radii R and R_e, respectively. The wave function inside and outside the antidot may then be expressed using Bessel functions and matched at the interface, see Paper I for more details. The problem is analyzed at the Γ-point where the Bloch phase is zero and the boundary condition

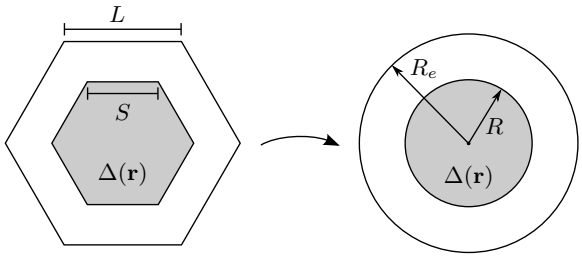

Fig. 2.3: Approximation of the hexagonal unit cell by assuming cylindrical symmetry. The unit cell and antidot side lengths L and S are replaced by the equivalent unit cell radius R_e and antidot radius R.

implies that the derivative of the wave function is zero at $r = R_e$. This leads to the equation

$$J_1(kR_e)[Y_0(kR) + Y_1(kR)] - Y_1(kR_e)[J_0(kR) + J_1(kR)] = 0, \tag{2.14}$$

where J_n and Y_n are the n'th order Bessel functions of the first and second kind, respectively, and $k = E/(\hbar\, v_F)$ includes the energy. This may be solved numerically to obtain half the band gap energy. However, this may also be simplified by Taylor expanding Eq. 2.14 in the low-energy regime (assuming small k), leading to an equation that may be solved analytically, yielding a band gap of

$$E_g = \frac{8\hbar v_F R}{R_e^2 - R^2 + \sqrt{5R^4 - 6R^2R_e^2 + R_e^4 + 8R^2R_e^2\ln(R_e/R)}}. \tag{2.15}$$

Using the substitution $x = R/R_e$, the expression becomes

$$E_g R_e = \frac{8\hbar v_F x}{1 - x^2 + \sqrt{1 + 5x^4 - 6x^2 - 8x^2\ln(x)}}, \tag{2.16}$$

which clearly demonstrates the scale invariance of the model. If all distances are scaled by some factor, the right side is unchanged and the energy must be scaled by the inverse factor. Approximating Eq. 2.15 in the limit of small antidot radius leads to the linear expression of the band gap

$$E_g = 4\hbar\, v_F \frac{R}{R_e^2} = 4\sqrt{\pi}\hbar\, v_F \frac{A_{removed}^{1/2}}{A_{total}}, \tag{2.17}$$

which is useful in the low antidot area fraction regime.

5 Dirac model for transport calculations

The transport properties through graphene nanostructures will also be studied in this thesis. A graphene antidot barrier (GAB) is a one-dimensional periodic antidot structure in an otherwise pristine sheet of graphene. We study such structures using a Green's tensor area integral equation method which is used in a similar fashion to solve scattering problems in optics [134, 135]. The basic geometry is shown in Fig. 2.4 where a spatially varying mass term defines the antidot regions in the same way described in Sec. 4. The theoretical description begins with the DE with a spatially varying mass term

$$\begin{pmatrix} \Delta(\mathbf{r}) - E & v_F(\hat{p}_x - i\hat{p}_y) \\ v_F(\hat{p}_x + i\hat{p}_y) & -\Delta(\mathbf{r}) - E \end{pmatrix} \begin{pmatrix} \Psi_A \\ \Psi_B \end{pmatrix} = 0, \tag{2.18}$$

which may also be written in a compact form as

$$(v_F \boldsymbol{\sigma} \cdot \mathbf{p} + \Delta(\mathbf{r})\sigma_z - \mathbf{I}E)\Psi = 0, \tag{2.19}$$

where $\Psi = \{\Psi_A, \Psi_B\}$ is the wave function spinor, $\boldsymbol{\sigma} = \{\sigma_x, \sigma_y\}$ and σ_z are the Pauli matrices and $\mathbf{p} = \{\hat{p}_x, \hat{p}_y\}$ is the momentum operator. Again, the mass

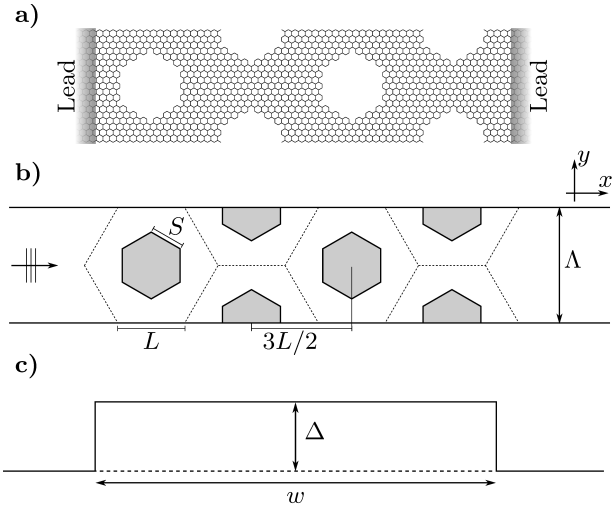

Fig. 2.4: Example of a GAB unit cell with four armchair antidots. a) Atomistic structure for TB. b) Structure for the Dirac model, where the mass term has a constant value of Δ_0 inside the gray (antidot) areas and is vanishing elsewhere. c) Dirac mass barrier with constant mass term Δ in the entire barrier width w.

term has a constant and large value inside the antidots, which prevents electrons from entering them, and is vanishing elsewhere. The incident wave function Ψ_0 must be a solution to the pristine case (no antidots) where $\Delta(\mathbf{r}) = 0$, leading to the DE without a mass term. The incident wave function is described as a plane wave on the form $\Psi_0 = 2^{-1/2}(1, e^{i\varphi})^T e^{i\mathbf{k}\cdot\mathbf{r}}$, where φ is the polar angle of $\mathbf{k}$. Subtracting the DE for the incident wave from Eq. 2.19 leads to

$$(v_F\boldsymbol{\sigma}\cdot\mathbf{p} - \mathbf{I}E)(\Psi - \Psi_0) = -\Delta(\mathbf{r})\sigma_z\Psi. \tag{2.20}$$

For the equation $\mathcal{L}\mathbf{A}(\mathbf{r}) = \mathbf{B}(\mathbf{r})$, where $\mathcal{L}$ is an operator and $\mathbf{A}(\mathbf{r})$ and $\mathbf{B}(\mathbf{r})$ are an unknown and known function, respectively, the solution may be expressed from the Green's function as

$$\mathbf{A}(\mathbf{r}) = -\int \mathbf{G}(\mathbf{r}-\mathbf{r}')\mathbf{B}(\mathbf{r})d^2r'. \tag{2.21}$$

This means that the solution to Eq. 2.20 is

$$\Psi(\mathbf{r}) = \Psi_0(\mathbf{r}) + \int \widetilde{\Delta}(\mathbf{r}')\sigma_z\mathbf{G}(\mathbf{r},\mathbf{r}')\Psi(\mathbf{r}')d^2r', \tag{2.22}$$

where $\widetilde{\Delta}(\mathbf{r}) = \Delta(\mathbf{r})/\hbar v_F$. This is the integral equation that is used to solve for the wave function in the Dirac system. Similarly to the Dirac model of GALs described in the previous section, it can be shown that this equation is unchanged when all lengths are scaled by some factor and energies are scaled by the inverse factor. This means that this problem is also scale invariant.

The Green's tensor $\mathbf{G}$ between an observation point $\mathbf{r}$ and source point $\mathbf{r}'$ is the solution to

$$(v_F\boldsymbol{\sigma}\cdot\mathbf{p} - \mathbf{I}E)\mathbf{G}(\mathbf{r},\mathbf{r}') = -\mathbf{I}\delta(\mathbf{r}-\mathbf{r}'). \tag{2.23}$$

Together with the radiation condition, this uniquely specifies the Green's tensor for this problem as

$$\mathbf{G}(\mathbf{r},\mathbf{r}') = \frac{k}{4i}\begin{pmatrix} H_0^{(1)}(kr) & -ie^{-i\theta}H_1^{(1)}(kr) \\ -ie^{i\theta}H_1^{(1)}(kr) & H_0^{(1)}(kr) \end{pmatrix}, \tag{2.24}$$

where $H_n^{(1)}$ is the n'th order Hankel function of the first kind, $k = E/\hbar v_F$, $r = \|\mathbf{r}-\mathbf{r}'\|$ and θ is the polar angle of $\mathbf{r}-\mathbf{r}'$. The integral equation is solved by discretizing the structure into small area elements δA_i centered at $\mathbf{r}_i$. It is assumed that the wave function is constant within each area element for

sufficiently small elements, and that the Green's tensor between element i and j may be written as

$$\mathbf{G}_{ij} \simeq \begin{cases} (\delta A_j)^{-1} \int_{\delta A_j} \mathbf{G}(\mathbf{r}_i, \mathbf{r}') d^2 r' & \text{if } i = j \\ \mathbf{G}(\mathbf{r}_i, \mathbf{r}_j) & \text{if } i \neq j \end{cases} . \tag{2.25}$$

The self-interaction element $i = j$ is evaluated by approximating the area element as a circle with $\delta A = \pi r_{eq}^2$ and integrate the area element in polar coordinates

$$\mathbf{G}_{ii} \simeq [1/(\pi r_{eq}^2 k) - i H_1^{(1)}(k r_{eq})/(2 r_{eq})]\mathbf{I}. \tag{2.26}$$

The method as formulated above is designed for solving scattering of Dirac electrons in finite nanostructures. The theory may be expanded to the periodic case where the scattered part of the wave function becomes a sum of the contributions from all unit cells. The wave function satisfies the Bloch condition $\Psi(\mathbf{r} + m\Lambda\hat{y}) = \Psi(\mathbf{r}) e^{imk_y\Lambda}$, where m is an integer and $\Lambda = \sqrt{3}L$ is the period. This means that the integral may be limited to the zeroth unit cell

$$\Psi(\mathbf{r}) = \Psi_0(\mathbf{r}) + \int_{A_0} \widetilde{\Delta}(\mathbf{r}') \sigma_z \widetilde{\mathbf{G}}(\mathbf{r}, \mathbf{r}') \Psi(\mathbf{r}') d^2 r', \tag{2.27}$$

where $\widetilde{\mathbf{G}}(\mathbf{r}, \mathbf{r}')$ is the modified Green's tensor. This may be evaluated using Graf's theorem [136] such that

$$\begin{aligned} \widetilde{\mathbf{G}}(\mathbf{r}, \mathbf{r}') &= \sum_{m=-\infty}^{\infty} \mathbf{G}(\mathbf{r}, \mathbf{r}' - m\Lambda\hat{y}) e^{ik_y m\Lambda} \\ &= \sum_{m=-M}^{M} \mathbf{G}(\mathbf{r}, \mathbf{r}' - m\Lambda\hat{y}) + \frac{k}{4i} \sum_{n=-\infty}^{\infty} i^n J_n(kr) e^{-in\theta} \begin{pmatrix} S_n & -S_{n-1} \\ -S_{n+1} & S_n \end{pmatrix}, \end{aligned} \tag{2.28}$$

where S_n is the so-called lattice sum

$$S_n = \sum_{m=M+1}^{\infty} H_n^{(1)}(km\Lambda) \left(e^{ik_y m\Lambda} + (-1)^n e^{-ik_y m\Lambda} \right). \tag{2.29}$$

The contribution from M unit cells on either side of the zeroth cell are excluded from the lattice sum. This is because they may not fulfill Graf's theorem depending on the length of the unit cell. Writing the latte sum on this form is advantageous as it does not depend on the distance between area elements.

The transmittance is given by the fraction of transmitted current I and incident current I_0. The transmitted current is calculated by integrating the current density j_x, given by $j_x = \Psi^\dagger \hat{j}_x \Psi$ where $\hat{j}_x = -ev_F\sigma_x$, over one unit cell

at the other side of the barrier $I = \int_{uc} j_x dy$. The transmittance curve $T(E)$ may then be calculated by sweeping the energy of the incident wave.

The equations from the discretized structure may be set up as a matrix problem and solved by matrix inversion. However, this scales badly with the number of elements N in the structure, where the memory requirement with complexity $O(N^2)$ becomes problematic. The problem may also be solved self-consistently by exploiting iterative algorithms for solving matrix equations. Specifically, the algorithm by Draine [137] has been used for the results presented here. In this algorithm, some parameters are initialized and then used in the algorithm to iteratively improve the solution. This is continued until some chosen error parameter is sufficiently small. It is furthermore convenient to use fast Fourier transform for evaluating the discrete convolutions in the algorithm, which further improves the performance. The memory requirement may then be reduced to $O(N)$, meaning that structures with much more elements may be evaluated.

6 Second-harmonic optical response in bilayer graphene

The last section of the results chapter concerns the second-harmonic (SH) optical properties of biased bilayer graphene (BLG). Here, the model and theory for studying this system is presented. Furthermore, the reason why Wu *et al.* [121] see a vanishing response in their calculations is elaborated, and an estimate of the emergence of a double-resonance is derived. This system is modeled using TB and including the electric field as an on-site shift of the top and bottom layers of $\pm\Delta$. The Hamiltonian is then given by

$$\mathbf{H} = \begin{pmatrix} -\Delta - \frac{\Delta'}{2} & -\gamma_0 f(\mathbf{k}) & \gamma_4 f(\mathbf{k}) & -\gamma_3 f^*(\mathbf{k}) \\ -\gamma_0 f^*(\mathbf{k}) & -\Delta + \frac{\Delta'}{2} & \gamma_1 & \gamma_4 f(\mathbf{k}) \\ \gamma_4 f^*(\mathbf{k}) & \gamma_1 & \Delta + \frac{\Delta'}{2} & -\gamma_0 f(\mathbf{k}) \\ -\gamma_3 f(\mathbf{k}) & \gamma_4 f^*(\mathbf{k}) & -\gamma_0 f^*(\mathbf{k}) & \Delta - \frac{\Delta'}{2} \end{pmatrix}, \tag{2.30}$$

where the TB parameters are from Ref. 138. The model includes both the in-plane nearest neighbor hopping parameter γ_0, the direct coupling γ_1 between atoms stacked on top of each other and skew coupling γ_3 and γ_4. Interestingly, the bias leads to the opening of a tunable band gap which has been studied both theoretically [27–29] and experimentally [28–32]. The band structure around the K-point for $\Delta = 0.4$ eV is shown in Fig. 2.5, where the band gap and saddle point transition energy is illustrated.

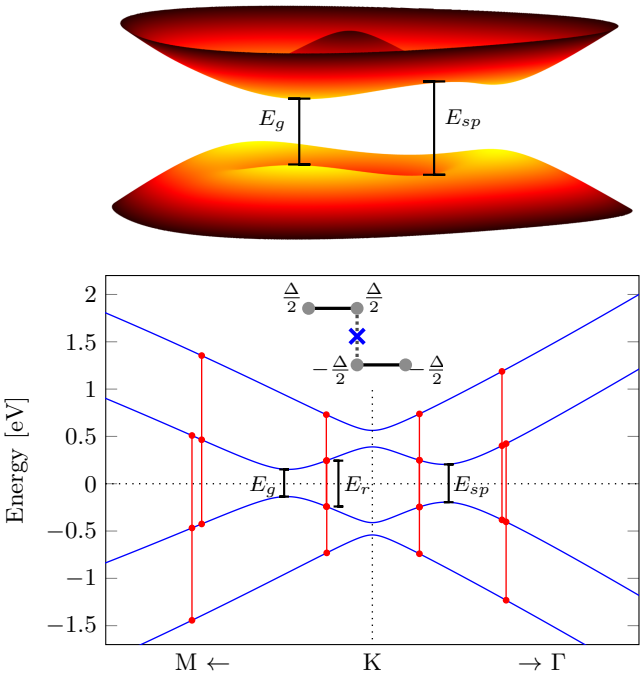

Fig. 2.5: Band structure of biased BLG around the K-point for $\Delta = 0.4$ eV. The top part shows energy surfaces of the top valence and bottom conduction bands. The band structure with the band gap and saddle point transition energy are shown, and double-resonance transitions are highlighted by red lines. The inset illustrates BLG with the on-site shifts on the four atoms, and the inversion point for vanishing bias is shown by the blue cross.

Second-harmonic generation (SHG) is studied by calculating the susceptibility using the independent-particle approximation in the low-temperature limit. For simplicity, only interband contributions are included, although intraband transitions may also contribute to the SH response. The imaginary part of the SH susceptibility is then [116, 117]

$$\chi^{(2)\,\prime\prime}_{abc}(\omega) = \frac{e^3}{2\pi m_e^3 \hbar^2 \varepsilon_0 \omega^3} \sum_{c,v,l} \int \left[\frac{P_{vcl}}{\omega - \omega_{lv}} \delta(2\omega - \omega_{cv}) + \left(\frac{P_{vlc}}{\omega + \omega_{cl}} + \frac{P_{clv}}{\omega + \omega_{lv}} \right) \delta(\omega - \omega_{cv}) \right] d^2k, \tag{2.31}$$

where $P_{ijl} = \mathrm{Im}\{p^a_{ij}(p^b_{jl}p^c_{li} + p^c_{jl}p^b_{li})\}/2$, p^a_{ij} is the a component of the momentum matrix element between states i and j and $\omega_{ij} = \omega_i - \omega_j$. Momentum matrix elements are calculated as $p^a_{ij} = \mathbf{v_i}^\dagger \mathbf{P_a} \mathbf{v_j}$, where $\mathbf{P_a} = \frac{m}{\hbar} \frac{\partial \mathbf{H}}{\partial k_a}$ is the momentum matrix in the a-direction and $\mathbf{v_i}$ is the ith eigenvector. Indices c and v refer

to conduction and valence bands, respectively, while $l \neq (c, v)$ runs over all bands. The only non-vanishing elements of the SH tensor are $\chi^{(2)}_{xxx} = -\chi^{(2)}_{xyy} = -\chi^{(2)}_{yyx} = -\chi^{(2)}_{yxy} \equiv \chi^{(2)}$. This expression leads to so-called double-resonances, which occur at fundamental photon energies E_r where $\omega = \omega_{lv}$ and $2\omega = \omega_{cv}$ are fulfilled at the same time. This case is shown by the red lines in Fig. 2.5.

As mentioned in Chap. 1, SHG in BLG has been studied by Wu *et al.* [121] who found no response, even with a perpendicular electric field, and instead included an in-plane current to break the symmetry. Their approach is based on the Dirac model with only the direct interlayer coupling for which the Hamiltonian becomes

$$\mathbf{H} = \begin{pmatrix} -\Delta & q_- & 0 & 0 \\ q_+ & -\Delta & \gamma_1 & 0 \\ 0 & \gamma_1 & \Delta & q_- \\ 0 & 0 & q_+ & \Delta \end{pmatrix}, \tag{2.32}$$

where $q_\pm = \hbar v_F(q_x \pm \xi i q_y)$ and $q_{x/y} = k_{x/y} - K_{x/y}$. This general expression describes both the K ($\xi = +1$) and K' ($\xi = -1$) valleys. When changing from K to K', the Hamiltonian becomes complex conjugated. By considering the complex conjugate of the Schrödinger equation $(\mathbf{Hc})^* = (E\mathbf{c})^*$ it is seen that a conjugated Hamiltonian leads to conjugated eigenvectors

$$\mathbf{H} \to \mathbf{H}^* \quad \Rightarrow \quad \mathbf{c} \to \mathbf{c}^*. \tag{2.33}$$

For the Dirac model, the momentum matrices also become conjugated, which entails a conjugation of the momentum matrix elements. The SH tensor element $\chi^{(2)}_{xxx}$ is considered for which P_{ijl} is used. Changing from K to K' then leads to a change of sign

$$P_{ijl}(K') = \mathrm{Im}\{(p^x_{ij})^*(p^x_{jl})^*(p^x_{li})^*\} = -P_{ijl}(K). \tag{2.34}$$

This means that all contributions from the K valley are canceled by the K' valley and no response is seen.

In the TB Hamiltonian, the only complex entity is $f(\mathbf{k})$. Changing from K to K', corresponding to $\mathbf{k} \to -\mathbf{k}$, does in fact lead to a complex conjugation of the Hamiltonian. The derivative of f with respect to k_x is used for the momentum matrix in the x-direction

$$g(\mathbf{k}) = \frac{\partial f(\mathbf{k})}{\partial k_x} = \frac{a}{\sqrt{3}}\left[e^{i\left(k_x\frac{a}{\sqrt{3}}+\frac{\pi}{2}\right)} - e^{-i\left(k_x\frac{a}{2\sqrt{3}}-\frac{\pi}{2}\right)}\cos\left(k_y\tfrac{a}{2}\right)\right]. \tag{2.35}$$

From the expression above, it is clear that $g(-\mathbf{k}) \neq g^*(\mathbf{k})$, meaning that the contributions from the two valleys do not cancel in the TB model.

The Dirac model of biased BLG may also be used to derive an analytic expression for the value of Δ at which the double-resonance appears. The Hamiltonian in Eq. 2.32 leads to the eigenvalues

$$E = \pm\frac{1}{\sqrt{2}}\sqrt{2\Delta^2+\gamma_1^2+2q^2\pm\sqrt{16\Delta^2q^2+\gamma_1^4+4\gamma_1^2q^2}}, \tag{2.36}$$

where $q^2 = \hbar^2 v_F^2(q_x^2+q_y^2)$. For energies sorted according to $E_1 < E_2 < E_3 < E_4$, the resonance condition becomes $E_3 - E_2 = E_2 - E_1$. This is solved for the q closest to the K point, giving the expression

$$q = \frac{1}{4\sqrt{2}}\sqrt{68\Delta^2+9\gamma_1^2-5\sqrt{144\Delta^4+8\Delta^2\gamma_1^2+9\gamma_1^4}}. \tag{2.37}$$

Requiring real values of q leads to the condition $\Delta \geq \gamma_1/\sqrt{8}$ with the corresponding minimum double-resonance energy $E_{r,min} = \gamma_1/\sqrt{2}$. This means that the double-resonance only appears when Δ is above this threshold value.

The expression for the photon energy at which the double-resonance appears for a given value of Δ may be obtained by using Eq. 2.37 in the resonance condition. This leads to the resonance photon energy

$$E_r = \frac{100\Delta^2+25\gamma_1^2-S-4\sqrt{544\Delta^4+34\gamma_1^4+208\Delta^2\gamma_1^2-2(4\Delta^2+\gamma_1^2)S}}{2\sqrt{2}}, \tag{2.38}$$

where $S = 5\sqrt{144\Delta^4+8\Delta^2\gamma_1^2+9\gamma_1^4}$. This expression is useful for a quick estimate of the photon energy of the double-resonance.

Chapter 3

Summary of results

In this chapter, the main results from the papers found at the end of this thesis are presented. The aim of this chapter is to provide the reader with a thorough overview of the results, yet in a fairly straightforward manner. Therefore, the reader is referred to the papers at the end of the thesis for more details on the topics discussed here.

1 Dirac model of graphene antidot lattices

The first topic of the results section is the important and widely studied field of graphene antidot lattices (GALs). As mentioned in Chap. 1, these systems are made by creating a two-dimensional (2D) periodic pattern of perforations in a pristine sheet of graphene. Using tight-binding (TB) it has been shown that such systems introduce a band gap that may be tuned by changing the geometrical parameters of the lattice [43, 48, 49]. This shows a promising way of turning the otherwise semimetallic graphene into a semiconductor. The TB model is extremely useful for studying such lattices, as it can handle fairly large systems without excessive computation times and has good precision when compared with more accurate methods, i.e., density functional theory (DFT). However, TB becomes problematic for systems with sizes on the experimental scale, as this simply involves too many atoms. For example, structures produced using e-beam lithography have (at the time the results were produced) been made with a period of 36.4 nm and holes with a diameter of 18.7 nm [58]. The unit cell of such a lattice contains in excess of 30,000 atoms, which is problematic for many TB studies.

The aim of the study in Paper I is to produce a theory that can handle nanostructured graphene systems in a continuum approximation. This means that all atomistic features are missing from the theory, which in turn means that the computational difficulty of the problem does no longer depend on the size of the system. The theory described in Sec. 4 of Chap. 2 is used to model the antidot lattices using the Dirac equation (DE). The scalability of the model follows from Eqs. 2.12 and 2.13, and is observed directly in Eq. 2.16. The model introduces a large mass term in the antidot regions, which excludes electrons from the antidots more and more as the mass term increases. The theory is based on describing the mass term and the periodic part of the wave function as Fourier series and setting up an eigenvalue problem which is solved through numerical diagonalization. Obviously, the real system is described by expanding using an infinite basis, which is of course not possible for the calculations. In stead, the calculation should be converged in both the size of the mass term Δ_0 and the size of the basis, which is determined by $\mathbf{G} = p\mathbf{g}_1 + q\mathbf{g}_2$ where $p, q \in [-N, N]$. It was found that using $\Delta_0 = 170$ eVL^{-1} for all calculations and $N = 20$ and $N = 16$ for hexagonal and circular antidots, respectively, provides sufficient convergence. The notations A$\{L, S\}$GAL, Z$\{L, S\}$GAL and C$\{L, R\}$GAL are used to describe GALs with unit cell side length L containing armchair, zigzag and circular antidots, respectively, with antidot side length S or antidot radius R. Examples of such structures are illustrated in Fig. 2.2. Figure 3.1 shows a comparison between band structures calculated using TB and the DE for selected zigzag and armchair antidots of similar sizes. For our study, we are interested in the band gap of the GAL, i.e., the electronic properties at low energies. Therefore, it is sufficient to compare with a nearest neighbor orthogonal TB model. Furthermore, only positive energies are shown because of electron-hole symmetry. It is observed that the Dirac model is generally in good agreement with TB and is able to reproduce most features in the band structures. It is clear that the comparison for armchair antidots is better than zigzag antidots, especially for the larger holes. A nearly dispersionless band is observed in the TB result near 0.09 eV for the Z$\{20, 6\}$GAL which is absent in the DE result. The reason for the better description of armchair antidots is that zigzag edges give rise to localized states, which has been shown theoretically [47, 52, 53] and even observed experimentally in GNRs [54]. Figure 3.1 also shows the probability density for the third conduction band for both the zigzag and armchair versions, and we observe that this state is strongly localized on the zigzag edge, while it is distributed over the entire unit cell with

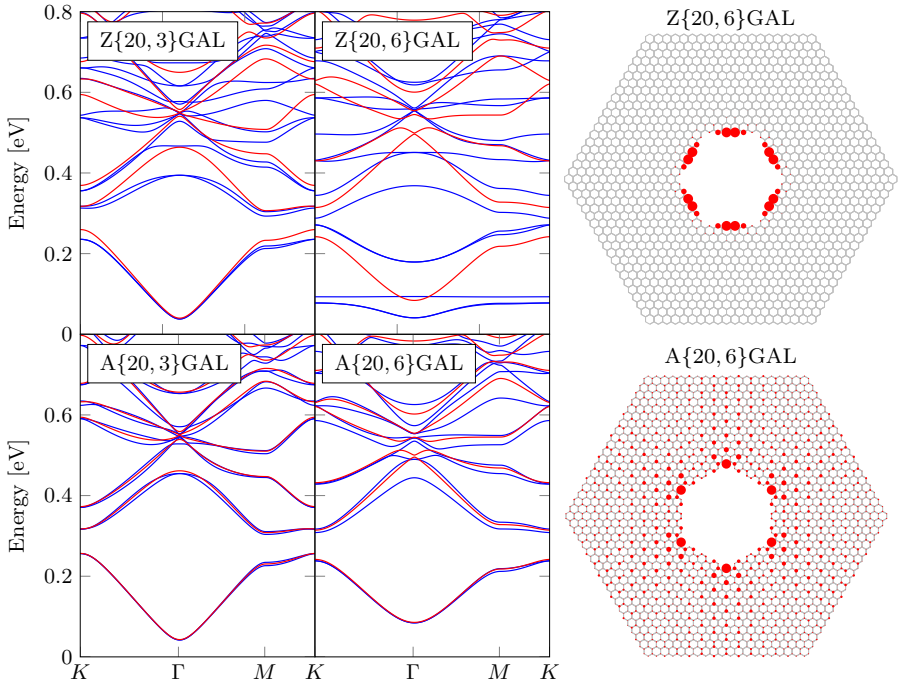

Fig. 3.1: Comparison of band structures calculated using the DE (red) and TB (blue) for GALs with zigzag and armchair antidots. The electron probability density for the third conduction band within the unit cell is shown to the right for two GALs. The radii of the circles are proportional to the absolute square of the corresponding eigenvector element and chosen such that the largest circles have the same radius in both plots.

only a slight localization at the antidot corners for the armchair version. As the Dirac model is a continuum model, it lacks all atomistic features and is therefore unable to describe the edge state at the zigzag edges, which is why the models deviate more for this kind of GAL.

The DE has previously been used by Fürst *et al.* [45] to study GALs by including a spatially varying mass term. Their approach is different from the one presented here in two ways. One, they use an infinite mass term inside the antidot region and, two, they solve the system using the commercial software tool COMSOL Multiphysics. They observed deviations in the band structures when comparing with TB, as their bands were shifted in energy away from the Fermi level. The requirement for an infinite mass term is that the current perpendicular to the antidot edge at the edge is zero. This leads to the boundary condition $\Psi_1(\mathbf{r}) = e^{-i\phi}\Psi_2(\mathbf{r})$, where ϕ is the polar angle of the normal vector at

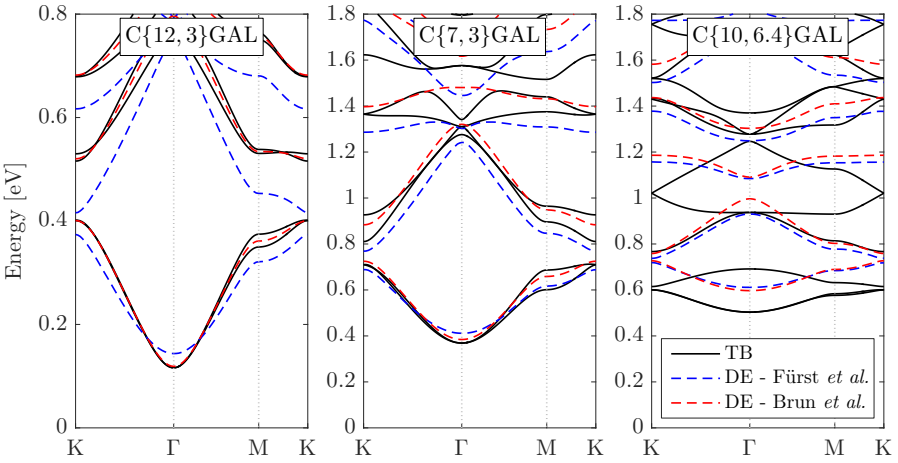

Fig. 3.2: Comparison of band structures of selected GALs calculated using TB, a DE method using COMSOL by Fürst *et al.* [45] and the Dirac model presented here. The band structures by Fürst *et al.* are shifted in energy according to the description in their paper.

the edge. This angle becomes completely undetermined in the limit of vanishing antidot radius. The shift of the bands is likely caused by this problem, and they found that the energies should be corrected by $1.02\gamma/L$. In Fig. 3.2 the band structures of selected GALs are compared for both TB, the Dirac model by Fürst *et al.* with energy correction and the Dirac model presented here. The band structures from the two Dirac models are generally very similar, however, the model presented here still yields better results than the previous attempt to make a continuum model description of GALs. Furthermore, the energy shift is not observed for the new calculations.

In addition to the band structures, the optical conductivity may also be calculated using the two models. This comparison is shown in Fig. 3.3 for the same structures compared in Fig. 3.1. Again, it is seen that the models agree well for armchair structures and worse for zigzag antidots. For the GAL with the small zigzag antidot, the agreement is quite good, especially at energies < 0.5 eV, which is due to the weak localization on the short zigzag edge. The spectra for the larger zigzag antidot are completely different and no discernible resemblance is observed. In contrast, the spectra for the armchair antidots are in very good agreement in the entire energy range up to 1 eV.

In order to compare the models for more antidot lattices, we chose to compare the band gap of numerous GALs by varying both L and S/R. Figure 3.4 shows these band gaps for the different types of GALs. Furthermore, a band

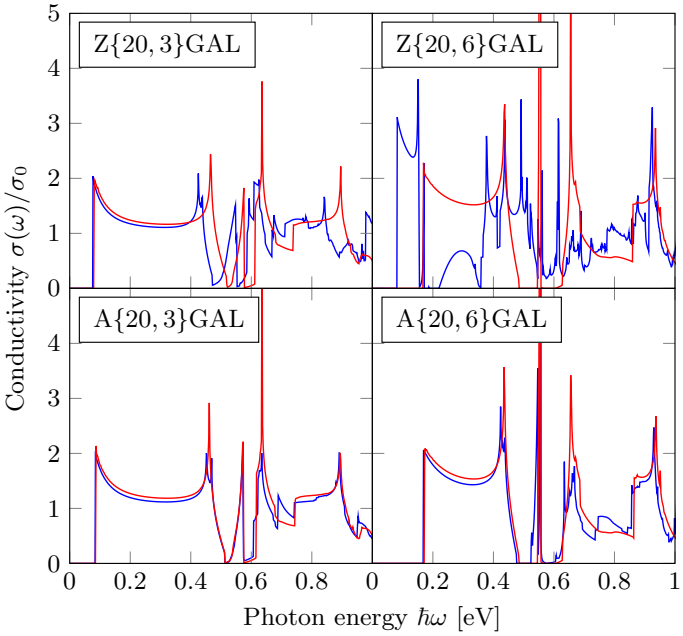

Fig. 3.3: Optical spectra of GALs with zigzag and armchair edges calculated using TB (blue) and our Dirac model (red). The spectra are in units of the low-energy pristine graphene conductivity $\sigma_0 = e^2/4\hbar$.

gap curve may be obtained from the Dirac model by solving the eigenvalue problem described earlier for different sizes of the antidot, which is also shown in the figure. As expected from observing the band structures, armchair GALs are described much better by the Dirac model than zigzag GALs because they have no edge states causing localization. The red dots show structures with small holes which are observed to agree better than larger holes, as the localization is weaker. The same is observed for GALs with circular antidots, where large holes have longer zigzag segments and only the smaller holes agree well with the Dirac model. The band gap may also be estimated using the Dirac model, which leads to Eq. 2.14 that must be solved numerically for obtaining half the band gap. This curve is shown in all panels of Fig. 3.4 and the agreement with the curve from solving the eigenvalue problem is very good. The band gap may also be expressed analytically by Taylor expanding the equation assuming low energies, leading to Eq. 2.15. This band gap curve is very close to the other curves, and Eq. 2.15 may therefore be used for a quick estimate of the band gap for structures with no edge states. In the case of the so-called ro-

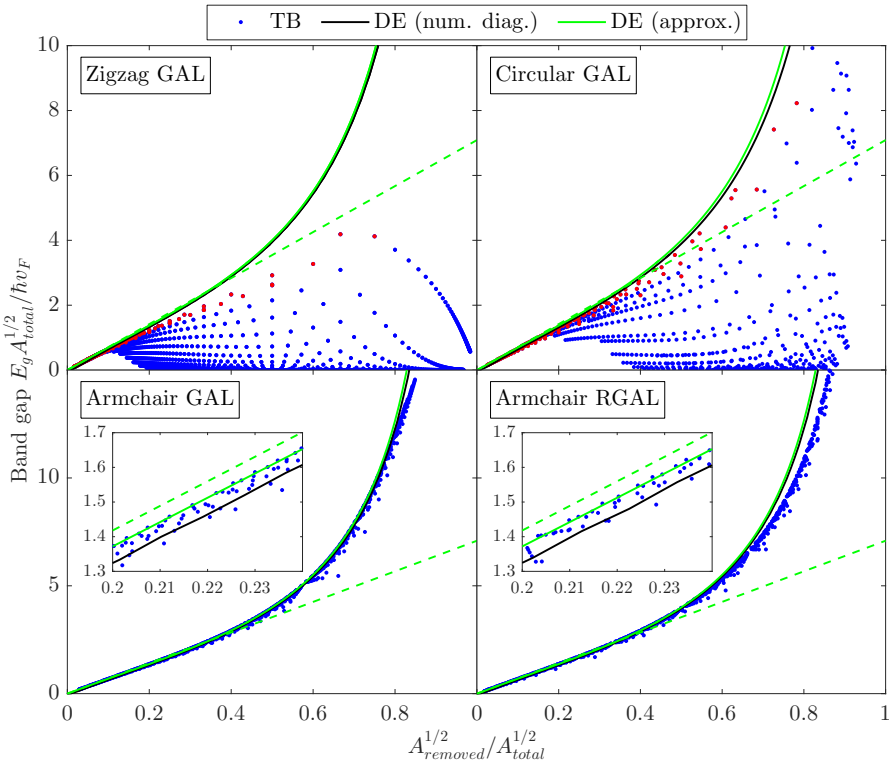

Fig. 3.4: Band gap calculations for numerous GAL structures. The dots show the TB band gap calculations from varying both L and S/R, where the red dots are for $S \leq 3$ and $R \leq 5$ for zigzag and circular antidots, respectively. The dashed green line is the linear Dirac description of the band gap.

tated GAL (RGAL) structures with armchair antidots, the deviation between TB and the Dirac model is seen to be larger than for GALs with armchair antidots. RGAL structures with large hole area fractions are basically connected armchair nanoribbons, while GALs form graphene triangles connected at the corners. Brey and Fertig [139] studied graphene nanoribbons (GNRs) with the DE and found that the energies of especially armchair nanoribbons are larger than the TB values, which agrees with the observation here. The results summed up in Fig. 3.4 are strong evidence that this Dirac model is very useful for estimating the band gap of GAL structures on any scale when no edge states are present.

2 Transport through graphene antidot barriers

The potential for applying graphene nanostructures within electronics and optoelectronics demands a thorough understanding of the transport properties of such systems. This section is based on Paper II and presents the results obtained for transport through graphene antidot barriers (GABs) studied with the DE. The theoretical description for these results is presented in Sec. 5 of Chap. 2. An area integral equation is set up using a Green's tensor and solved by discretizing the structure in small area elements. The method is further improved by an iterative algorithm, where discrete convolutions are performed using fast Fourier transform. The transport is also calculated for the atomistic structures with the Landauer approach using an orthogonal nearest neighbor TB Hamiltonian as described in Ref. 69 and compared with the Dirac model.

Transport of Dirac electrons through GABs, which are illustrated in Fig. 2.4, is studied for both atomistic and Dirac models. The theory is applied to the

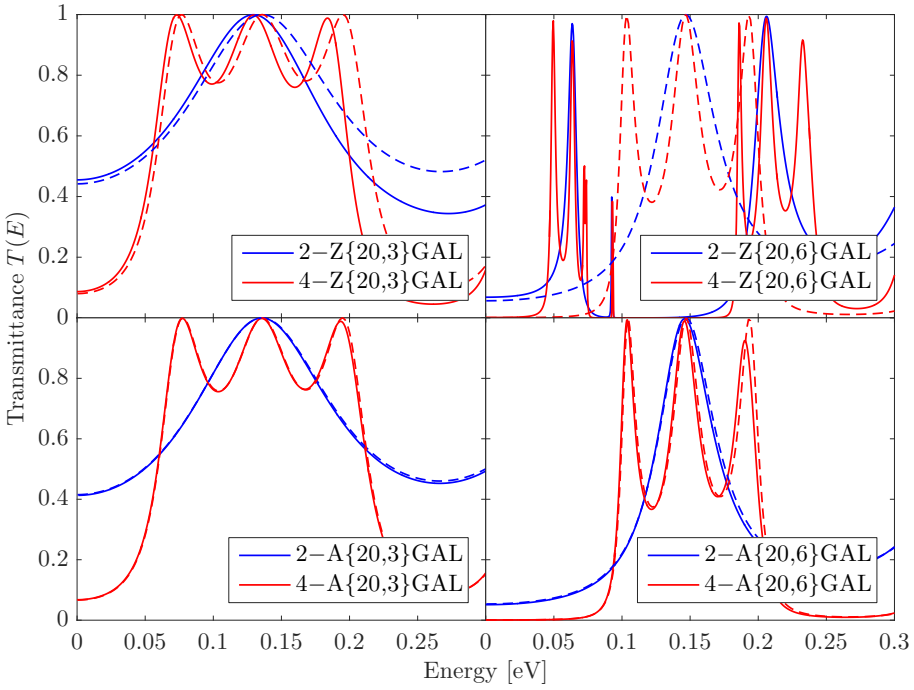

Fig. 3.5: Comparison of the transmittance through different GABs calculated using TB (solid lines) and our Dirac model (dashed lines). Top and bottom panels show structures with zigzag and armchair antidots, respectively.

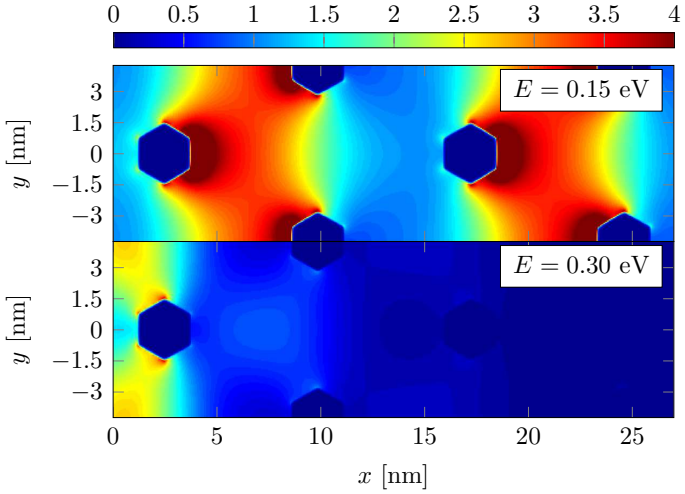

Fig. 3.6: Electron probability density within one unit cell for the A{20, 6}GAL barrier with 4 antidots at two energies calculated using the Dirac model.

same type of antidot lattices as focused on for the fully periodic case in Sec. 1. The top panels of Fig. 3.5 show the transmittance through barriers with zigzag antidots of two sizes calculated using the two models. Only positive energies are shown because of electron-hole symmetry. The transmittance is described quite well by the Dirac model for the smaller antidot, but large deviations are seen for the larger antidot. In the case of armchair antidots, shown in the bottom panels of the figure, the agreement between the models is excellent and the Dirac model describes the transport very well for all energies shown. It is also observed that adding more antidots to the barrier lowers the transmittance at low energies, i.e. within the band gap, and adds more subpeaks to the transmittance peak. The actual band gap of the A{20, 6}GAL structure from TB is 169 meV and the figure shows that the onset of the transmittance occurs as a sharper transition closer to half this value as the number of antidots increases. This follows from the argument that an infinitely long barrier will completely suppress the transport in the band gap region. The observations from Fig. 3.5 are in complete agreement with the results from Sec. 1, where edge states cause discrepancies between the models for zigzag but not armchair antidots.

To better understand the transport through the GABs, the probability density is calculated in the Dirac model. Figure 3.6 shows the probability density for the A{20, 6}GAL barrier with 4 antidots at two energies. First of all, it

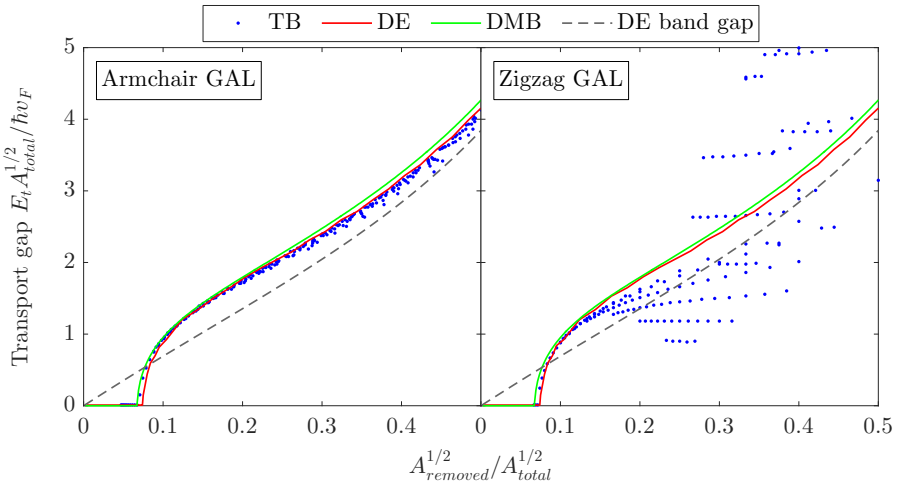

Fig. 3.7: Transport gap of A$\{L, S\}$GAL barriers (left panel) and Z$\{L, S\}$GAL barriers (right panel) with 4 antidots in the unit cell. The transport gap is calculated using TB, the Dirac model presented here and the DMB model. The analytic band gap from the previous section is also shown.

is noted that the probability density inside the antidots is very low due to the large mass term. For the lower energy, the probability density inside the barrier is quite high which is because this energy is within one of the bands of the fully periodic structure as seen in Fig. 3.1. The transmittance in this case is $T = 0.91$. For the larger energy there are no states available in the barrier and consequently the probability density is much lower, resulting in the transmittance $T = 0.02$. This shows that GABs only allow electrons to pass through at energies where states are available in the fully periodic structure.

For a more broad overview of the validity of the model, the transport gap has been calculated for many barriers with 4 antidots in the unit cell using TB and compared with the Dirac model in Fig. 3.7. Here, the transport gap is defined as the lowest energy at which the transmittance is above 1/2. The study is carried out for barriers with just four antidots per unit cell to see how much such short barriers suppress the transport in the band gap. The figure shows that a transport gap opens up for structures where $A_{removed}^{1/2}/A_{total}^{1/2} > 0.07$. The gaps are zero below this value, as the antidots are so small that the transmittance is larger than 1/2 even at vanishing energy. The rapid increase of the transport gap is caused by the horizontal slope of the transmittance curve at vanishing energy. As the size of the antidot is increased, the transmittance becomes lower and the transport gap increases rapidly when the transmittance drops

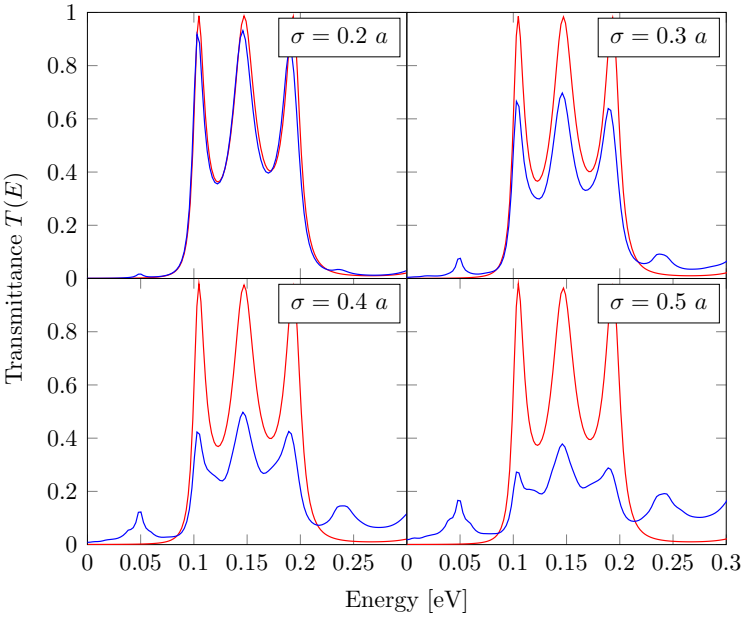

Fig. 3.8: Comparison of transmittance spectra for disordered A{20, 6}GAL barriers with 4 antidots calculated using TB (blue) and the Dirac model (red).

below 1/2. Again, armchair antidots are seen to be in good agreement with the Dirac model while for zigzag antidots this is only the case for small antidots. For zigzag antidots with $A^{1/2}_{removed}/A^{1/2}_{total} > 0.15$, large deviations are observed between the models and the transport gap in TB is often larger than predicted by the Dirac model. This is contrary to the band gap in Sec. 1 which is always lower for TB than the Dirac model. As mentioned earlier, edge states are localized to the edges of the antidots and may therefore not support transport of electrons through the barrier, which explains why the transport gap is higher in some cases. The band gap calculated using Eq. 2.15 is also shown, and the transport gap is seen to be significantly larger than the band gap. This is because the barriers contain only 4 antidots in the unit cell, whereas the transport gap will move closer to the band gap as the antidot barriers become longer. The figure also shows calculations of the transport gap using the Dirac mass barrier (DMB) model illustrated in Fig. 2.4. Here, the mass term is constant inside the barrier and set at a value of half the band gap of the corresponding GAL, which may be obtained easily from Eq. 2.14. The transport gap may then be calculated using the theory described in Ref. 69. This model

is quite simple, yet yields a transport gap very close to the full Dirac model and is thus useful for quick estimates of the transport gap.

Experimental devices are always subjected to some degree of disorder from the fabrication process. Usually, top-down methods are used, where inaccuracies lead to e.g. disorder at the edges of the antidots. The effect of randomly displacing the antidots in the barrier is studied, where the displacement is according to a normal distribution with a standard deviation σ such that the mean displacement is $\sigma\sqrt{2/\pi}$. Figure 3.8 shows the transmittance for the A$\{20, 6\}$GAL barrier with 4 antidots, which is calculated by averaging several random configurations. The emerging peaks in the TB spectra at $E = 0.05$ eV and $E = 0.24$ eV for large disorder are not observed in the Dirac model. However, the models still agree well at lower degrees of disorder.

3 Doping in graphene antidot lattices

The previous sections have stressed the importance of knowing the band gap and transport properties of nanostructured graphene. Another important topic within graphene research is doping, which is often a necessity for device applications. As mentioned in Chap. 1, doping has been studied widely in graphene and GNRs both theoretically and experimentally [80–82, 86, 88–98]. Doping in GALs has also been studied, where scanning Raman spectroscopy has in-

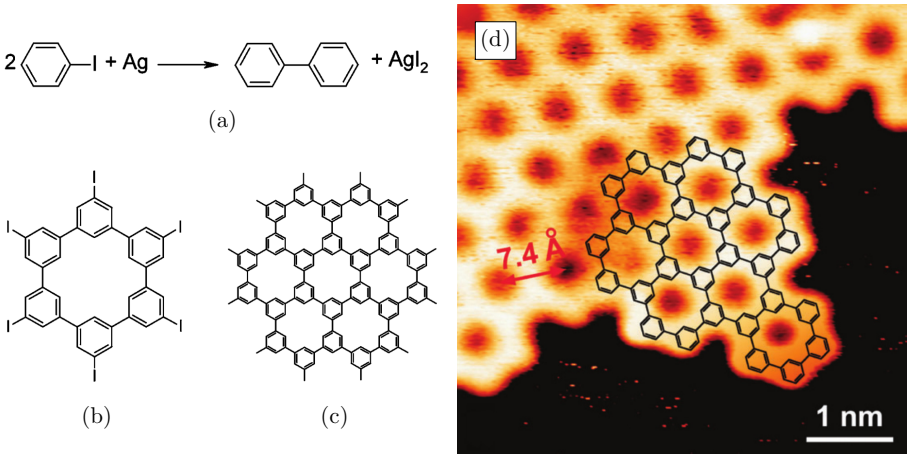

Fig. 3.9: (a) Silver-promoted aryl-aryl reaction. (b) Structure of the CHP molecule. (c) Part of the finished GAL. (d) AFM image of the synthesized GAL with the structure overlaid on part of the image. The figure is from Ref. 85 by Bieri *et al.*

dicated p-type doping after fabrication from electron-beam lithography and it was suggested that the doping stems from the patterning process [140]. GALs fabricated from top-down methods, such as electron-beam lithography, suffer from the disorder that inevitably occur during fabrication. Theoretical studies have shown that disorder can have drastic effects on the electronic and transport properties of GALs [77, 78]. One promising strategy for overcoming these problems is to use bottom-up methods for fabricating graphene nanostructures.

This section is based on the results published in Paper V. Focus is put on a specific type of GAL, which was fabricated and characterized by Bieri *et al.* [85]. The process uses the precursor hexaiodo-substituted macrocycle cyclohexa-m-phenylene (CHP), which assembles into a GAL with sub-nanometer periodicity. This is shown in Fig. 3.9 together with an AFM image of the produced structure. This GAL is the starting point for this study, and it is assume that doped versions of the precursor may be used to fabricate GALs with doping at edge sites. To the best of our knowledge, there has been no previous research on the doping properties of GALs, and we thus present the first step in the direction of understanding such systems.

The pristine and doped versions of the GAL for this study are shown in Fig. 3.10. Doping is included by substituting one edge atom in each cell (corresponding to a molecule) with either boron or nitrogen. The dopant may be terminated by either zero, one or two hydrogen atoms. Both the pristine and fully ordered doped systems are studied using DFT in the software ABINIT. Full structural relaxation is performed on all systems before band structures are calculated. Larger systems have also been studied, such as diluted and disordered doping, for which DFT is too computationally demanding. Therefore, TB parameterizations are used in such cases. The Hamiltonian of the pristine system is given by

$$\mathbf{H_0} = \sum_i \varepsilon_p |i\rangle\langle i| + \sum_{i,j} t_{ij} |i\rangle\langle j|, \tag{3.1}$$

where ε_p is the carbon on-site energy and t_{ij} is the hopping integral between atoms i and j. In Fig. 3.11, the band structure of the pristine GAL from the DFT calculation is shown together with the TB parameterization. It turned out that it was necessary to include up to third nearest neighbor interactions in a non-orthogonal model to get a good fit to the DFT band structure. This structure is actually an RGAL, which are only semiconducting for every third size of the unit cell. This one is a semiconductor, as predicted by the rule in Ref. 50, and shows a quite large band gap of 2.30 eV in agreement with previous calculations [141, 142].

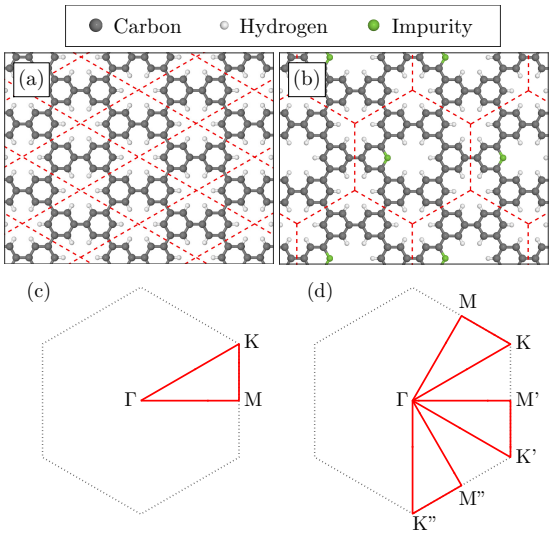

Fig. 3.10: Structure of the pristine (a) and doped (b) GAL of this study, where dashed red lines indicate unit cells. Corresponding Brillouin zone and band structure routes for the pristine (c) and doped (d) systems.

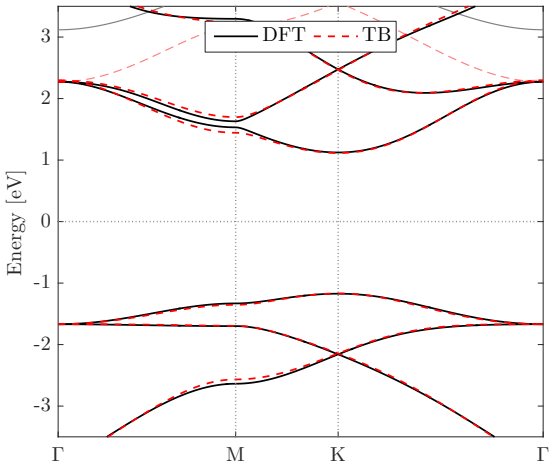

ε_p	t_1	t_2	t_3	s_1	s_2	s_3
-2.18	-2.58	-1.11	-0.29	0.36	0.08	0.07

Fig. 3.11: Band structure of the pristine GAL calculated using DFT together with the third nearest neighbor non-orthogonal TB parameterization. The TB parameters are listed in the table, where the on-site energy and hopping integrals are in units of eV.

DFT band structure calculations of boron and nitrogen doped GALs are shown in Fig. 3.12 for varying degrees of hydrogenation at the impurity. As expected, boron doping introduces a p-type doping level near the top valence band. This acceptor level shifts upwards in energy towards the conduction bands when the number of hydrogen atoms at the impurity increases. Similarly, nitrogen introduces an n-type doping level near the conduction bands that moves towards the valence bands when hydrogenated more. Additionally, it is noticed that the rest of the band structure only changes marginally.

In order to study diluted doping and disorder, a TB parametrization is performed for all the doped structures. The impurity is modeled simply by shifting the on-site potential of the impurity by Δ, making this the only fitting parameter for the perturbed systems. The Hamiltonian is then modified by $\mathbf{H_1} = \Delta|l\rangle\langle l|$, where the impurity is at the l'th site. Others have included

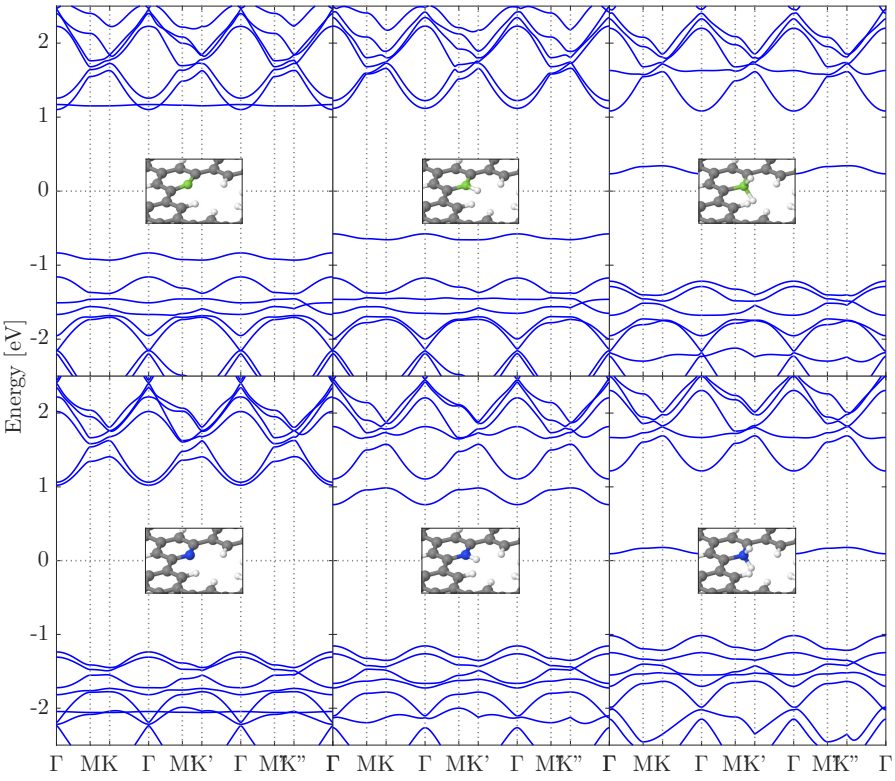

Fig. 3.12: DFT band structures of GALs doped with one boron (top panels) or nitrogen (bottom panels) atom in each molecule, where the dopant is terminated by (from left to right) zero, one and two hydrogen atoms.

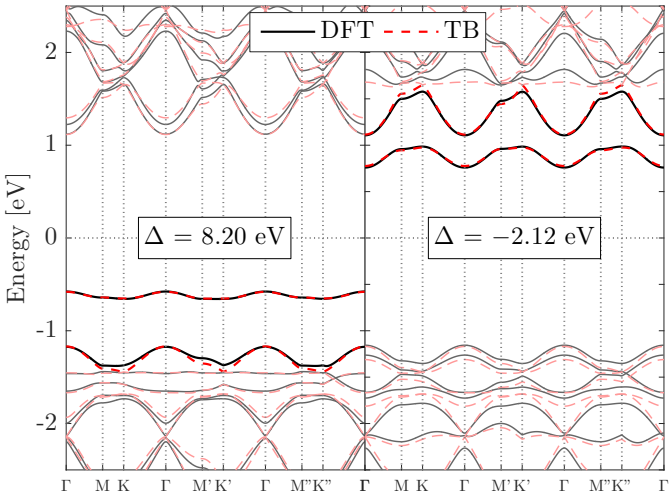

Fig. 3.13: DFT band structures and TB parameterizations of boron (left) and nitrogen (right) doped GALs terminated by one hydrogen atom at the impurity. Full colors/lines show the bands used for the parameterizations.

changes in the hopping integral between the impurity and its neighbors [82, 92], however, this was found to only change the fit marginally. Examples of the on-site energy parameterizations are shown in Fig. 3.13. This simple model is seen to describe the band structures very well. The values of the on-site shifts are listed in Table 3.1.

The case of diluted doping is studied in order to determine the doping level and activation energy of the dopants. Unit cells of diluted doping are constructed from $N \times N$ of the precursor CHP molecules containing only a single dopant. The impurity band becomes more flat and eventually nearly dispersionless as the cell size increases and the impurity becomes more isolated. For on-site shifts away from zero, this converges for small cell sizes. However, for energy shifts close to zero, the convergence is quite bad, and large cells are

Impurity hydrogenation	0	1	2
Boron Δ [eV]	3.22	8.20	–
Nitrogen Δ [eV]	−0.88	−2.12	−6.94

Table 3.1: Values of Δ by fitting TB to DFT for boron and nitrogen doping and for different hydrogen terminations at the impurity.

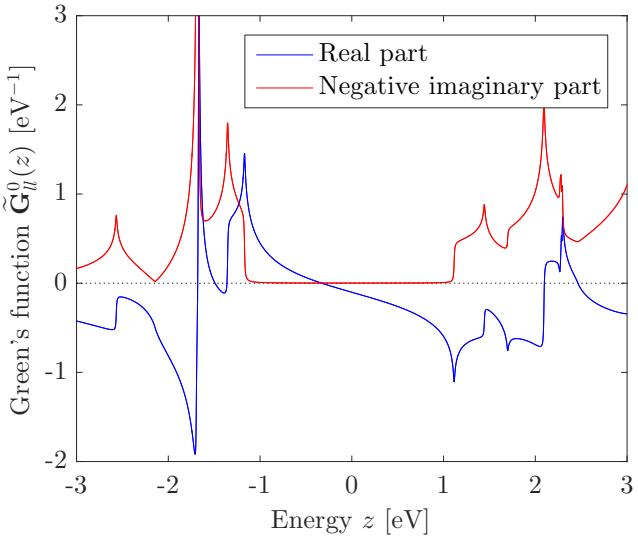

Fig. 3.14: Green's function for the impurity site of the GAL with a broadening of 5 meV.

required, as the dopant is more shallow and thus hybridizes over larger distances. The aim is to describe the activation energy of the system with respect to the impurity on-site energy shift. This may be achieved by calculating TB band structures for impurity concentrations where the impurity band is nearly dispersionless. Because convergence has to be ensured and the systems can be very large, this is computationally demanding. The doping level may be calculated more efficiently using Green's functions. In case of modeling the impurity by only shifting the on-site potential, the impurity perturbed Green's function at site l is simply given by [93]

$$\mathbf{G}_{ll}(z) = \frac{\mathbf{G}^0_{ll}(z)}{1 - \Delta\widetilde{\mathbf{G}}^0_{ll}(z)}, \tag{3.2}$$

where the Green's functions are given by $\mathbf{G}_0(z) = (z - \mathbf{S}^{-1}\mathbf{H}_0)^{-1}$ and $\widetilde{\mathbf{G}}_0(z) = (z\mathbf{S} - \mathbf{H}_0)^{-1}$. The local Green's function at the impurity site of the GAL is shown in Fig. 3.14, where the band gap is clearly identified as the region where the imaginary part is zero. For completely isolated dopants in a semiconductor, the doping level becomes a pole contribution in the local density of states (LDOS), which approaches a Dirac delta function for vanishing broadening. The energy at which this delta function shows up, i.e., the doping level, may be evaluated using Eq. 3.2. The impurity LDOS may be expressed as $L(\omega) = -\pi^{-1}\mathrm{Im}\{\mathbf{G}_{ll}(\omega)\}$, which diverges when $\mathrm{Re}\{\widetilde{\mathbf{G}}^0_{ll}(z)\} = 1/\Delta$

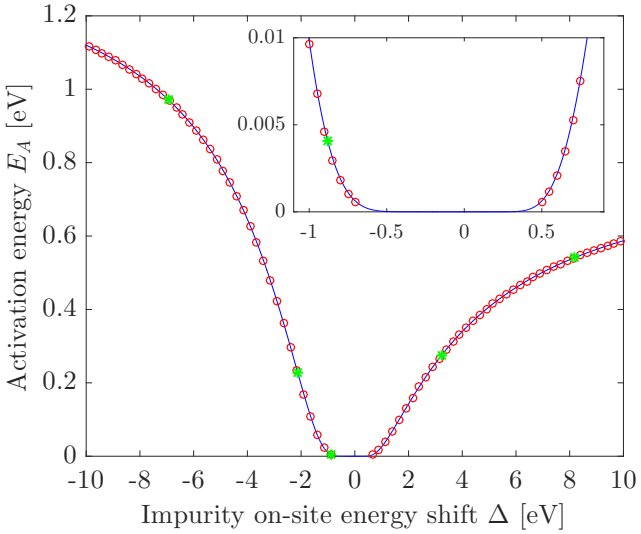

Fig. 3.15: Activation energies of the GAL with respect to the impurity on-site shift. Red circles show results from TB, while the blue line is calculated using the Green's function method. The green asterisks show the activation energies for the fitted values of the on-site shift from the DFT calculations.

and $\mathrm{Im}\{\widetilde{\mathbf{G}}^0_{ll}(z)\} = 0$ are both satisfied. This is a very efficient method for calculating the impurity level for a given on-site potential shift. When the Green's function is known, it is a simple matter to determine the impurity level from the real part of the Green's function. The activation energy is then simply $E_A = E_d - E_v$ for positive Δ corresponding to p-type doping and $E_A = E_c - E_d$ for negative Δ corresponding to n-type doping, where E_d refers to the energy of the doping level and E_v and E_c are the highest (lowest) energy of the valence (conduction) band, respectively. The activation energy with respect to the on-site energy shift is presented in Fig. 3.15. Both the TB and Green's function results are shown and the agreement between the methods is excellent. The inset shows that this continues down to very low activation energies. No TB results are shown in the ± 0.5 eV regime, as this required excessively large unit cells. Note that the Green's function method is not limited to this specific structure, but may be used to determine activation energies of any lattice site in other GALs as long as a TB parameterization is available. The green asterisks show the expected activation energies for boron and nitrogen doping according to the TB parameters from DFT. Notably, nitrogen doping with no impurity hydrogenation leads to a very low activation energy of 4.1 meV.

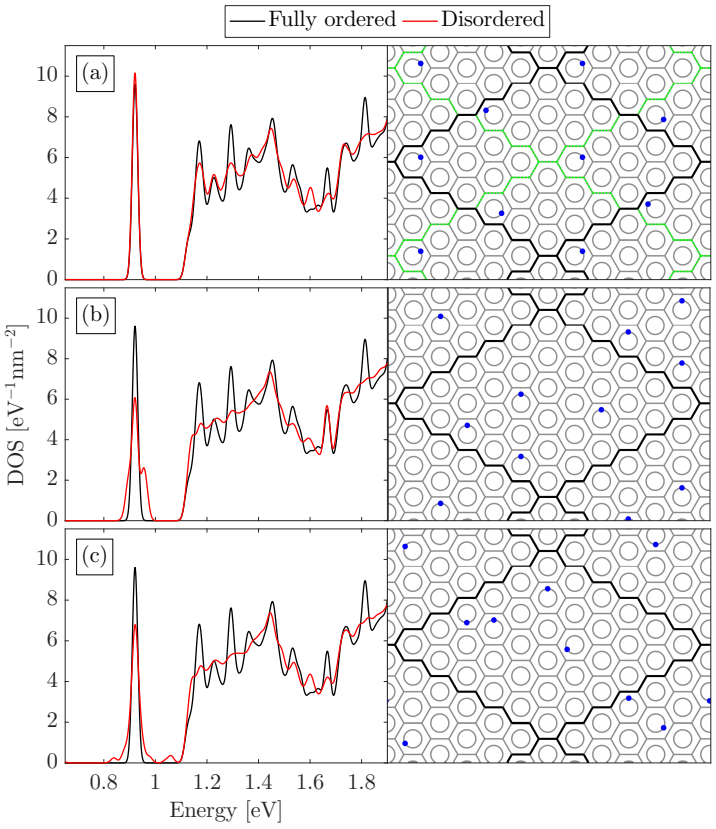

Fig. 3.16: DOS for disordered GALs with every ninth molecule doped using $\Delta = -2$ eV and a broadening of 25 meV. The unit cell in (a), marked by black lines, consists of four subcells, each with a doped molecule at a fixed position and random orientation. The disorder in (b) is fixed orientation and random position and (c) is fully disordered with both random position and orientation.

For the structures in the present study, there is no obvious way to control where the dopants are located. Therefore, the effect of disorder in the form of random position is studied by considering the density of states (DOS). Structures built from mostly pristine and some doped CHP molecules are considered. Figure 3.16 shows the effect of three different types of disorder; (a) fixed molecule position and random orientation, (b) random position and fixed orientation and (c) full disorder with both random position and orientation. The first type of disorder (a) never places the impurities close together. The coupling between impurities is therefore weak, and only marginal changes to the DOS are observed. The peak is broadened for the second type of disorder

(b), where the broadening is more to the right showing a small extra peak. Impurities may be much closer together for this type of disorder and the small extra peak is caused by the case where molecules are adjacent. At full disorder, two small peaks emerge on either side of the main peak, however, these peaks are much smaller than the main peak for this doping concentration. For this type of disorder, impurities in adjacent molecules may be separated by different distances because of the random orientation, whereas adjacent molecules in (b) are often separated by the same distance. This is why the small peak in (b) is not observed for full disorder. The doping properties of these structures seem to be fairly robust against disorder, as the DOS is seen to only be affected to a small extent for this doping concentration even at full disorder.

4 Graphene-embedded iron membranes

Another interesting, yet somewhat completely different, subject that will be discussed in this thesis is the magnetic properties of suspended iron membranes embedded in graphene. This came of interest in 2014 when Zhao *et*

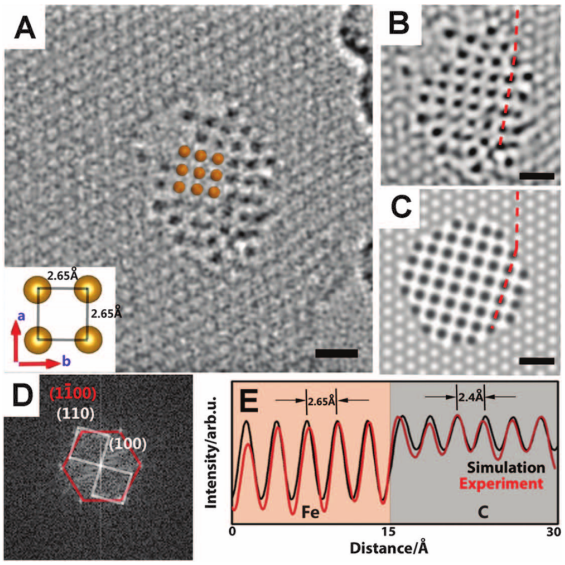

Fig. 3.17: Micrograph measurements of monolayer iron membranes in graphene pores. (a) TEM image showing the square lattice of the iron membrane, (b) smoothed image of (a), (c) simulated image of the monolayer, (d) fast Fourier transform of (a) where the graphene (red) and iron (white) layers are recognized, (e) comparison of intensities of the lines in (b) and (c). All scale bars are 0.6 nm. The figure is from Ref. 107 by Zhao *et al.*

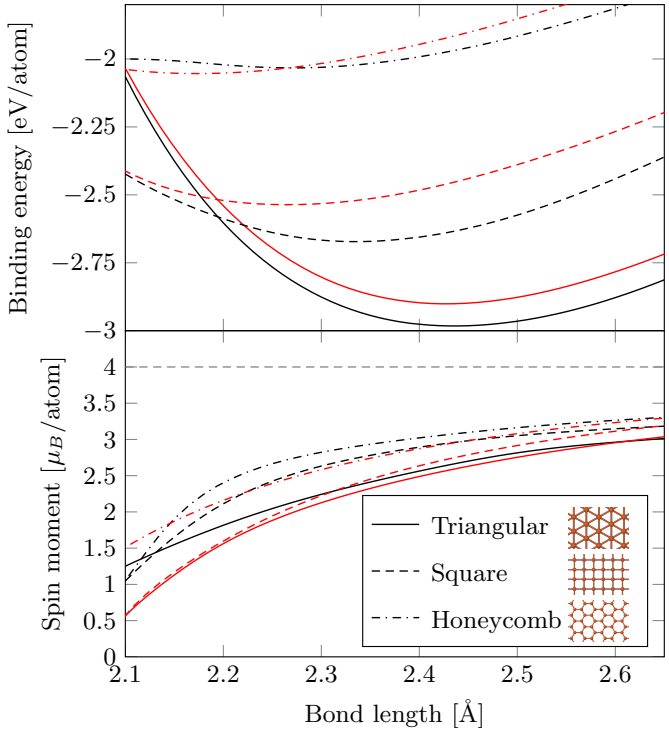

Fig. 3.18: DFT calculations of the binding energy and magnetization of monolayer iron membranes, where black (red) lines correspond to ferromagnetic (antiferromagnetic) configuration. The dashed gray line indicates the spin of free iron.

al. [107] reported that iron membranes may form (and collapse) in pores of suspended graphene under electron irradiation in a transmission electron microscope (TEM) as shown in Fig. 3.17 from their paper. They observed that the membranes are in some cases monolayer iron, and measurements show that they are composed of pure iron. The iron itself is provided by residues form the transfer process. They find that monolayer iron is formed in a square lattice in the pores, where they measure a lattice constant of 2.65 Å, while their DFT calculations indicate 2.35 Å. The deviation is attributed strain effects from embedding the iron in pores. Here, these systems are studied more closely using DFT to better understand their properties. This section is based on the results published in Paper III.

The stability and magnetization of monolayer iron is studied for different lattice configurations. All calculations have been made using the DFT software package ABINIT. A sufficiently converged total energy of the systems

were found for a plane-wave cutoff energy of 435 eV, a Fermi smearing of 0.27 eV, a $16 \times 16 \times 1$ k-grid and an interlayer distance of 10 Å. Binding energies and magnetization of free-standing monolayer iron in a square, triangular and honeycomb lattice are shown in Fig. 3.18 for both ferromagnetic and antiferromagnetic configurations. The ferromagnetic ordering is generally more stable, and the honeycomb lattice is seen to be the least stable of the three. Therefore, only square and triangular lattices in ferromagnetic configuration will be considered in further calculations. The lattice constant for the relaxed square lattice is 2.33 Å with a cost when straining to a lattice constant of 2.65 Å of only 0.2 eV. These values are very close to the theoretical ones reported by Zhao *et al.* However, it is found here that monolayer iron in a triangular lattice is more stable than the square lattice configuration, whereas Zhao *et al.* conclude the opposite. There are a some differences between the calculations. Here, a plane wave basis set and a $16 \times 16 \times 1$ k-point sampling is used, whereas Zhao *et al.* use a localized basis set and a $3 \times 3 \times 1$ k-point sampling. The primitive unit cells of monolayer iron structures are quite small. It is found here that a $3 \times 3 \times 1$ k-point sampling is not sufficient for converged results, leading to the conclusion that the discrepancy arises from the different k-point sampling.

The experimental results show that iron membranes in a square lattice form in the graphene pores, whereas the result in Fig. 3.18 show that the triangular lattice is more stable. In order to better understand how the square lattice might form, the formation kinetics of the monolayer iron membranes are studied by calculating the edge formation energy of the different lattices using

$$E_{\text{edge}} = (E_{\text{total}} - NE_{\text{monolayer}})/2L, \tag{3.3}$$

where E_{total} is the total energy of the nanoribbon unit cell, $E_{\text{monolayer}}$ is the energy per atom of the corresponding lattice, N is the number of atoms in the unit cell of the nanoribbon and L is the width of the unit cell. Figure 3.19 shows the edge formation energy as function of the ribbon width for two types of square and triangular lattices. All calculations are for fully relaxed structures. The figure shows that the edges of both types of square lattices are more stable than the triangular ones, and that the energy difference is about 0.5 eV/nm between the most stable square and triangular lattices. This indicates that a square lattice is more favorable during the formation of the membrane and it may then be kinetically hindered from rearranging to the triangular lattice. The bond lengths through a 16-atom-wide nanoribbon are also shown for the different edge types. It is seen that the bond lengths on the edges are smaller

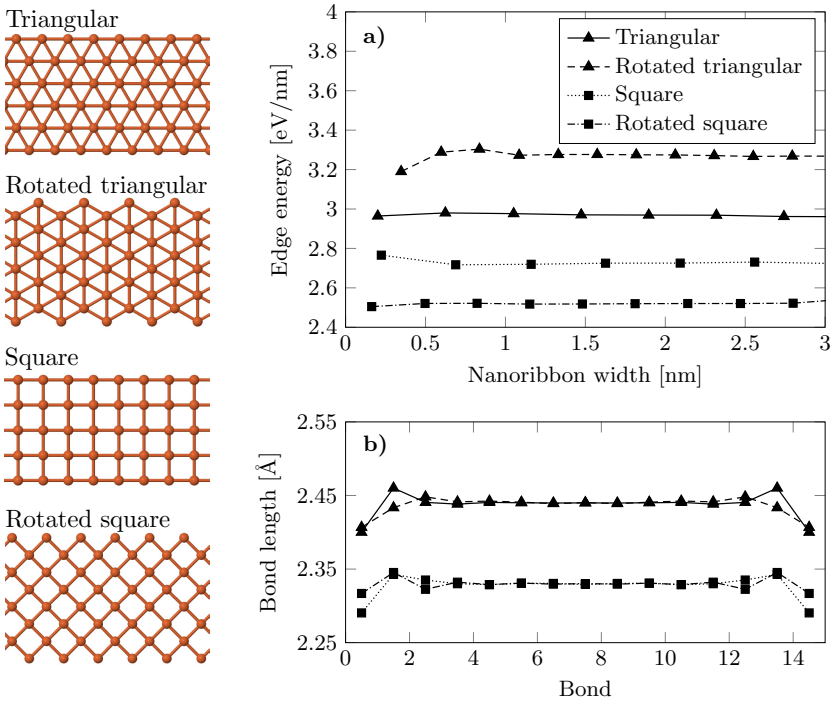

Fig. 3.19: Edge formation energy and bond lengths for two edge types of iron nanoribbons arranged in a square or triangular lattice.

than in the monolayers, indicating that the large lattice constant observed in the experiments is not caused by formation kinetics.

More complex systems with iron embedded in graphene pores have also been studied. Periodic boundary conditions are imposed in order to model the systems using DFT, meaning that the structures effectively become iron-filled GALs. For antidots filled with the same number of iron atoms in either triangular or square configurations, it is possible to compare the total energy of the systems to determine which iron lattice is more stable. In particular, the $\{4, 2\}$ and $\{5, 3\}$ antidot lattices filled with 12 and 21 iron atoms, respectively, are compared in case of triangular and square iron lattices. The fully relaxed versions of these structures are shown in Fig. 3.20, where it is seen that the surrounding graphene is almost unaffected due to its large strength. For the smaller antidots, the iron membrane is seen to bulge more out of plane than for the large antidot. By comparing the total energies, it is found that the triangular lattice is favored in the $\{4, 2\}$ antidot lattice with an energy difference

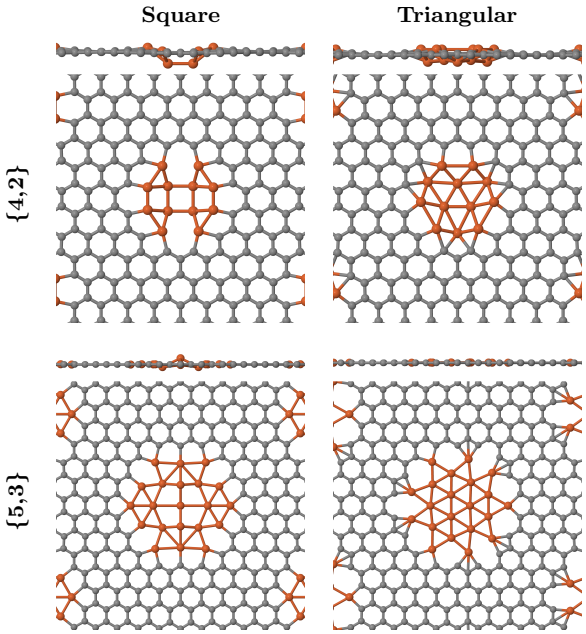

Fig. 3.20: Examples of DFT relaxed GALs with monolayer iron membranes in the antidot in either square or triangular configuration.

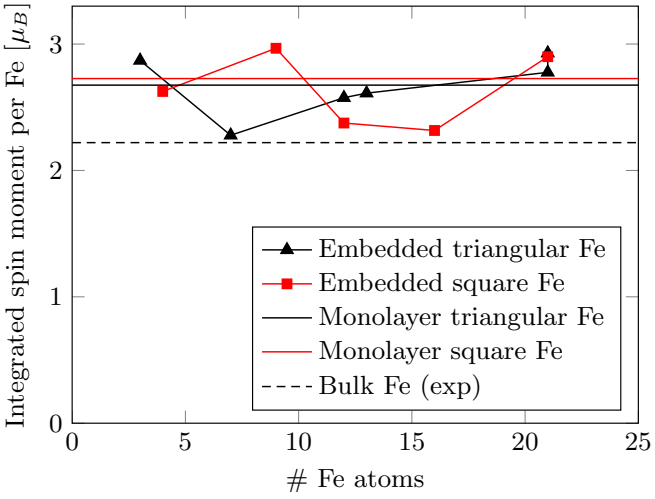

Fig. 3.21: Total spin moment per iron atom of several different structures with varying number of iron atoms in the membrane.

of 2.31 eV. In contrast, the square lattice is favored for the $\{5, 3\}$ antidot lattice with an energy difference of 1.37 eV. The last observation suggests that the binding energy between iron and graphene is larger for the square iron lattice, even though this seems to conform worse. However, for larger iron membranes, the "bulk" behavior of the iron layer should be greater than the effects from the edge or interface, and the triangular iron lattice should be favored. It is possible that there is a regime for small graphene pore sizes that favors the square iron lattice and a regime for larger pores favoring the triangular lattice.

The integrated spin moment per iron atom for the structures in Fig. 3.20 and several other ones are compared in Figure 3.21 for the two iron lattices. The spin per atom is similar for the two lattice types, and it is seen to always be larger than the bulk value and sometimes larger than the monolayer values. Furthermore, the spin moment per iron atom is observed to remain high even for membranes consisting of just a few iron atoms.

5 Second-harmonic generation in bilayer graphene

The final section of this chapter concerns the optical properties of graphene materials, specifically the second-harmonic generation (SHG) in biased bilayer graphene (BLG). This is based on the results in Paper IV which contains more details on the topic. SHG has been studied in many two-dimensional materials, such as MoS_2, WS_2 and WSe_2, where it has proven to be a very useful method for identifying crystal lattice orientation and grain boundaries in polycrystalline samples [110–115]. Even order optical processes require materials that are non-centrosymmetric, meaning that there is no inversion point in the structure. The previously mentioned materials have broken centrosymmetry and therefore show SHG. Graphene is centrosymmetric with inversion points at the center of a hexagon and at the midpoint between two neighbor atoms. BLG is also centrosymmetric with an inversion point between two atoms stacked on top of each other, however, this symmetry may be broken by applying an electric field perpendicular to the layer. Interestingly, BLG becomes semiconducting with a tunable band gap when an electric field is applied. This has been studied both theoretically [27–29] and experimentally [28–32], where a band gap of 250 meV has been achieved.

The imaginary part of the sheet second-harmonic (SH) susceptibility from biased BLG is calculated using Eq. 2.31. For these calculations, an improved triangle integration method for nonlinear response functions has been developed. This significantly lowers the number of k-points necessary, and thus

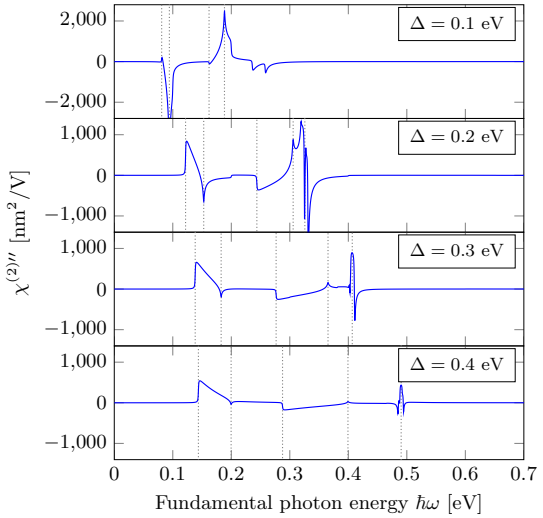

Fig. 3.22: Imaginary part of the sheet SH susceptibility of biased BLG for different values of the electric field strength Δ. The dotted vertical lines are (from left to right) $E_g/2$, $E_{sp}/2$, E_g, E_{sp} and E_r. All spectra include a small broadening of 1 meV.

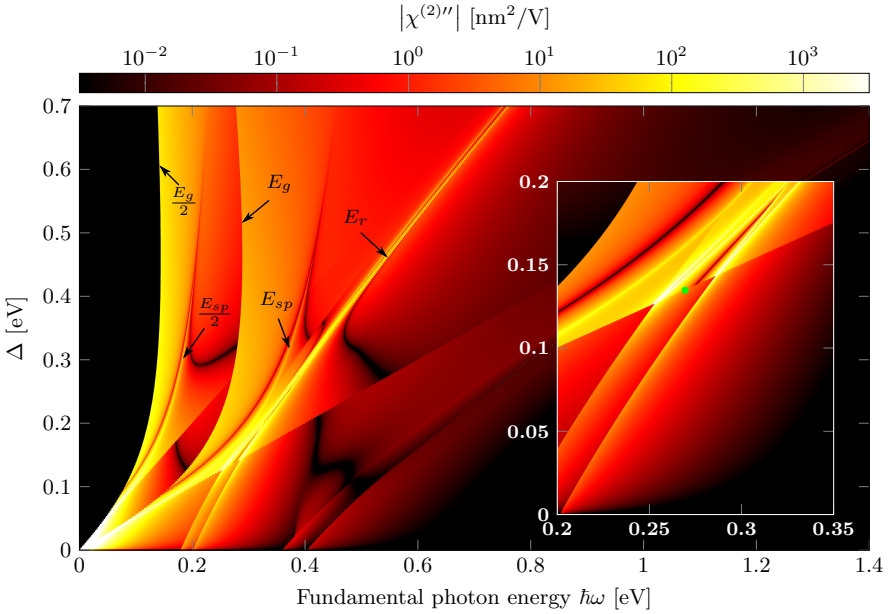

Fig. 3.23: Absolute value of the imaginary part of the sheet SH susceptibility of biased BLG at different photon energies and field strengths. Recognizable features from the band structure are marked in the plot. The double-resonance shows up clearly as a nearly straight line approaching $\Delta = \hbar\omega$. The inset shows a zoom of the onset of the double-resonance, where the approximation (green dot) is seen to fit well.

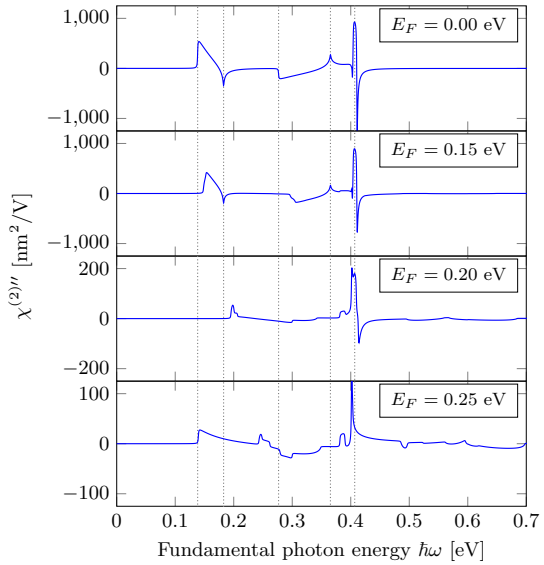

Fig. 3.24: Imaginary part of the sheet SH susceptibility for a field strength of $\Delta = 0.3$ eV for selected values of the Fermi level. The dotted vertical lines are (from left to right) $E_g/2$, $E_{sp}/2$, E_g, E_{sp} and E_r. All spectra include a small broadening of 1 meV.

lowers the computational demand, see Paper III for a detailed explanation. The response is shown in Fig. 3.22 for different values of the field strength. The dotted vertical lines represent recognizable features in the band structure, which are shown in Fig. 2.5. For the lowest field strength ($\Delta = 0.1$ eV), a very large response is observed at low photon energies, which becomes much smaller as the photon energy increases. For this field strength, the band gap and saddle point features are recognized in the response. However, the double-resonance is absent, in agreement with the requirement $\Delta \geq \gamma_1/\sqrt{8} \simeq 0.135$ eV derived earlier. For the larger values of Δ in the figure, the double-resonance emerges and at e.g. $\Delta = 0.3$ eV this is clearly seen as a large peak around a photon energy of 0.4 eV.

A complete picture of the response for numerous field strengths is shown in Fig. 3.23, where the absolute value of the SH susceptibility is shown on a logarithmic scale. The black area at low photon energies is below half the band gap, and the response in this region is exactly zero, as no second-order transitions between the valence and conduction bands are possible. The response is very large at photon energies $E_g/2$ and E_g, and the features from the saddle point are also clearly seen. The figure shows the double-resonance

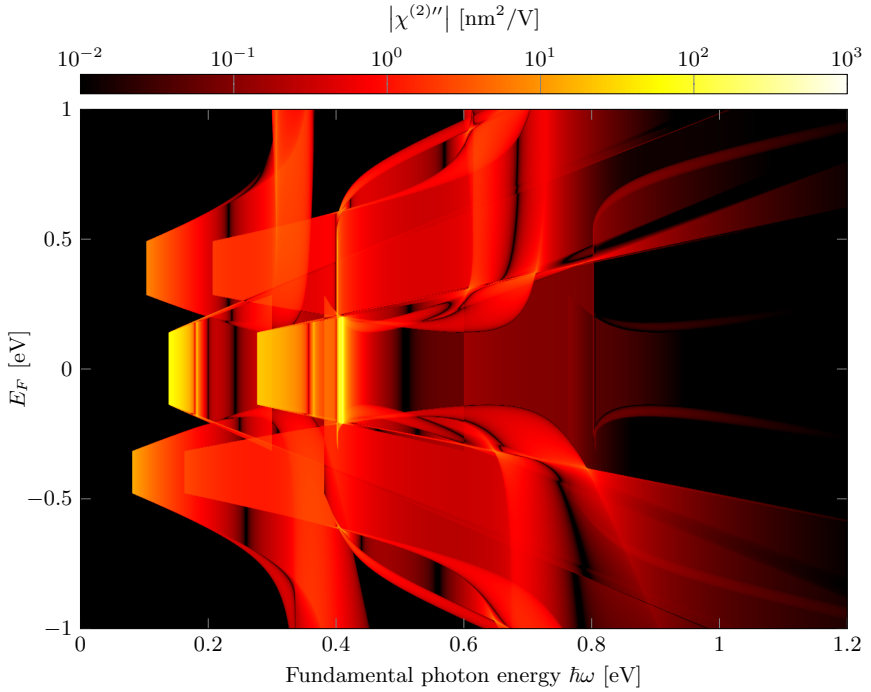

Fig. 3.25: Absolute value of the imaginary part of the sheet SH susceptibility of biased BLG for $\Delta = 0.3$ eV at different photon energies and Fermi levels.

as a distinct feature for field strengths above the threshold, appearing at different photon energies for different Δ. The inset shows a zoom of the onset of the double-resonance, where the approximation is seen to fit excellently. This clearly demonstrates the highly tunable optical properties of this system.

Another method for tuning the SH response from biased BLG is by changing the Fermi level of the system. Figure 3.24 shows the response at selected values of the Fermi level for a field strength of $\Delta = 0.3$ eV, where the band gap is 276 meV. For Fermi levels intersecting the band structure, the allowed transitions (near the K and K' points) are changed due to the Pauli principle. This means that a Fermi level above half the band gap of 138 meV will change the response. The figure shows that a Fermi level of 0.15 eV, which is only slightly above half the band gap, changes the response slightly around $E_g/2$ and E_g. The remaining parts of the spectrum are nearly unchanged. Increasing the Fermi level to 0.2 eV leads to major changes, where most of the features are no longer recognized. The double-resonance is still observed, but its amplitude is

significantly lowered. Increasing the Fermi level even further to 0.25 eV changes the spectrum drastically and none of the original features are recognized.

The response for numerous Fermi levels is shown in Fig. 3.25 for $\Delta = 0.3$ eV. As expected, the spectrum is unchanged when the Fermi level is within $\pm E_g/2$. However, as the Fermi level moves outside this region, the response changes dramatically and is eventually lowered to a few nm^2/V. The expected Pauli blockades at slopes of $\pm 1/2$ and ± 1 are clearly seen in the plot. The figure shows that the response is also highly tunable by changing the Fermi level. However, for a strong response, the Fermi level should be kept within the band gap region.

Chapter 4

Conclusions and perspectives

The aim of this thesis has been to study the electronic and optical properties of semiconducting graphene. Focus has been primarily on the electronic properties of graphene antidot lattices (GALs), where the band gap, transport and doping properties have been investigated. In Paper I, the Dirac equation (DE) is used to develop a continuum model for describing the electronic properties of GALs by solving the DE with a spatially varying mass term. This model is advantageous compared to atomistic models in one key aspect, namely that the computation time is independent of the size of the system. The band structure and optical spectra were compared for selected structures, where it was found that the Dirac model is in excellent agreement with the more accurate atomistic model tight-binding (TB) for systems where no edge states are present. In case of antidots with zigzag edges, which give rise to localized edge states, the Dirac model is not able to reproduce the TB results unless the antidots are very small. Comparing the band gap of numerous GALs lead to the same conclusion. Additionally, an approximation to the Dirac model lead to an analytic description of the band gap, which again was found to agree well with GALs containing antidots with armchair edges.

The focus in Paper II is to use the DE to describe electronic transport though graphene antidot barriers (GABs). The theoretical description, again based on a spatially varying mass term, leads to a Green's tensor area integral equation, which is solved numerically by discretizing the structure. This facilitates calculations of electron scattering in arbitrary graphene antidot systems.

The transmittance through GABs was studied and compared to equivalent TB structures. Again, the conclusion is that the Dirac model is able to accurately reproduce TB results for systems with no edge states. However, the advantage of the Dirac model is again that it is scale invariant and can handle arbitrarily large systems. Furthermore, a simple Dirac mass barrier model is used to efficiently calculate the transport gap. It was found that the transport gap for GABs with zigzag antidots can be significantly larger than the band gap of the corresponding GAL, and that GABs with only a few antidots in the unit cell is sufficient to block the transport in the band gap region.

The electronic properties of graphene nanostructures were studied further in Paper V, which concerns the doping properties of GALs. Density functional theory (DFT) is used to study a specific GAL, which has previously been produced with atomic precision using a bottom-up approach. Doping is introduced by replacing one edge atom with either boron or nitrogen. The band structure of the pristine and doped systems was calculated using DFT, and TB parameterizations were used to accurately describe the properties of diluted doping and disordered systems. Impurities are modeled in TB by simply shifting the on-site energy of the impurity. Boron doping was found to introduce an acceptor level near the valence bands while nitrogen doping introduces a donor level near the conduction bands. A Green's function method was developed for efficiently calculating the activation energy of dopants for any value of the on-site shift, and a comparison with TB revealed very good agreement. The GAL in this study is very small and only one site and two dopants were considered. However, this work is the first step on the way to understanding the doping properties of GALs, which are important for electronics applications.

A somewhat unrelated topic was discussed in Paper III, namely the stability and magnetic properties of iron membranes embedded in graphene nanopores. This came of interest after it was realized experimentally, showing iron in a square lattice with a lattice constant of 2.65 Å. In Paper III, DFT calculation of monolayer iron in different lattice configurations were performed, showing that the most stable version is a triangular lattice with a lattice constant of 2.44 Å. The formation kinetics of the iron membrane was studied in order to explain the difference between the theory and experiment. The edge formation energy for different lattices and edge types were carried out for iron nanoribbons, which revealed that the edge formation energy is lower for the square lattice than the triangular lattice. DFT was also used to study iron membranes in GALs, where it was observed that the square lattice is more stable in some cases. It

is speculated that there is a regime of small membrane size where the edge formation makes the square lattice favorable. However, for large membranes, the bulk stability should turn the iron membrane into the triangular lattice.

Another different topic was studied in Paper IV, where the second-harmonic optical response from biased bilayer graphene (BLG) was calculated. Second-harmonic generation (SHG) requires materials that are non-centrosymmetric, which is achieved in BLG by applying a perpendicular electric field. This opens up a band gap tunable by the strength of the electric field. It turns out that biased BLG also shows strong SHG that is tunable by the field strength. A strong double-resonance appears in the spectrum for field strengths above a threshold value. The photon energy at which this double-resonance appears is described analytically using the Dirac approximation. Furthermore, the SH response is tunable by varying the Fermi level, however, for a strong response, the Fermi level should be in the band gap.

The next step in studying graphene for nanoelectronics applications would be to study the doping properties of other GALs, which might also include effects such as disorder. Furthermore, such doped systems could be put together to form junctions for which the transport properties would be a very interesting research topic. The experimental research in graphene nanostructures is constantly advancing, and new measurements together with a thorough theoretical understanding could pave the way for functional nanoelectronic devices based on graphene.

References

[1] K. S. Novoselov, A. K. Geim, S. V. Morozov, D. Jiang, Y. Zhang, S. V. Dubonos, I. V. Grigorieva, and A. A. Firsov, Science **306**, 666 (2004).

[2] X. Li, W. Cai, J. An, S. Kim, J. Nah, D. Yang, R. Piner, A. Velamakanni, I. Jung, E. Tutuc, *et al.*, Science **324**, 1312 (2009).

[3] Y. Zhang, L. Zhang, and C. Zhou, Accounts Chem. Res. **46**, 2329 (2013).

[4] Q. Yu, J. Lian, S. Siriponglert, H. Li, Y. P. Chen, and S.-S. Pei, Appl. Phys. Lett. **93**, 113103 (2008).

[5] L. G. De Arco, Y. Zhang, A. Kumar, and C. Zhou, IEEE T. Nanotechnol. **8**, 135 (2009).

[6] A. Reina, X. Jia, J. Ho, D. Nezich, H. Son, V. Bulovic, M. S. Dresselhaus, and J. Kong, Nano Lett. **9**, 30 (2008).

[7] K. S. Kim, Y. Zhao, H. Jang, S. Y. Lee, J. M. Kim, K. S. Kim, J.-H. Ahn, P. Kim, J.-Y. Choi, and B. H. Hong, Nature **457**, 706 (2009).

[8] A. E. Karu and M. Beer, J. Appl. Phys. **37**, 2179 (1966).

[9] P. R. Wallace, Phys. Rev. **71**, 622 (1947).

[10] K. F. Mak, C. Lee, J. Hone, J. Shan, and T. F. Heinz, Phys. Rev. Lett. **105**, 136805 (2010).

[11] B. Radisavljevic, A. Radenovic, J. Brivio, i. V. Giacometti, and A. Kis, Nat. Nanotechnol. **6**, 147 (2011).

[12] J. K. Ellis, M. J. Lucero, and G. E. Scuseria, Appl. Phys. Lett. **99**, 261908 (2011).

[13] Y.-H. Lee, X.-Q. Zhang, W. Zhang, M.-T. Chang, C.-T. Lin, K.-D. Chang, Y.-C. Yu, J. T.-W. Wang, C.-S. Chang, L.-J. Li, *et al.*, Adv. Mater. **24**, 2320 (2012).

[14] H. Ramakrishna Matte, A. Gomathi, A. K. Manna, D. J. Late, R. Datta, S. K. Pati, and C. Rao, Angew. Chem. **122**, 4153 (2010).

[15] H. R. Gutiérrez, N. Perea-López, A. L. Elías, A. Berkdemir, B. Wang, R. Lv, F. López-Urías, V. H. Crespi, H. Terrones, and M. Terrones, Nano Lett. **13**, 3447 (2012).

[16] P. Tonndorf, R. Schmidt, P. Böttger, X. Zhang, J. Börner, A. Liebig, M. Albrecht, C. Kloc, O. Gordan, D. R. Zahn, *et al.*, Opt. Express **21**, 4908 (2013).

[17] Y. Zhang, T.-R. Chang, B. Zhou, Y.-T. Cui, H. Yan, Z. Liu, F. Schmitt, J. Lee, R. Moore, Y. Chen, *et al.*, Nat. Nanotechnol. **9**, 111 (2014).

[18] H. Liu, A. T. Neal, Z. Zhu, Z. Luo, X. Xu, D. Tománek, and P. D. Ye, ACS Nano **8**, 4033 (2014).

[19] P. Vogt, P. De Padova, C. Quaresima, J. Avila, E. Frantzeskakis, M. C. Asensio, A. Resta, B. Ealet, and G. Le Lay, Phys. Rev. Lett. **108**, 155501 (2012).

[20] M. Dávila, L. Xian, S. Cahangirov, A. Rubio, and G. Le Lay, New J. Phys. **16**, 095002 (2014).

[21] F.-f. Zhu, W.-j. Chen, Y. Xu, C.-l. Gao, D.-d. Guan, C.-h. Liu, D. Qian, S.-C. Zhang, and J.-f. Jia, Nat. Mater. **14**, 1020 (2015).

[22] K. I. Bolotin, K. Sikes, Z. Jiang, M. Klima, G. Fudenberg, J. Hone, P. Kim, and H. Stormer, Solid State Commun. **146**, 351 (2008).

[23] K. S. Novoselov, D. Jiang, F. Schedin, T. J. Booth, V. V. Khotkevich, S. V. Morozov, and A. K. Geim, P. Natl. Acad. Sci. USA **102**, 10451 (2005).

[24] Y. Zhang, Y.-W. Tan, H. L. Stormer, and P. Kim, Nature **438**, 201 (2005).

[25] R. R. Nair, P. Blake, A. N. Grigorenko, K. S. Novoselov, T. J. Booth, T. Stauber, N. M. R. Peres, and A. K. Geim, Science **320**, 1308 (2008).

[26] C. Lee, X. Wei, J. W. Kysar, and J. Hone, Science **321**, 385 (2008).

[27] E. McCann, Phys. Rev. B **74**, 161403 (2006).

[28] E. V. Castro, K. Novoselov, S. Morozov, N. Peres, J. L. Dos Santos, J. Nilsson, F. Guinea, A. Geim, and A. C. Neto, Phys. Rev. Lett. **99**, 216802 (2007).

[29] L. Zhang, Z. Li, D. N. Basov, M. Fogler, Z. Hao, and M. C. Martin, Phys. Rev. B **78**, 235408 (2008).

[30] T. Ohta, A. Bostwick, T. Seyller, K. Horn, and E. Rotenberg, Science **313**, 951 (2006).

[31] Y. Zhang, T.-T. Tang, C. Girit, Z. Hao, M. C. Martin, A. Zettl, M. F. Crommie, Y. R. Shen, and F. Wang, Nature **459**, 820 (2009).

[32] K. F. Mak, C. H. Lui, J. Shan, and T. F. Heinz, Phys. Rev. Lett. **102**, 256405 (2009).

[33] F. Xia, D. B. Farmer, Y.-m. Lin, and P. Avouris, Nano Lett. **10**, 715 (2010).

[34] J. G. Pedersen and T. G. Pedersen, Phys. Rev. B **85**, 235432 (2012).

[35] P. Recher and B. Trauzettel, Nanotechnology **21**, 302001 (2010).

[36] F. Molitor, J. Güttinger, C. Stampfer, S. Dröscher, A. Jacobsen, T. Ihn, and K. Ensslin, J. Phys.: Condens. Matter **23**, 243201 (2011).

[37] J. Güttinger, F. Molitor, C. Stampfer, S. Schnez, A. Jacobsen, S. Dröscher, T. Ihn, and K. Ensslin, Rep. Prog. Phys. **75**, 126502 (2012).

[38] B. S. Kandemir and G. Omer, Eur. Phys. J. B **86**, 299 (2013).

[39] B. Obradovic, R. Kotlyar, F. Heinz, P. Matagne, T. Rakshit, M. Giles, M. Stettler, and D. Nikonov, Appl. Phys. Lett. **88**, 142102 (2006).

[40] Y.-W. Son, M. L. Cohen, and S. G. Louie, Phys. Rev. Lett. **97**, 216803 (2006).

[41] M. Y. Han, B. Özyilmaz, Y. Zhang, and P. Kim, Phys. Rev. Lett. **98**, 206805 (2007).

[42] R. Balog, B. Jørgensen, L. Nilsson, M. Andersen, E. Rienks, M. Bianchi, M. Fanetti, E. Lægsgaard, A. Baraldi, S. Lizzit, *et al.*, Nat. Mater. **9**, 315 (2010).

[43] T. G. Pedersen, C. Flindt, J. Pedersen, N. A. Mortensen, A.-P. Jauho, and K. Pedersen, Phys. Rev. Lett. **100**, 136804 (2008).

[44] J. A. Fürst, T. G. Pedersen, M. Brandbyge, and A.-P. Jauho, Phys. Rev. B **80**, 115117 (2009).

[45] J. A. Fürst, J. G. Pedersen, C. Flindt, N. A. Mortensen, M. Brandbyge, T. G. Pedersen, and A.-P. Jauho, New J. Phys. **11**, 095020 (2009).

[46] R. Petersen and T. G. Pedersen, Phys. Rev. B **80**, 113404 (2009).

[47] M. Vanević, V. M. Stojanović, and M. Kindermann, Phys. Rev. B **80**, 045410 (2009).

[48] M. L. Trolle, U. S. Møller, and T. G. Pedersen, Phys. Rev. B **88**, 195418 (2013).

[49] F. Ouyang, S. Peng, Z. Liu, and Z. Liu, ACS Nano **5**, 4023 (2011).

[50] R. Petersen, T. G. Pedersen, and A.-P. Jauho, ACS Nano **5**, 523 (2010).

[51] M. Dvorak, W. Oswald, and Z. Wu, Sci. Rep. **3** (2013).

[52] M. Fujita, K. Wakabayashi, K. Nakada, and K. Kusakabe, J. Phys. Soc. Jpn. **65**, 1920 (1996).

[53] K. Wakabayashi, K.-i. Sasaki, T. Nakanishi, and T. Enoki, Sci. Technol. Adv. Mater. **11**, 054504 (2010).

[54] C. Tao, L. Jiao, O. V. Yazyev, Y.-C. Chen, J. Feng, X. Zhang, R. B. Capaz, J. M. Tour, A. Zettl, S. G. Louie, *et al.*, Nat. Phys. **7**, 616 (2011).

[55] J. Eroms and D. Weiss, New J. Phys. **11**, 095021 (2009).

[56] A. Giesbers, E. Peters, M. Burghard, and K. Kern, Phys. Rev. B **86**, 045445 (2012).

[57] J. Bai, X. Zhong, S. Jiang, Y. Huang, and X. Duan, Nat. Nanotechnol. **5**, 190 (2010).

[58] M. Kim, N. S. Safron, E. Han, M. S. Arnold, and P. Gopalan, Nano Lett. **10**, 1125 (2010).

[59] M. Kim, N. S. Safron, E. Han, M. S. Arnold, and P. Gopalan, ACS Nano **6**, 9846 (2012).

[60] Z. Zeng, X. Huang, Z. Yin, H. Li, Y. Chen, H. Li, Q. Zhang, J. Ma, F. Boey, and H. Zhang, Adv. Mater. **24**, 4138 (2012).

[61] M. Wang, L. Fu, L. Gan, C. Zhang, M. Rümmeli, A. Bachmatiuk, K. Huang, Y. Fang, and Z. Liu, Sci. Rep. **3**, 1238 (2013).

[62] X. Liang, Y.-S. Jung, S. Wu, A. Ismach, D. L. Olynick, S. Cabrini, and J. Bokor, Nano Lett. **10**, 2454 (2010).

[63] Q. Xu, M.-Y. Wu, G. F. Schneider, L. Houben, S. K. Malladi, C. Dekker, E. Yucelen, R. E. Dunin-Borkowski, and H. W. Zandbergen, ACS Nano **7**, 1566 (2013).

[64] F. Oberhuber, S. Blien, S. Heydrich, F. Yaghobian, T. Korn, C. Schüller, C. Strunk, D. Weiss, and J. Eroms, Appl. Phys. Lett. **103**, 143111 (2013).

[65] X. Jia, M. Hofmann, V. Meunier, B. G. Sumpter, J. Campos-Delgado, J. M. Romo-Herrera, H. Son, Y.-P. Hsieh, A. Reina, J. Kong, *et al.*, Science **323**, 1701 (2009).

[66] Ç. Ö. Girit, J. C. Meyer, R. Erni, M. D. Rossell, C. Kisielowski, L. Yang, C.-H. Park, M. Crommie, M. L. Cohen, S. G. Louie, *et al.*, Science **323**, 1705 (2009).

[67] A. P. Seitsonen, A. M. Saitta, T. Wassmann, M. Lazzeri, and F. Mauri, Phys. Rev. B **82**, 115425 (2010).

[68] F. Schwierz, Nat. Nanotechnol. **5**, 487 (2010).

[69] T. G. Pedersen and J. G. Pedersen, J. Appl. Phys. **112**, 113715 (2012).

[70] T. Gunst, T. Markussen, A.-P. Jauho, and M. Brandbyge, Phys. Rev. B **84**, 155449 (2011).

[71] J. G. Pedersen, T. Gunst, T. Markussen, and T. G. Pedersen, Phys. Rev. B **86**, 245410 (2012).

[72] S. Berrada, V. H. Nguyen, D. Querlioz, J. Saint-Martin, A. Alarcón, C. Chassat, A. Bournel, and P. Dollfus, Appl. Phys. Lett. **103**, 183509 (2013).

[73] D. A. Areshkin, D. Gunlycke, and C. T. White, Nano Lett. **7**, 204 (2007).

[74] E. R. Mucciolo, A. C. Neto, and C. H. Lewenkopf, Phys. Rev. B **79**, 075407 (2009).

[75] D. V. Kosynkin, A. L. Higginbotham, A. Sinitskii, J. R. Lomeda, A. Dimiev, B. K. Price, and J. M. Tour, Nature **458**, 872 (2009).

[76] L. Jiao, L. Zhang, X. Wang, G. Diankov, and H. Dai, Nature **458**, 877 (2009).

[77] S. Yuan, R. Roldán, A.-P. Jauho, and M. Katsnelson, Phys. Rev. B **87**, 085430 (2013).

[78] S. R. Power and A.-P. Jauho, Phys. Rev. B **90**, 115408 (2014).

[79] J. Cai, P. Ruffieux, R. Jaafar, M. Bieri, T. Braun, S. Blankenburg, M. Muoth, A. P. Seitsonen, M. Saleh, X. Feng, *et al.*, Nature **466**, 470 (2010).

[80] C. Bronner, S. Stremlau, M. Gille, F. Brauße, A. Haase, S. Hecht, and P. Tegeder, Angew. Chem. Int. Ed. **52**, 4422 (2013).

[81] J. Cai, C. A. Pignedoli, L. Talirz, P. Ruffieux, H. Söde, L. Liang, V. Meunier, R. Berger, R. Li, X. Feng, *et al.*, Nat. Nanotech. **9**, 896 (2014).

[82] A. Lherbier, L. Liang, J.-C. Charlier, and V. Meunier, Carbon **95**, 833 (2015).

[83] J. Mahmood, E. K. Lee, M. Jung, D. Shin, I.-Y. Jeon, S.-M. Jung, H.-J. Choi, J.-M. Seo, S.-Y. Bae, S.-D. Sohn, *et al.*, Nat. Commun. **6**, 6486 (2015).

[84] C. Sánchez-Sánchez, S. Brüller, H. Sachdev, K. Müllen, M. Krieg, H. F. Bettinger, A. Nicolaï, V. Meunier, L. Talirz, R. Fasel, *et al.*, ACS Nano **9**, 9228 (2015).

[85] M. Bieri, M. Treier, J. Cai, K. Aït-Mansour, P. Ruffieux, O. Gröning, P. Gröning, M. Kastler, R. Rieger, X. Feng, *et al.*, Chem. Commun. **45**, 6919 (2009).

[86] H. Terrones, R. Lv, M. Terrones, and M. S. Dresselhaus, Rep. Prog. Phys. **75**, 062501 (2012).

[87] R. Czerw, M. Terrones, J.-C. Charlier, X. Blase, B. Foley, R. Kamalakaran, N. Grobert, H. Terrones, D. Tekleab, P. Ajayan, *et al.*, Nano Lett. **1**, 457 (2001).

[88] X. Wang, X. Li, L. Zhang, Y. Yoon, P. K. Weber, H. Wang, J. Guo, and H. Dai, Science **324**, 768 (2009).

[89] D. Wei, Y. Liu, Y. Wang, H. Zhang, L. Huang, and G. Yu, Nano Lett. **9**, 1752 (2009).

[90] D. Usachov, O. Vilkov, A. Gruneis, D. Haberer, A. Fedorov, V. Adamchuk, A. Preobrajenski, P. Dudin, A. Barinov, M. Oehzelt, *et al.*, Nano Lett. **11**, 5401 (2011).

[91] A. Lherbier, X. Blase, Y.-M. Niquet, F. Triozon, and S. Roche, Phys. Rev. Lett. **101**, 036808 (2008).

[92] A. Lherbier, A. R. Botello-Mendez, and J.-C. Charlier, Nano Lett. **13**, 1446 (2013).

[93] T. G. Pedersen and J. G. Pedersen, Phys. Rev. B **87**, 155433 (2013).

[94] T. G. Pedersen, Phys. Rev. B **91**, 085428 (2015).

[95] B. Huang, Q. Yan, G. Zhou, J. Wu, B.-L. Gu, W. Duan, and F. Liu, Appl. Phys. Lett. **91**, 253122 (2007).

[96] Q. Yan, B. Huang, J. Yu, F. Zheng, J. Zang, J. Wu, B.-L. Gu, F. Liu, and W. Duan, Nano Lett. **7**, 1469 (2007).

[97] Y. Li, Z. Zhou, P. Shen, and Z. Chen, ACS Nano **3**, 1952 (2009).

[98] X. Wang, Z. Hou, T. Ikeda, S.-F. Huang, K. Terakura, M. Boero, M. Oshima, M.-a. Kakimoto, and S. Miyata, Phys. Rev. B **84**, 245434 (2011).

[99] J. Zhou, Q. Wang, Q. Sun, X. Chen, Y. Kawazoe, and P. Jena, Nano Lett. **9**, 3867 (2009).

[100] P. O. Lehtinen, A. S. Foster, Y. Ma, A. V. Krasheninnikov, and R. M. Nieminen, Phys. Rev. Lett. **93**, 187202 (2004).

[101] S. Haldar, B. S. Pujari, S. Bhandary, F. Cossu, O. Eriksson, D. G. Kanhere, and B. Sanyal, Phys. Rev. B **89**, 205411 (2014).

[102] I. Zanella, S. B. Fagan, R. Mota, and A. Fazzio, J. Phys. Chem. C **112**, 9163 (2008).

[103] A. V. Krasheninnikov, P. O. Lehtinen, A. S. Foster, P. Pyykkö, and R. M. Nieminen, Phys. Rev. Lett. **102**, 126807 (2009).

[104] E. J. G. Santos, A. Ayuela, and D. Sánchez-Portal, New J. Phys. **12**, 053012 (2010).

[105] Z. He, K. He, A. W. Robertson, A. I. Kirkland, D. Kim, J. Ihm, E. Yoon, G.-D. Lee, and J. H. Warner, Nano Lett. **14**, 3766 (2014).

[106] J. A. Rodrígues-Manzo, O. Cretu, and F. Banhart, ACS Nano **4**, 3422 (2010).

[107] J. Zhao, Q. Deng, A. Bachmatiuk, G. Sandeep, A. Popov, J. Eckert, and M. H. Rümmeli, Science **343**, 1228 (2014).

[108] T. G. Pedersen, A.-P. Jauho, and K. Pedersen, Phys. Rev. B **79**, 113406 (2009).

[109] T. G. Pedersen, C. Flindt, J. Pedersen, A.-P. Jauho, N. A. Mortensen, and K. Pedersen, Phys. Rev. B **77**, 245431 (2008).

[110] L. M. Malard, T. V. Alencar, A. P. M. Barboza, K. F. Mak, and A. M. de Paula, Phys. Rev. B **87**, 201401 (2013).

[111] N. Kumar, S. Najmaei, Q. Cui, F. Ceballos, P. M. Ajayan, J. Lou, and H. Zhao, Phys. Rev. B **87**, 161403 (2013).

[112] X. Yin, Z. Ye, D. A. Chenet, Y. Ye, K. O'Brien, J. C. Hone, and X. Zhang, Science **344**, 488 (2014).

[113] C. Janisch, Y. Wang, D. Ma, N. Mehta, A. L. Elías, N. Perea-López, M. Terrones, V. Crespi, and Z. Liu, Sci. Rep. **4** (2014).

[114] H. Zeng, G.-B. Liu, J. Dai, Y. Yan, B. Zhu, R. He, L. Xie, S. Xu, X. Chen, W. Yao, *et al.*, Sci. Rep. **3** (2013).

[115] W.-T. Hsu, Z.-A. Zhao, L.-J. Li, C.-H. Chen, M.-H. Chiu, P.-S. Chang, Y.-C. Chou, and W.-H. Chang, ACS Nano **8**, 2951 (2014).

[116] M. L. Trolle, G. Seifert, and T. G. Pedersen, Phys. Rev. B **89**, 235410 (2014).

[117] T. G. Pedersen and K. Pedersen, Phys. Rev. B **79**, 035422 (2009).

[118] L. Golub and S. Tarasenko, Phys. Rev. B **90**, 201402 (2014).

[119] S. Mikhailov, Phys. Rev. B **84**, 045432 (2011).

[120] S.-Y. Hong, J. I. Dadap, N. Petrone, P.-C. Yeh, J. Hone, and R. M. Osgood Jr, Phys. Rev. X **3**, 021014 (2013).

[121] S. Wu, L. Mao, A. M. Jones, W. Yao, C. Zhang, and X. Xu, Nano Lett. **12**, 2032 (2012).

[122] P. Hohenberg and W. Kohn, Phys. Rev. **136**, B864 (1964).

[123] W. Kohn and L. J. Sham, Phys. Rev. **140**, A1133 (1965).

[124] M. L. Cohen and J. R. Chelikowsky, *Electronic Structure and Optical Spectra of Semiconductors*, 2nd ed. (Springer-Verlag, 1988).

[125] K. Burke and L. O. Wagner, Int. J. Quantum Chem. **113**, 96 (2013).

[126] R. Godby, M. Schlüter, and L. Sham, Phys. Rev. Lett. **56**, 2415 (1986).

[127] R. Godby, M. Schlüter, and L. Sham, Phys. Rev. B **37**, 10159 (1988).

[128] M. S. Hybertsen and S. G. Louie, Phys. Rev. Lett. **55**, 1418 (1985).

[129] J. Muscat, A. Wander, and N. Harrison, Chem. Phys. Lett. **342**, 397 (2001).

[130] W. Foulkes, L. Mitas, R. Needs, and G. Rajagopal, Rev. Mod. Phys. **73**, 33 (2001).

[131] R. Saito, G. Dresselhaus, and M. S. Dresselhaus, *Physical Properties of Carbon Nanotubes*, 2nd ed. (Imperial College Press, 1998).

[132] S. Reich, J. Maultzsch, C. Thomsen, and P. Ordejon, Phys. Rev. B **66**, 035412 (2002).

[133] S.-W. Lee and R. Mittra, IEEE T. Antenn. Propag. **31**, 99 (1983).

[134] T. Søndergaard, Phys. Status Solidi B **244**, 3448 (2007).

[135] L. Novotny and B. Hecht, *Principles of nano-optics* (Cambridge University Press, 2006).

[136] M. Abramovitz and I. A. Stegun, eds., *Handbook of mathematical functions* (Dover Publications, 1965).

[137] B. T. Draine, Astrophys. J. **333**, 848 (1988).

[138] E. McCann and M. Koshino, Rep. Prog. Phys. **76**, 056503 (2013).

[139] L. Brey and H. Fertig, Phys. Rev. B **73**, 235411 (2006).

[140] S. Heydrich, M. Hirmer, C. Preis, T. Korn, J. Eroms, D. Weiss, and C. Schüller, Appl. Phys. Lett. **97**, 043113 (2010).

[141] A. Du, Z. Zhu, and S. C. Smith, J. Am. Chem. Soc. **132**, 2876 (2010).

[142] Y. Li, Z. Zhou, P. Shen, and Z. Chen, Chem. Commun. **46**, 3672 (2010).

Publications

[I] **S. J. Brun**, M. R. Thomsen and T. G. Pedersen, "*Electronic and optical properties of graphene antidot lattices: comparison of Dirac and tight-binding models,*" Journal of Physics: Condensed Matter, **26**, 265301 (2014).

[II] M. R. Thomsen, **S. J. Brun** and T. G. Pedersen, "*Dirac model of electronic transport in graphene antidot barriers,*" Journal of Physics: Condensed Matter, **26**, 335301 (2014).

[III] M. R. Thomsen, **S. J. Brun** and T. G. Pedersen, "*Stability and magnetization of free-standing and graphene-embedded iron membranes,*" Physical Review B, **91**, 125439 (2015).

[IV] **S. J. Brun** and T. G. Pedersen, "*Intense and tunable second-harmonic generation in biased bilayer graphene,*" Physical Review B, **91**, 205405 (2015).

[V] **S. J. Brun**, V. M. Pereira and T. G. Pedersen, "*Boron and nitrogen doping in graphene antidot lattices,*" Physical Review B, **93**, 245420 (2016).

Paper I

Electronic and optical properties of graphene antidot lattices: comparison of Dirac and tight-binding models

Søren Jacob Brun, Morten Rishøj Thomsen and Thomas Garm Pedersen

The paper has been published in
Journal of Physics: Condensed matter **26**, 265301 (2014)

IOP Publishing Journal of Physics: Condensed Matter
J. Phys.: Condens. Matter **26** (2014) 265301 (8pp) doi:10.1088/0953-8984/26/26/265301

Electronic and optical properties of graphene antidot lattices: comparison of Dirac and tight-binding models

S J Brun, M R Thomsen and T G Pedersen

Department of Physics and Nanotechnology, Aalborg University, Skjernvej 4A, DK-9220 Aalborg Øst, Denmark
Center for Nanostructured Graphene (CNG), DK-9220 Aalborg Øst, Denmark

E-mail: sjb@nano.aau.dk

Received 3 March 2014, revised 21 April 2014
Accepted for publication 25 April 2014
Published 9 June 2014

Abstract
The electronic properties of graphene may be changed from semimetallic to semiconducting by introducing perforations (antidots) in a periodic pattern. The properties of such graphene antidot lattices (GALs) have previously been studied using atomistic models, which are very time consuming for large structures. We present a continuum model that uses the Dirac equation (DE) to describe the electronic and optical properties of GALs. The advantages of the Dirac model are that the calculation time does not depend on the size of the structures and that the results are scalable. In addition, an approximation of the band gap using the DE is presented. The Dirac model is compared with nearest-neighbour tight-binding (TB) in order to assess its accuracy. Extended zigzag regions give rise to localized edge states, whereas armchair edges do not. We find that the Dirac model is in quantitative agreement with TB for GALs without edge states, but deviates for antidots with large zigzag regions.

Keywords: graphene, antidot lattice, band gap, Dirac equation

(Some figures may appear in colour only in the online journal)

1. Introduction

Graphene has been the subject of intense research since it was discovered a decade ago [1]. This novel two-dimensional material has remarkable electronic [2, 3], optical [4] and mechanical [5] properties. Consequently, it finds potential applications within e.g. electronics and optoelectronics [6]. The excellent electronic properties of graphene, especially its very high mobility, make it ideally suited for new smaller and faster nanoelectronic devices [1–3]. Due to its semi-metallic nature, pristine graphene is not well-suited for semiconductor applications. Several strategies for introducing a band gap have been proposed, including graphene nanoribbons (GNRs) [7–9], gated bilayer graphene [10] and periodic gating [11]. Alternatively, an energy gap may be created using graphene quantum dots, or graphene nanodisks, which also show promising results as hosts for spin qubits [12–15]. Another method is to introduce perforations in a periodic pattern, called a graphene antidot lattice (GAL) [16, 17]. This provides a controllable band gap that depends on the geometry of the antidot lattice [16]. Previously, tight-binding (TB) calculations have been made for relatively small unit cells [16–18]. Trolle *et al* [19] have used density functional theory (DFT) and Hubbard TB to show that localized edge states emerge in GALs containing hexagonal antidots with zigzag edges. However, realistic structures are typically much larger than the ones studied theoretically, and the calculation time scales badly with the size of the structures. Fürst *et al* [18] have previously presented an analysis based on the Dirac equation (DE), in which they used finite-element analysis to calculate the electronic properties of GALs with circular antidots. The computational time of their method depends only on the ratio between the radius of the antidot and the size of the unit cell, but their method only qualitatively predicts the band structure.

Recently, GALs with circular antidots have been fabricated by several groups [20–23]. Such structures are fabricated either by e-beam lithography [20, 21] or using diblock copolymer templates [22, 23]. Moreover, Oberhuber *et al* [24] have fabricated

GALs with hexagonal antidots. They used an etching technique that selectively etches armchair edges, which produces hexagonal antidots with zigzag edges. Xu *et al* [25] have demonstrated that it is possible to create antidots with diameters down to 2 nm using a scanning transmission electron microscope. When subsequently heating the sample, the curved edges of the antidots were observed to reconstruct into armchair edges. It has also been shown that Joule heating reconstructs graphene edges into zigzag or armchair configurations [26]. Theoretical studies based on DFT show that the preferred edge chirality of GNRs is armchair in an oxygen-rich atmosphere and zigzag for water-saturated GNRs [27]. Although there may still remain some edge roughness, these findings show that the chirality of the edges of GNRs and GALs is controllable.

In this paper, we present a continuum model of GALs based on the DE. In this method, the antidot lattice is modelled by a spatially varying mass term that is only nonzero inside the antidots. This makes the antidot regions increasingly unfavourable for electrons as the mass term increases. The major advantage of the Dirac model is that the calculation time does not depend on the size of the structure that is being studied. In fact, for energies much smaller than the mass term, the results are scalable. This means that, for example, a given band structure can be used to describe a geometry where all lengths are scaled by some factor if the energies are divided by the same factor. The Dirac model is compared with nearest-neighbour TB in order to assess its accuracy. The two models will mainly be compared for GALs containing hexagonal antidots with zigzag or armchair edges. Furthermore, the DE is used to derive an approximation of the band gap of GALs, which is compared with TB for a wide range of structures. We demonstrate that the Dirac model is in quantitative agreement with TB for GALs containing antidots with armchair edges. However, for other antidot geometries, the models only agree for small antidots. We use TB to calculate the band gap of a large range of geometries, and obtain gaps ranging between practically zero and 2.25 eV. However, experimentally feasible structures result in a band gap on the order of 100 meV.

2. Theory and methods

In the present work, we will model GALs using the DE and compare the results with nearest-neighbour TB. We use the notation GAL to describe structures where the antidot lattice vectors are parallel to the carbon–carbon bonds. By rotating the lattice $\pi/6$, the antidot lattice vectors are perpendicular to the carbon–carbon bonds. These structures will be denoted rotated GALs (RGALs) as in [28]. We will focus on GALs containing hexagonal antidots with zigzag and armchair edges, which we will refer to as zigzag and armchair antidots throughout the paper. Figure 1 shows examples of GALs with zigzag and armchair antidots used in TB and the Dirac model. GALs with circular antidots and RGALs with armchair antidots will also be considered. The structures are described by the side length L of the unit cell and the side length S of the antidot, where all distances are in units of the graphene lattice constant a. Circular antidots are correspondingly

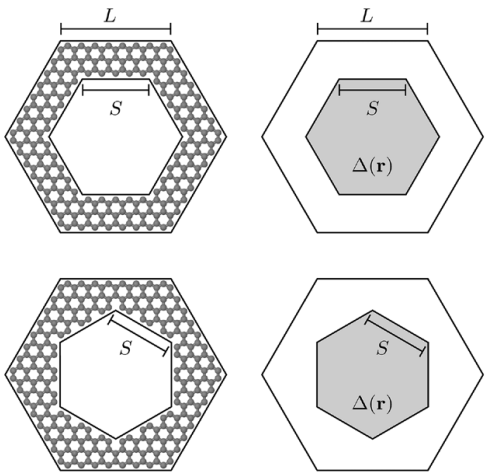

Figure 1. Unit cells used in TB (left) and DE (right) for hexagonal antidots with zigzag (top) and armchair (bottom) edges in triangular antidot lattices. The atomic structures shown are Z{8, 5}GAL and A{8, 5}GAL.

characterized by the radius R. The unit cells for TB are generated by removing all atoms within the antidot region and subsequently removing dangling bonds. The notations Z{L, S}GAL and A{L, S}GAL will be used to describe the geometry of GALs with zigzag and armchair antidots, respectively. Furthermore, the notations C{L, R}GAL and A{L, S}RGAL will describe GALs with circular antidots and RGALs with armchair antidots, respectively.

The Dirac Hamiltonian for a graphene lattice with a spatially varying mass term $\Delta(\mathbf{r})$ has the form [18]

$$\mathbf{H} = \begin{pmatrix} \Delta(\mathbf{r}) & -\hbar v_{\mathrm{F}}\left(\mathrm{i}\partial_x - \partial_y\right) \\ -\hbar v_{\mathrm{F}}\left(\mathrm{i}\partial_x + \partial_y\right) & -\Delta(\mathbf{r}) \end{pmatrix}, \tag{1}$$

where the mass term has a constant value of Δ_0 inside the antidot and is vanishing elsewhere. The wave function Ψ will satisfy the Bloch condition if $\Psi(\mathbf{r}) = \mathrm{e}^{\mathrm{i}\mathbf{k}\cdot\mathbf{r}}u(\mathbf{r})$, where the function $u(\mathbf{r})$ is a lattice-periodic spinor containing the components $u^A(\mathbf{r})$ and $u^B(\mathbf{r})$. We then express $\Delta(\mathbf{r})$ and $u(\mathbf{r})$ as Fourier series, as they are both periodic with the antidot lattice

$$\Delta(\mathbf{r}) = \sum_{\mathbf{G}} \Delta_{\mathbf{G}} e^{\mathrm{i}\mathbf{G}.\mathbf{r}}, \quad u(\mathbf{r}) = \sum_{\mathbf{G}} u_{\mathbf{G}} \mathrm{e}^{\mathrm{i}\mathbf{G}.\mathbf{r}}, \tag{2}$$

where $u_{\mathbf{G}}$ is a spinor containing the Fourier coefficients $u_{\mathbf{G}}^A$ and $u_{\mathbf{G}}^B$, $\mathbf{G} = p\mathbf{g}_1 + q\mathbf{g}_2$ is the reciprocal lattice vector, p and q are integers, and $\mathbf{g}_1$ and $\mathbf{g}_2$ are the primitive reciprocal lattice vectors of the antidot lattice. The geometry of the antidot is then solely described by the Fourier coefficients $\Delta_{\mathbf{G}}$ and the geometry of the unit cell is solely described by $\mathbf{g}_1$ and $\mathbf{g}_2$. The expression for $\Delta_{\mathbf{G}}$ for an arbitrary N-sided polygon was derived in [29]. Inserting the expressions for $\Delta(\mathbf{r})$ and $\Psi(\mathbf{r})$ in the Dirac equation $\mathbf{H}\Psi = E\Psi$ leads to the expression

$$\sum_{\mathbf{G}'} \mathbf{H}_{\mathbf{G},\mathbf{G}'} u_{\mathbf{G}'} = E u_{\mathbf{G}}, \tag{3}$$

$$\mathbf{H}_{\mathbf{G},\mathbf{G}'} = \begin{pmatrix} \Delta_{\mathbf{G}-\mathbf{G}'} & T_{\mathbf{G}}\delta_{\mathbf{G},\mathbf{G}'} \\ T^{*}_{\mathbf{G}}\delta_{\mathbf{G},\mathbf{G}'} & -\Delta_{\mathbf{G}-\mathbf{G}'} \end{pmatrix}, \tag{4}$$

where $T_{\mathbf{G}} = \hbar v_{\mathrm{F}}[k_x + G_x - \mathrm{i}(k_y + G_y)]$. This may be set up as a matrix equation and solved as an eigenvalue problem through numerical diagonalization. Electrons are excluded more and more from the antidot region as the mass term increases, and in the limit of an infinite mass term, the electrons are completely excluded. Therefore, convergence is obtained by using a sufficiently large mass term. However, convergence must also be ensured by choosing a basis that is large enough. Throughout the paper we use a mass term given by $\Delta_0 = 170$ eV L^{-1}. The reciprocal lattice vectors used for the basis are created by letting $p, q \in [-N, N]$, where we use $N = 20$ and $N = 16$ for hexagonal and circular antidots, respectively. These parameters were found to provide adequately converged results.

Our method is different from the one used by Fürst *et al* [18], who studied GALs with circular antidots using the DE. They used the commercially available finite-element solver COMSOL Multiphysics for their calculations. They studied the case of an infinite mass term by imposing the boundary condition that the current normal to the edge of the antidot is vanishing. This method was shown to provide results that agree qualitatively, but not quantitatively, with TB. Their boundary condition states that $\Psi_A(\mathbf{r}) = \mathrm{i}\mathrm{e}^{-\mathrm{i}\phi}\Psi_B(\mathbf{r})$, where $\Psi_{A/B}(\mathbf{r})$ are the two spinor components of the wave function and ϕ is the polar angle of the normal vector at a given point on the edge of the antidot. This was shown to be problematic in the limit of vanishing antidots where the angle ϕ becomes completely undetermined. In this case, the band gap was non-vanishing and approached a value of approximately $1.02\gamma/L$, where γ is the transfer integral of nearest-neighbour TB. Our method uses a finite mass term. However, in the limit of an infinite mass term, the two approaches should be equivalent, and in this case our method should also show a finite band gap in the limit of vanishing antidots. In practice, we cannot use an infinite mass term, as this would require an infinite basis. Because our model uses a finite mass term, we do not encounter the same problem in the limit of vanishing antidots.

We have focused our attention on hexagonal antidots, although other geometries may easily be considered by adjusting the Fourier coefficients of the mass term accordingly. An approximation of the band gap of a GAL is derived in appendix A from the DE by assuming cylindrical symmetry in the unit cell.

The atomistic model used for comparison is nearest-neighbour TB in the orthogonal approximation (assuming no overlap between atomic wave functions) with a transfer integral of $\gamma = 3.033$ eV.

3. Results

In this section, we present the results of our Dirac model and compare them with TB. Only positive energies of band structures will be shown, as the valence bands follow from exact electron-hole symmetry. We will present results for GALs with zigzag and armchair antidots, as well as GALs with circular antidots and RGALs with armchair antidots.

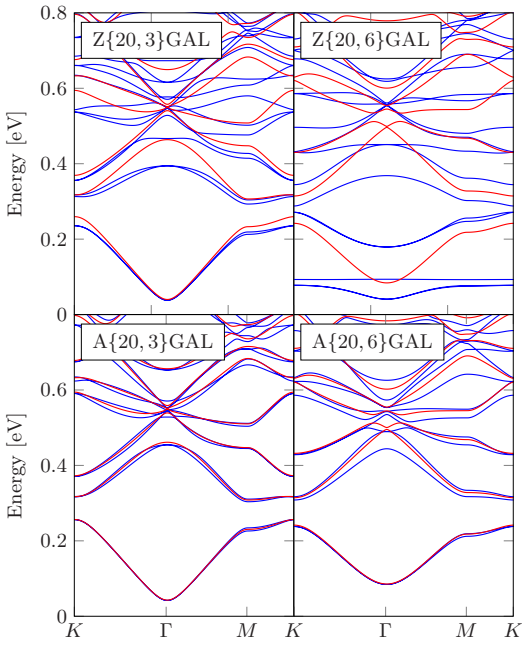

Figure 2. Comparison of DE (red) and TB (blue) band structures for GALs with zigzag and armchair antidots.

Band structures calculated using the DE and TB are compared in figure 2 for four different geometries. The geometries used for the Dirac model are created such that the area of the antidot equals the total area of the removed atoms. For all four geometries shown, a band gap opens up at the Γ-point both for the DE and TB calculations. In the case of zigzag antidots, the Dirac model agrees well with the band structure from TB when the antidot is very small, e.g. for the Z{20, 3}GAL geometry. However, large discrepancies are observed for the Z{20, 6}GAL geometry. The band structures agree much better for armchair antidots. For the A{20, 3}GAL geometry, the DE band structure almost coincides with the TB band structure, and the two models are in excellent agreement in this case. Even the band structures for the A{20, 6}GAL with a larger antidot agree very well. This tendency continues for larger antidots, where the band structures from the two models remain very similar.

The lowest bands of the Z{20, 6}GAL geometry are very flat, especially the third conduction band near 0.09 eV, which is almost completely dispersionless. For larger zigzag antidots, even more bands become dispersionless, and the band structures agree even worse. Dispersionless bands are associated with localized states. The localization of the electrons may be visualized by plotting the electron probability density on each atom in the unit cell. Figure 3 shows the probability density of the third conduction band for the Z{20, 6}GAL and A{20, 6}GAL geometries within one unit cell. The plots are

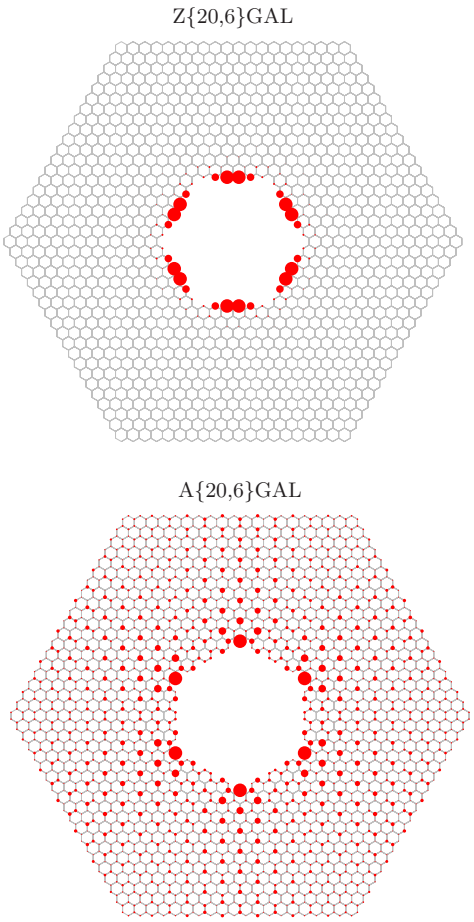

Figure 3. Electron probability density of the third conduction band in one unit cell. The radius of each circle is proportional to the absolute square of the eigenvector element for that atom and chosen such that the radius of the largest circle is the same in both plots.

generated by averaging over the Brillouin zone. It is clear that the electrons of the Z{20, 6}GAL are confined to the edge of the antidot, whereas the electrons in the A{20, 6}GAL are generally spread out over the entire unit cell and only slightly localized in the corners of the antidot. Such localized edge states are generally observed when the antidot contains long zigzag regions. The existence of localized edge states was studied by Fujita *et al* [30], who showed that edge states appear for semi-infinite graphene with zigzag termination, whereas armchair termination does not lead to edge states. Brey and Fertig [31] have used the DE to study the electronic states of GNRs, and by using appropriate boundary conditions, they arrived at the same conclusion. Localized edge states in GALs have previously been studied by Vanević *et al* [32]. They showed that triangular antidots with zigzag edges lead to dispersionless bands where the electrons are localized at the edge of the antidot, which is in good agreement with our results. Recently, Trolle *et al* [19] used DFT and Hubbard TB to investigate localized edge states in GALs with zigzag antidots. Furthermore, they showed that the edge states become spin polarized when $S \geqslant 6$. Edge states have also been observed experimentally using scanning tunnelling spectroscopy on GNRs fabricated by 'unzipping' carbon nanotubes [33]. Edge states modify the electronic properties of GNRs and figure 2 shows that they also modify the electronic properties of GALs. As the size of the antidot increases, edge states appear for zigzag antidots and the electrons become more and more confined to the edges of the antidot. The Dirac model is a continuum model, and consequently all atomistic features are missing. With no boundary conditions, the Dirac model is unable to predict the localized edge states appearing for zigzag edges.

The size of the band gap is highly dependent on the lattice geometry. Generally, the band gap increases as the ratio of antidot to unit-cell area (fill factor) increases. A linear scaling law for GALs with circular antidots was proposed by Pedersen *et al* [16] suggesting that the band gap scales as $E_g \approx K \cdot N_{\text{removed}}^{1/2} / N_{\text{total}}$ for small values of $N_{\text{removed}}^{1/2} / N_{\text{total}}$, where N_{removed} is the number of removed atoms and N_{total} is the total number of atoms in the unit cell before the antidot was created. They determined the scaling constant as $K \simeq 25$ eV, whereas a more exact quasiparticle TB model has revealed a slightly larger constant of $K \simeq 29$ eV [34]. The DE band structures in figure 2 show that the band gap increases as the size of the antidot increases, which is expected from the scaling law. The size of the band gap may be estimated by replacing the hexagonal unit cell with an approximated unit cell with full cylindrical symmetry and by assuming an infinite mass term. This means that both the unit cell and the antidot are replaced by circles of equivalent areas, see appendix A for a derivation. The band gap then only depends on the total area of the unit cell A_{total} and the area of the antidot A_{removed}. The approximation of the band gap (given by equation (A.6)) may be used to calculate the band gap scaled by $A_{\text{total}}^{1/2}$ as a function of $A_{\text{removed}}^{1/2} / A_{\text{total}}^{1/2}$, which becomes the universal curve shown in figure 4. The scaling law predicts a linear correlation on these axes, and a linear approximation of equation (A.6) (given by equation (A.8)) is also shown in the figure. The scaling constant for the DE, obtained from equation (A.8), is $K = 4 \cdot 3^{1/4} \sqrt{\pi} \gamma \simeq 28.3$ eV, which is very close to the scaling constants determined from atomistic models.

Band gap energies of a wide range of structures have been calculated using TB and are compared with the results of the Dirac model in figure 4. The approximation of the band gap using the DE is also included in the figure. The values of A_{total} and A_{removed} in TB are calculated directly from N_{total} and N_{removed}, respectively. The approximated band gap is seen to be a very good estimate as it is very close to the curve obtained from the numerical diagonalization method. Furthermore, the Dirac model predicts that the band gap increases linearly in the regime $A_{\text{removed}}^{1/2} / A_{\text{total}}^{1/2} < 0.4$. For GALs with zigzag antidots, the TB results are close to the results from the Dirac model when the antidots are fairly small. However, edge states appear for larger antidots, which cause the band gap to shrink. Furthermore, the band gaps from TB for zigzag antidots are

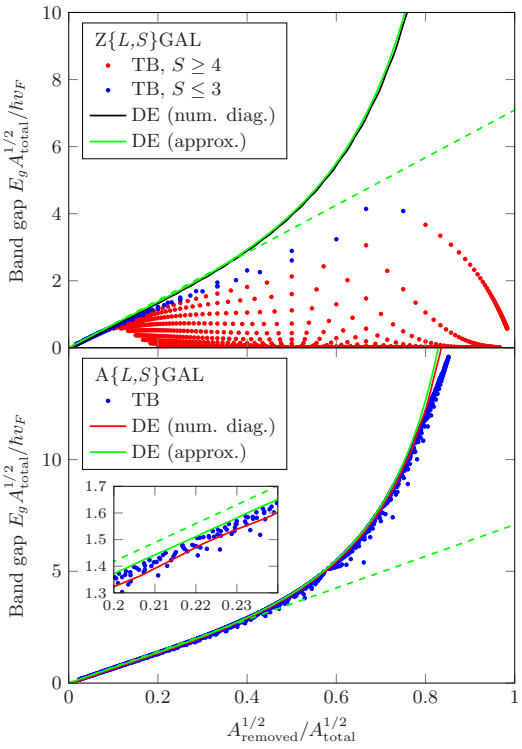

Figure 4. Band gap of GALs with zigzag and armchair antidots calculated using TB and the DE. The green dashed line is a linearization of the approximated Dirac curve. The inset shows a zoom of the linear region.

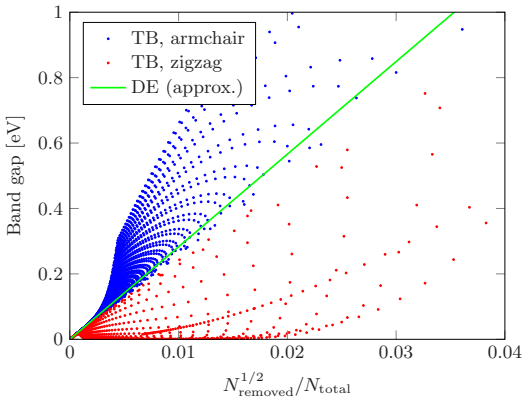

Figure 5. Comparison of the band gap in units of eV for the same data as shown in figure 4.

always lower than the linear Dirac result. For the A{*L*, *S*} GAL structures, the band gaps calculated from TB are all very close to the curves from the DE. Moderate deviations are only observed in the region $A_{\text{removed}}^{1/2}/A_{\text{total}}^{1/2} > 0.8$. The absence of localized edge states in the case of armchair edges means that the band gap does not vanish for large antidots. The inset in the figure shows a zoom, where it is seen that the approximation of the band gap from the DE serves as an upper limit for the TB band gap calculations. The band gap obtained from the numerical diagonalization method shows lower values than the approximated version. This is partly because the numerical diagonalization uses a finite mass term, and partly because the approximated band gap is calculated using an approximate geometry (assumes cylindrical symmetry). Clearly, the results of figure 4 show that the DE is able to accurately predict the band gap of GALs with armchair antidots.

The band gaps in figure 4 are scaled by the area of the unit cell. To provide values of achievable gaps in absolute units, we convert the gaps of armchair and zigzag GALs in figure 4 to eV and compare them in figure 5. It is expected that the band gap of armchair GALs is generally larger than that of zigzag GALs. Figure 5 shows that this is true for all values of $N_{\text{removed}}^{1/2}/N_{\text{total}}$, and it is seen that the approximate band gap from the DE is close to being a separation line between the band gaps of the two types of GALs. At present, state of the art fabrication, using diblock copolymer templates, has resulted in GALs with circular antidots arranged in a triangular pattern with a diameter of 18.7 nm and a period of 36.4 nm [22]. Using these parameters, our Dirac model predicts a band gap of 66 meV, which is close to the measured effective transport gap of 102 meV. This level of discrepancy is reasonable bearing in mind that the transport gap of a disordered structure is expected to deviate somewhat from the band gap of a perfectly periodic model.

The approximation of the band gap using the DE seems to be the better choice, as it is computationally much faster than numerical diagonalization. However, the numerical diagonalization method is necessary in order to calculate band structures and may also be used to calculate other properties such as the density of states and optical conductivity. A comparison of the optical conductivity calculated using the DE and TB is shown in figure 6 for four GALs. The method for calculating the optical conductivity was adopted from [17]. We reach the same conclusion as for the band structures in figure 2. The optical conductivity from the Dirac model agrees very well with the TB results for armchair antidots. For zigzag antidots, the results agree for low energies when the antidot is small, but the optical spectra are very different for larger antidots, e.g. the Z{20, 6}GAL. The optical properties of gapped graphene, i.e. using a spatially invariant mass term, have previously been presented in a closed-form expression and compared with TB [35]. The conductivity spectra $\sigma(\omega)$ were shown to always increase abruptly at the band gap energy to $\sigma(\omega_g) = 2\sigma_0$, where $\sigma_0 = e^2/4\hbar$ is the conductivity of pristine graphene. Gapped graphene was shown to be a good approximation at energies near the band gap for a GAL with a small circular antidot. The spectra from our Dirac model follow the spectra from TB very well in the case of armchair antidots, and even capture features at energies far from the band gap.

Until now, we have only considered GALs with hexagonal antidots, but other geometries may easily be compared with the Dirac model. Figure 7 shows a comparison of the band gap calculated using the DE and TB for GALs with circular

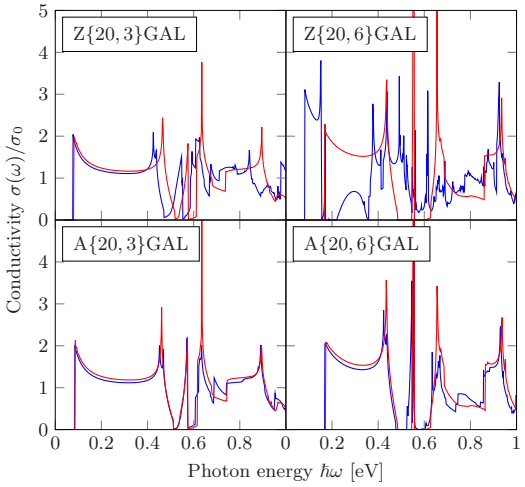

Figure 6. Optical conductivity in units of the pristine graphene conductivity $\sigma_0 = e^2/4\hbar$ calculated using the DE (red) and TB (blue) for the GALs shown in figure 2.

antidots and RGALs with armchair antidots. The edge of circular antidots will consist of both zigzag and armchair edges when the antidot is not very small. The zigzag parts of the edge will support localized edge states when the antidot is large, which cause the band gap to shrink as observed in the figure. However, for small antidots ($R \leqslant 5$), the Dirac model predicts the band gap reasonably well, as the localization is weak.

The band gap calculations of A{*L*, *S*}RGAL structures show the same tendency as the A{*L*, *S*}GAL structures in figure 4. RGALs were found to provide a band gap only for every third value of *L*. This is consistent with previous findings [28], and also obeys a universal band gap opening rule by Dvorak *et al* [36]. The Dirac model predicts that the band gap increases dramatically for $A^{1/2}_{\text{removed}}/A^{1/2}_{\text{total}} > 0.8$. TB shows somewhat lower values of the band gap in this region, but these also increase dramatically as for the Dirac model. Again, the inset shows that the approximation of the band gap from the DE seems to be the upper limit of TB.

It should be noted that while all structures considered in this paper are perfectly ordered, realistic structures from experiments will to some extent contain disorder. Theoretical studies have shown that the band gap of GALs is robust against a considerable amount of disorder [37]. The band gap was found to initially shrink and eventually vanish as the amount of disorder increased. Other calculations have shown that the properties of graphene waveguide structures based on GALs are also robust against structural disorder [38].

We have shown that the Dirac model is in good agreement with TB in the absence of edge states. However, in the case of zigzag or circular antidots, edge states cause the band gap to shrink. If the electrons of edge states are completely confined to the edges of the antidot, they will not be able to contribute to the electronic transport of the GAL. The lowest conduction bands of GALs with large zigzag antidots are almost

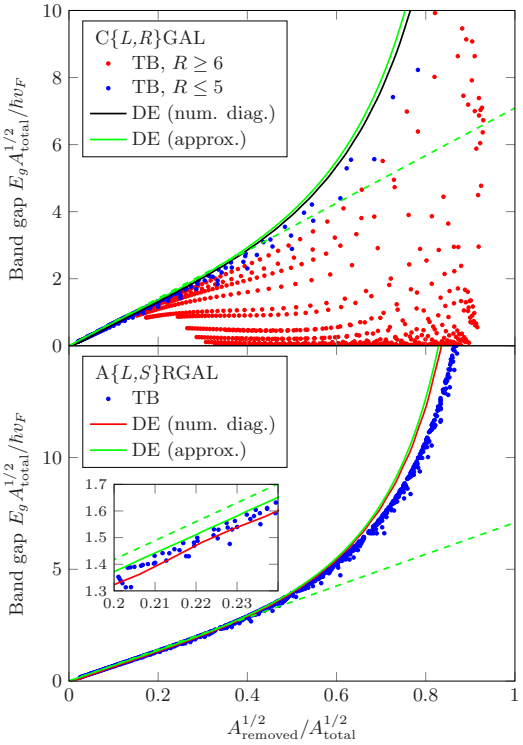

Figure 7. Same as figure 4, but for GALs with circular antidots and RGALs with armchair antidots.

completely dispersionless, which suggests that the transport gap in such cases may be larger than the band gap.

4. Conclusion

We have presented a continuum model based on the Dirac equation, which describes the electronic and optical properties of graphene antidot lattices. The major advantages of the Dirac model are that the computational time does not depend on the size or geometry of the structures, and that the results are scalable. The Dirac model is compared with tight-binding calculations of the corresponding atomistic structures in order to determine its accuracy. A comparison of band structures shows that the Dirac model is in quantitative agreement with tight-binding for structures with no edge states, e.g. antidots with armchair edges. The present Dirac model is unable to predict edge states as it does not distinguish between zigzag and armchair edges. Comparing band gap calculations and optical spectra also shows quantitative agreement between the models for structures with no edge states.

An approximation of the band gap of a graphene antidot lattice was derived from the Dirac equation. A linearization revealed a scaling constant in good agreement with previously suggested values obtained from atomistic models. The approximation provides a very fast way of estimating the band

gap of a graphene antidot lattice with no edge states even if the antidot makes up a large part of the unit cell.

Acknowledgments

The authors gratefully acknowledge the financial support from the Center for Nanostructured Graphene (project no. DNRF58) financed by the Danish National Research Foundation. We thank A-P Jauho for useful comments on the manuscript.

Appendix A. Estimate of band gap

In this appendix, we present an approximation of the band gap of GALs derived using the DE. The hexagonal unit cell is replaced by one with full cylindrical symmetry, i.e. a circle of radius R_e, see figure A1. This approach is inspired by [39]. The area of the circle is equal to the area of the hexagonal unit cell, such that $A_{\text{total}} = \pi R_e^2$. If the antidot is not circular, this is also replaced by a circle with radius R of equivalent antidot area, $A_{\text{removed}} = \pi R^2$.

The Dirac Hamiltonian in cylindrical coordinates is

$$\mathbf{H} = \hbar v_{\text{F}} \begin{pmatrix} \widetilde{\Delta}(r) & -\mathrm{i}\mathrm{e}^{-\mathrm{i}\theta}\left(\partial_r - \frac{\mathrm{i}}{r}\partial_\theta\right) \\ -\mathrm{i}\mathrm{e}^{\mathrm{i}\theta}\left(\partial_r + \frac{\mathrm{i}}{r}\partial_\theta\right) & -\widetilde{\Delta}(r) \end{pmatrix}, \quad \text{(A.1)}$$

where $\widetilde{\Delta}(r) = \frac{\Delta_0}{\hbar v_{\text{F}}} H(R-r) = \widetilde{\Delta}_0 H(R-r)$ and H is the Heaviside step function. The wave function is of the form

$$\Psi(r,\theta) = \frac{1}{\sqrt{2}} \begin{pmatrix} \mathrm{i}^m f(r)\,\mathrm{e}^{\mathrm{i}m\theta} \\ \mathrm{i}^{m+1} g(r)\,\mathrm{e}^{\mathrm{i}(m+1)\theta} \end{pmatrix}, \quad \text{(A.2)}$$

which is inserted in the DE together with the Hamiltonian. For a piecewise constant mass term, the solutions for f and g are

$$f(r) = \begin{cases} J_m(kr) + B_m Y_m(kr) & r > R \\ C_m I_m(qr) & r < R \end{cases}, \quad \text{(A.3)}$$

$$g(r) = \begin{cases} J_{m+1}(kr) + B_m Y_{m+1}(kr) & r > R \\ -C_m \sqrt{\dfrac{\widetilde{\Delta}_0 - k}{\widetilde{\Delta}_0 + k}}\, I_{m+1}(qr) & r < R \end{cases}, \quad \text{(A.4)}$$

where J_m and Y_m are the m'th order Bessel functions of the first and second kind, respectively, I_m is the m'th order modified Bessel function of the first kind, $k = E/\hbar\, v_{\text{F}}$ and $q = (\widetilde{\Delta}_0^2 - k^2)^{1/2}$. Both f and g must be continuous at $r = R$, which is used to determine B_m and C_m. For the lowest state ($m = 0$) and in the limit of large $\widetilde{\Delta}_0$, the coefficients become

$$B_0 \approx -\frac{J_0(kR) + J_1(kR)}{Y_0(kR) + Y_1(kR)}, \qquad C_0 \approx 0. \quad \text{(A.5)}$$

This derivation is generally carried out using a finite mass term, and the band gap may also be calculated in this case. The wave functions inside and outside the antidot are matched at the edge of the antidot in the case of a finite mass term, which is used to determine B_m and C_m. Subsequently the limit of a large mass term is applied for which the coefficients listed above are valid. This approach does not lead to boundary conditions that cause problems in the limit of small antidots as observed in [18].

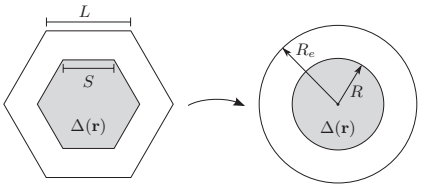

Figure A1. The hexagonal unit cell and the antidot are replaced by circles of equivalent areas. This approximated geometry has cylindrical symmetry.

We restrict our analysis to the Γ-point of the Brillouin zone, as this is where the band gap opens. We still require that the wave function is Bloch-periodic when using the approximated geometry. However, at the Γ-point it is merely periodic. Periodicity implies a vanishing derivative of f at the outer boundary ($r = R_e$), meaning that $J_1(kR_e) + B_0 Y_1(kR_e) = 0$. This yields the equation

$$J_1(kR_e)\,[\,Y_0(kR) + Y_1(kR)\,] - Y_1(kR_e)\,[\,J_0(kR) + J_1(kR)\,] = 0, \quad \text{(A.6)}$$

which may be solved numerically for k to obtain the band gap given by $E_g = 2\hbar v_{\text{F}} k$. f is used to solve for the lowest energy of the conduction bands. Equivalently, g may be solved for negative energies using $m = -1$ which leads to the highest energy of the valence bands. The Bessel functions in equation (A.6) are approximated by assuming small k, such that the equation becomes

$$\frac{4}{kR_e} + kR_e - \frac{2R_e}{R} + \frac{2R}{R_e} + kR_e(2 + kR)\ln\left(\frac{R}{R_e}\right) = 0. \quad \text{(A.7)}$$

In the limit of small R, the solution becomes the simple expression $k \approx 2R/R_e^2$, meaning that

$$E_g = 4\hbar v_{\text{F}} \frac{R}{R_e^2} = 4\sqrt{\pi}\,\hbar v_{\text{F}} \frac{A_{\text{removed}}^{1/2}}{A_{\text{total}}}. \quad \text{(A.8)}$$

This shows that at small k, the band gap is directly proportional to the square root of the removed area and inversely proportional to the area of the unit cell, which is consistent with previously suggested scaling laws [16, 34].

References

[1] Novoselov K S, Geim A K, Morozov S V, Jiang D, Zhang Y, Dubonos S V, Grigorieva I V and Firsov A A 2004 *Science* **306** 666

[2] Novoselov K S, Jiang D, Schedin F, Booth T J, Khotkevich V V, Morozov S V and Geim A K 2005 *Proc. Natl Acad. Sci. USA* **102** 10451

[3] Bolotin K I, Sikes K, Jiang Z, Klima M, Fudenberg G, Hone J, Kim P and Stormer H 2008 *Solid State Commun.* **146** 351

[4] Nair R R, Blake P, Grigorenko A N, Novoselov K S, Booth T J, Stauber T, Peres N M R and Geim A K 2008 *Science* **320** 1308
[5] Lee C, Wei X, Kysar J W and Hone J 2008 *Science* **321** 385
[6] Geim A K 2009 *Science* **324** 1530
[7] Obradovic B, Kotlyar R, Heinz F, Matagne P, Rakshit T, Giles M, Stettler M and Nikonov D 2006 *Appl. Phys. Lett.* **88** 142102
[8] Son Y W, Cohen M L and Louie S G 2006 *Phys. Rev. Lett.* **97** 216803
[9] Han M Y, Özyilmaz B, Zhang Y and Kim P 2007 *Phys. Rev. Lett.* **98** 206805
[10] Zhang Y, Tang T T, Girit C, Hao Z, Martin M C, Zettl A, Crommie M F, Shen Y R and Wang F 2009 *Nature* **459** 820
[11] Pedersen J G and Pedersen T G 2012 *Phys. Rev.* B **85** 235432
[12] Recher P and Trauzettel B 2010 *Nanotechnology* **21** 302001
[13] Molitor F, Güttinger J, Stampfer C, Dröscher S, Jacobsen A, Ihn T and Ensslin K 2011 *J. Phys.: Condens. Matter* **23** 243201
[14] Güttinger J, Molitor F, Stampfer C, Schnez S, Jacobsen A, Dröscher S, Ihn T and Ensslin K 2012 *Rep. Prog. Phys.* **75** 126502
[15] Kandemir B S and Omer G 2013 *Eur. Phys. J.* B **86** 299
[16] Pedersen T G, Flindt C, Pedersen J G, Mortensen N A, Jauho A P and Pedersen K 2008 *Phys. Rev. Lett.* **100** 136804
[17] Pedersen T G, Flindt C, Pedersen J, Jauho A P, Mortensen N A and Pedersen K 2008 *Phys. Rev.* B **77** 245431
[18] Fürst J A, Pedersen J G, Flindt C, Mortensen N A, Brandbyge M, Pedersen T G and Jauho A P 2009 *New J. Phys.* **11** 095020
[19] Trolle M L, Møller U S and Pedersen T G 2013 *Phys. Rev.* B **88** 195418
[20] Eroms J and Weiss D 2009 *New J. Phys.* **11** 095021
[21] Giesbers A J M, Peters E C, Burghard M and Kern K 2012 *Phys. Rev.* B **86** 045445
[22] Kim M, Safron N S, Han E, Arnold M S and Gopalan P 2010 *Nano Lett.* **10** 1125
[23] Kim M, Safron N S, Han E, Arnold M S and Gopalan P 2012 *ACS Nano* **6** 9846
[24] Oberhuber F, Blien S, Heydrich S, Yaghobian F, Korn T, Schüller C, Strunk C, Weiss D and Eroms J 2013 *Appl. Phys. Lett.* **103** 3111
[25] Xu Q, Wu M Y, Schneider G F, Houben L, Malladi S K, Dekker C, Yucelen E, Dunin-Borkowski R E and Zandbergen H W 2013 *ACS Nano* **7** 1566
[26] Jia X *et al* 2009 *Science* **323** 1701
[27] Seitsonen A P, Saitta A M, Wassmann T, Lazzeri M and Mauri F 2010 *Phys. Rev.* B **82** 115425
[28] Petersen R, Pedersen T G and Jauho A P 2010 *ACS Nano* **5** 523
[29] Lee S W and Mittra R 1983 *IEEE Trans. Antennas Propag.* **31** 99
[30] Fujita M, Wakabayashi K, Nakada K and Kusakabe K 1996 *J. Phys. Soc. Japan* **65** 1920
[31] Brey L and Fertig H 2006 *Phys. Rev.* B **73** 235411
[32] Vanević M, Stojanović V M and Kindermann M 2009 *Phys. Rev.* B **80** 045410
[33] Tao C *et al* 2011 *Nat. Phys.* **7** 616
[34] Petersen R and Pedersen T G 2009 *Phys. Rev.* B **80** 113404
[35] Pedersen T G, Jauho A P and Pedersen K 2009 *Phys. Rev.* B **79** 113406
[36] Dvorak M, Oswald W and Wu Z 2013 *Sci. Rep.* **3** 02289
[37] Yuan S, Roldán R, Jauho A P and Katsnelson M I 2013 *Phys. Rev.* B **87** 085430
[38] Pedersen J G, Gunst T, Markussen T and Pedersen T G 2012 *Phys. Rev.* B **86** 245410
[39] Mortensen N A 2006 *J. Eur. Opt. Soc.—Rapid* **1** 06009

Paper II

Dirac model of electronic transport in graphene antidot barriers

Morten Rishøj Thomsen, Søren Jacob Brun and Thomas Garm Pedersen

The paper has been published in
Journal of Physics: Condensed matter **26**, 335301 (2014)

IOP Publishing Journal of Physics: Condensed Matter
J. Phys.: Condens. Matter **26** (2014) 335301 (8pp) doi:10.1088/0953-8984/26/33/335301

Dirac model of electronic transport in graphene antidot barriers

M R Thomsen, S J Brun and T G Pedersen

Department of Physics and Nanotechnology, Aalborg University, Skjernvej 4A, DK-9220 Aalborg Øst, Denmark
Center for Nanostructured Graphene (CNG), DK-9220 Aalborg Øst, Denmark

E-mail: mrt@nano.aau.dk

Received 30 April 2014, revised 26 June 2014
Accepted for publication 30 June 2014
Published 29 July 2014

Abstract

In order to use graphene for semiconductor applications, such as transistors with high on/off ratios, a band gap must be introduced into this otherwise semimetallic material. A promising method of achieving a band gap is by introducing nanoscale perforations (antidots) in a periodic pattern, known as a graphene antidot lattice (GAL). A graphene antidot barrier (GAB) can be made by introducing a 1D GAL strip in an otherwise pristine sheet of graphene. In this paper, we will use the Dirac equation (DE) with a spatially varying mass term to calculate the electronic transport through such structures. Our approach is much more general than previous attempts to use the Dirac equation to calculate scattering of Dirac electrons on antidots. The advantage of using the DE is that the computational time is scale invariant and our method may therefore be used to calculate properties of arbitrarily large structures. We show that the results of our Dirac model are in quantitative agreement with tight-binding for hexagonal antidots with armchair edges. Furthermore, for a wide range of structures, we verify that a relatively narrow GAB, with only a few antidots in the unit cell, is sufficient to give rise to a transport gap.

Keywords: graphene, antidot, dirac equation, electronic transport

(Some figures may appear in colour only in the online journal)

1. Introduction

Graphene has been the subject of intense research since its discovery in 2004 [1]. Especially the ultrahigh mobility [2–4] of pristine graphene makes it a promising platform for novel nanoelectronic devices. Pristine graphene does not have a band gap, which makes it ill-suited for semiconductor applications, such as transistors with high on/off ratios for logic applications. Band gaps in graphene have been demonstrated experimentally in graphene nanoribbons [5], gated bilayer graphene [6, 7] and patterned adsorption of hydrogen on graphene [8]. Another promising method for creating a tunable band gap in graphene is by introducing nanoscale perforations in a periodic fashion, known as graphene antidot lattices (GALs) or graphene nanomeshes [9–11]. The magnitude of the band gap depends on the size of the antidots, size of the unit cell and on edge chirality [9, 12–15]. It has been shown that the band gap of GALs with relatively small antidots follows a simple scaling rule proposed by Pedersen *et al* [9].

Several methods have been used to produce GALs experimentally, including e-beam lithography [16–18], diblock copolymer templates [19–21], anodic aluminum oxide templates [22], nanosphere lithography [23] and nanoimprint lithography [24]. The antidots range in size between a few nanometers and several hundred nanometers, depending on the fabrication method. The antidots synthesized with these methods are often round, but it has been demonstrated experimentally that armchair and zigzag edges in GALs are stable and can be synthesized selectively [25–27]. Recent experimental studies of transport in GALs have shown on/off ratios in the range between 4 and 100 [19, 22, 24]. These values are still too low for logic applications [28], but the results are important indicators that devices based on GALs could be used to make efficient transistors. The electronic transport properties of GALs have also been studied theoretically. The transport through graphene antidot barriers (GABs), i.e. 1D periodic antidot structures in an otherwise pristine sheet of graphene, has previously been studied for small systems using

a tight-binding (TB) formalism [29, 30]. These studies showed that just a few antidots in the unit cell of the GAB is sufficient to suppress the transport within the band gap region. Suppression of transport in antidot regions has also been used to model electronic waveguides [31], where a transport channel is kept pristine, while the rest of the structure is a GAL. Their results show that GAL waveguides have higher conductance than corresponding graphene nanoribbons. Furthermore, Berreda *et al* [32] have simulated three different graphene field-effect transistors based on GALs with band gaps of about 500 meV. They showed that their simulated devices had on/off ratios as high as 7400, which is close to that of silicon based MOSFETs that have on/off ratios on the order of 10^4 to 10^7 [28].

Experimentally feasible GALs are typically too large to handle with traditional atomistic models, such as TB and DFT. However, models based on the Dirac equation (DE) are in the continuum regime and are therefore able to handle arbitrarily large structures. In this paper, we will use the Dirac equation (DE) with a spatially varying mass term to calculate the scattering of Dirac electrons in GABs that are periodic in one dimension. It has previously been shown that the DE on this form can be used to calculate the band structure of GALs [11, 12]. In addition, the DE has previously been used to calculate scattering of Dirac electrons on a single circular mass barrier [33], a single circular electrostatic barrier [34] and simple barriers of constant and finite mass [35]. The advantages of our approach are that it works for any antidot shape and for an arbitrary arrangement of antidots. Furthermore, our method can easily be extended to a 1D periodic case. Another advantage that arises from using the DE is that all results are scalable, i.e., the results are invariant when all lengths are scaled up by some factor and all energies are scaled down by the same factor. We use a Green's tensor area integral equation method (AIEM) in order to solve the DE. We will focus on the transport of a plane electron wave through GABs with two different types of hexagonal antidots, namely antidots with zigzag edges and antidots with armchair edges. We compare the results of our Dirac model with results obtained with TB.

2. Theory and methods

In this section, we will set up a Green's tensor AIEM to calculate the scattering of Dirac electrons on arbitrary graphene antidot structures, where an electron wave is incident on the structure and the resulting total wave function is calculated. Once this general method has been set up, we will specialize to scattering of Dirac electrons on GABs as shown in figure 1(*b*). The idea of using an AIEM to solve inhomogeneous differential equations is not new. In fact, it has been used extensively to solve scattering problems in optics [36, 37] and we utilize several of the same techniques to calculate scattering of electron waves in graphene.

The DE for a graphene sheet with a spatially varying mass term $\Delta(\vec{r})$ has the form [11]

$$(v_F\boldsymbol{\sigma}\cdot\vec{p}+\Delta(\vec{r})\sigma_z-\boldsymbol{I}E)\Psi=0, \tag{1}$$

$$(v_F\boldsymbol{\sigma}\cdot\vec{p}-\Delta(\vec{r})\sigma_z-\boldsymbol{I}E)\Psi'=0, \tag{2}$$

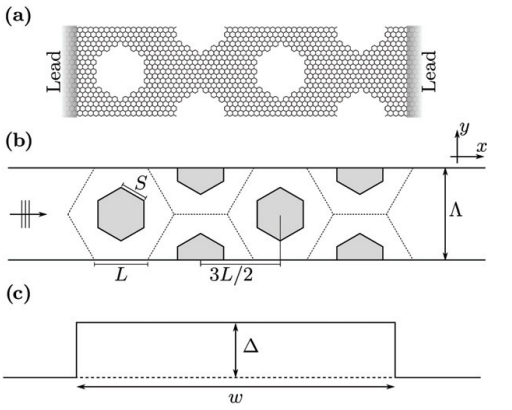

Figure 1. Unit cells of a GAB with four rows of armchair antidots. (*a*) Geometry used in TB. (*b*) Geometry used with the DE, where the mass term has a constant value of Δ_0 inside the shaded areas and is vanishing elsewhere. (*c*) Dirac mass barrier (DMB) with height Δ and width w.

where $\Psi=\{\psi_A,\psi_B\}$ and $\Psi'=\{\psi'_B,\psi'_A\}$ are the wave functions associated with the K and K' valleys, respectively, $\boldsymbol{\sigma}=\{\sigma_x,\sigma_y\}$ and σ_z are the Pauli matrices, $\boldsymbol{p}=\{\hat{p}_x,\hat{p}_y\}$ is the momentum operator, and v_F is the Fermi velocity. The mass term has a constant value of Δ_0 inside the antidots and is vanishing elsewhere. This effectively makes electrons massive inside the antidots, making it energetically unfavorable to enter them. The mass term should be sufficiently large in order to model actual holes in graphene. It should generally be much larger than the electron energy $\Delta_0\gg|E|$. We use $\Delta_0=170\,\mathrm{eV}/L$ in all our calculations, which is identical to the value used in [12]. Due to the similarity of the K and K' equations, we can restrict our analysis to one of them. The wave function of the incident wave Ψ_0 must be a solution to the case without a scatterer (pristine graphene), i.e. the case where $\Delta(\vec{r})=0$ everywhere. This simply reduces equation (1) to the DE without a mass term. We will use incident plane waves on the form $\Psi_0=2^{-1/2}(1,\mathrm{e}^{\mathrm{i}\varphi})^T\mathrm{e}^{\mathrm{i}\vec{k}\cdot\vec{r}}$, where φ is the polar angle of $\vec{k}$.

The Green's tensor $\boldsymbol{G}$ between an observation point $\vec{r}$ and a source point $\vec{r}'$ is defined as the solution to the equation

$$(v_F\boldsymbol{\sigma}\cdot\vec{p}-\boldsymbol{I}E)\boldsymbol{G}(\vec{r},\vec{r}')=-\boldsymbol{I}\delta(\vec{r}-\vec{r}'). \tag{3}$$

The solution must obey the radiation condition, which states that the solution should asymptotically tend towards an outward propagating wave proportional to $\mathrm{e}^{\mathrm{i}kr}/\sqrt{kr}$. This uniquely specifies the Green's tensor as

$$\boldsymbol{G}(\vec{r},\vec{r}')=\frac{k}{4\mathrm{i}}\begin{pmatrix}H_0^{(1)}(kr) & -\mathrm{i}\mathrm{e}^{-\mathrm{i}\theta}H_1^{(1)}(kr)\\ -\mathrm{i}\mathrm{e}^{\mathrm{i}\theta}H_1^{(1)}(kr) & H_0^{(1)}(kr)\end{pmatrix}, \tag{4}$$

where $H_n^{(1)}$ is the n'th order Hankel function of the first kind, $k=E/\hbar v_F$, $r=|\vec{r}-\vec{r}'|$ and θ is the polar angle of $\vec{r}-\vec{r}'$. By subtracting the DE without a mass term from equation (1) we get

$$(v_F\boldsymbol{\sigma}\cdot\vec{p}-\boldsymbol{I}E)(\Psi-\Psi_0)=-\Delta(\vec{r})\sigma_z\Psi, \tag{5}$$

which has the solution

$$\Psi(\vec{r}) = \Psi_0(\vec{r}) + \int \widetilde{\Delta}(\vec{r}')\sigma_z \boldsymbol{G}(\vec{r},\vec{r}')\Psi(\vec{r}')d^2r', \qquad (6)$$

where $\widetilde{\Delta}(\vec{r}) = \Delta(\vec{r})/\hbar v_F$. This is the central equation for the Green's tensor AIEM, which we will use to calculate the scattering of Dirac electrons on antidot structures. It can be demonstrated that the equation is invariant when all lengths are scaled up by some factor and all energies and mass terms are scaled down by the same factor. This effectively means that the computational time is scale invariant.

The main advantage of this approach is that we only need to consider points $\vec{r}'$ where $\Delta(\vec{r}') \neq 0$, i.e. inside the antidot. Once we know the wave function inside the antidot, it is a simple matter to use equation (6) to calculate the wave function at any other position. We solve this self-consistently by discretizing the area inside the antidots into a number of small areas δA_i with centers $\vec{r}_i$. The integral is then completed by assuming that the mass term and the wave function are constant inside each area element and by approximating the Green's tensor between element i and j as

$$\boldsymbol{G}_{ij} \simeq \begin{cases} (\delta A_j)^{-1}\int_{\delta A_j} \boldsymbol{G}(\vec{r}_i,\vec{r}')d^2r' & \text{if } i = j \\ \boldsymbol{G}(\vec{r}_i,\vec{r}_j) & \text{if } i \neq j. \end{cases} \qquad (7)$$

The self-interaction element $i = j$ may be calculated by approximating the area element with a circle, with radius r_{eq}, of equivalent area, i.e. $\delta A_j = \pi r_{\mathrm{eq}}^2$, and integrating in polar coordinates

$$\boldsymbol{G}_{ii} \simeq [1/(\pi r_{\mathrm{eq}}^2 k) - i H_1^{(1)}(kr_{\mathrm{eq}})/(2r_{\mathrm{eq}})]\boldsymbol{I}. \qquad (8)$$

We now have all the ingredients necessary to solve the scattering problem. It is then a simple matter of using matrix inversion or some efficient iterative scheme to solve for the wave function inside the antidots.

We will specialize to the case of GABs, where the antidot structure is periodic along the y-direction with period Λ as shown in figure 1(b). We will focus on hexagonal antidots arranged in a GAL configuration, meaning that the antidot lattice vectors are parallel to the carbon-carbon bonds of the graphene lattice as shown in figure 1(a). The antidots are chosen, such that they have either armchair edges (denoted armchair antidots) or zigzag edges (denoted zigzag antidots). The structures are described by the side length L of the GAL unit cell, the side length S of the antidot and the number of antidots N in the GAB unit cell, see figure 1(b). All distances are in units of the graphene lattice constant a. The notation N−A$\{L, S\}$GAL and N−Z$\{L, S\}$GAL will be used to describe barriers with N armchair and zigzag antidots, respectively, in GAL a configuration.

In the periodic case, the scattered part of the wave function is given by an infinite sum of integrals over unit cells. By shifting all integrals to the zeroth unit cell, we can take the sum inside the integral and, thus, only integrate over the area of the zeroth unit cell A_0. All shifted wave functions are related to the wave function in the zeroth unit cell by the Bloch condition $\Psi(\vec{r} + m\Lambda\hat{y}) = \Psi(\vec{r})\mathrm{e}^{\mathrm{i}mk_y\Lambda}$, where m is an integer, $\Lambda = \sqrt{3}L$ is the period, $k_y = k\sin(\varphi)$ and φ is the angle of incidence. We may then write the wave function as

$$\Psi(\vec{r}) = \Psi_0(\vec{r}) + \int_{A_0} \widetilde{\Delta}(\vec{r}')\sigma_z \widetilde{\boldsymbol{G}}(\vec{r},\vec{r}')\Psi(\vec{r}')d^2r', \qquad (9)$$

where $\widetilde{\boldsymbol{G}}$ is a modified Green's tensor given by

$$\widetilde{\boldsymbol{G}}(\vec{r},\vec{r}') = \sum_{m=-\infty}^{\infty} \boldsymbol{G}(\vec{r},\vec{r}' - m\Lambda\hat{y})e^{\mathrm{i}k_y m\Lambda}. \qquad (10)$$

This sum is extremely slowly convergent. However, once it has been determined, the problem of finding the wave function is no harder than in the non-periodic case. Using Graf's theorem [38] the Green's tensor may be restated as

$$\widetilde{\boldsymbol{G}}(\vec{r},\vec{r}') = \sum_{m=-M}^{M} \boldsymbol{G}(\vec{r},\vec{r}' - m\Lambda\hat{y}) + \frac{k}{4\mathrm{i}}\sum_{n=-\infty}^{\infty} \mathrm{i}^n J_n(kr)e^{-in\theta}\begin{pmatrix} S_n & -S_{n-1} \\ -S_{n+1} & S_n \end{pmatrix}, \qquad (11)$$

where J_n is the n'th order Bessel function of the first kind and S_n is the n'th order *lattice sum* given by

$$S_n = \sum_{m=M+1}^{\infty} H_n^{(1)}(km\Lambda)\left(\mathrm{e}^{\mathrm{i}k_y m\Lambda} + (-1)^n \mathrm{e}^{-\mathrm{i}k_y m\Lambda}\right). \qquad (12)$$

We have taken the contribution of M unit cells on either side of the zeroth unit cell outside the lattice sum as they may not satisfy the condition for using Graf's theorem. In fact, Graf's theorem is only satisfied when the largest distance between area elements within one unit cell is smaller than $(M + 1)\Lambda$. Therefore, M is chosen to be the smallest integer that satisfies this condition. The lattice sum is actually also extremely slowly convergent, but there are two advantages of writing $\widetilde{\boldsymbol{G}}$ using the lattice sum: 1) The lattice sum does not depend on the observation point, so it needs only be calculated once for a given choice of $k\Lambda$ and angle of incidence φ, and 2) it can be calculated efficiently using the integral representation described in [39].

The transmittance $T(E)$ of an electron with energy E through the barrier is simply the transmitted current $I(E)$ at that energy divided by the incident current I_0. The current is calculated by integrating the x-component of the current density over one period $I = \int_{uc} j_x\, dy$, where the current density is given by $j_x = \Psi^\dagger \hat{j}_x \Psi$ using the current density operator $\hat{j}_x = -ev_F\sigma_x$. The experimentally relevant quantity is the total current I expressed as a function of bias voltage V_B given by [40]

$$I(V_B) = \frac{2e}{h}\int_{-\infty}^{\infty} T(E)[f(E, E_F + eV_B) - f(E, E_F)]\,\mathrm{d}E, \qquad (13)$$

where $f(E, E_F) = (1 + \exp[(E - E_F)/kT])^{-1}$ is the Fermi-Dirac distribution. The only unknown quantity in this expression is the transmittance function $T(E)$. The transmittance function has more distinct features than the current and we therefore show this quantity instead

of the current in most cases. In the limit of vanishing bias, the conductance is $G = G_0 T$, where $G_0 = 2e^2/h$ is the conductance quantum.

In order to assess the accuracy of our model, we compare our results with spectra calculated using the Landauer approach with a nearest-neighbor TB Hamiltonian, as outlined in [29]. We use a hopping integral of $\gamma = 3.033$ eV and, for numerical stability, we add a small imaginary part to the energy, such that $E \to E + i\varepsilon$, where we use $\varepsilon = 10^{-5}$ eV. In the Dirac models, we average over valleys in order to obtain the transmittance per valley. All TB spectra are therefore divided by a factor of two in order to directly compare with the DE.

In order to make a quantitative comparison between the models for a wide range of structures, we define a transport gap using the lowest positive energy, at which the transmittance rises above 1/2. Due to exact electron-hole symmetry, the transport gap will then be twice this energy. Long zigzag edges give rise to very localized states in TB. However, in a real device with even a small amount of disorder, we do not expect these states to support electronic transport. This effect can be introduced heuristically by convolving the TB transmittance spectra with a Gaussian or by using a larger imaginary part of the energy $i\varepsilon$. Therefore, in our calculations of the transport gap we convolve with a Gaussian having a full width at half maximum of $0.1\,\text{eV}/L$.

The transport gap of a GAB may be approximated by replacing the actual structure with a simple barrier as shown in figure 1(*c*). This type of barrier is referred to as a Dirac mass barrier (DMB) and was shown by Pedersen *et al* to be in good agreement with tight-binding in the gap region [29]. In this approach, we define the width of the barrier as $w = N(3L/2)$ and take the barrier height Δ to be half the band gap of the fully periodic case. We use the approximation of the band gap given by equation A6 in [12]. This approach thus offers a quick way to estimate the transport gap.

3. Results and discussion

In this section, we present the results of our Dirac model and compare them with TB. Furthermore, we compare transport gap spectra with the DMB model. Results are presented for both armchair and zigzag antidots. The geometries used in our Dirac model are created such that the total area of the antidots equals the total area of the removed atoms of the corresponding structure used in TB.

3.1. Armchair antidots

We start out by considering GABs in GAL configuration containing armchair antidots. The transmittance spectra of two different barriers with armchair antidots is shown in figure 2. The results are only displayed for positive energies, as the results for negative energies follow from exact electron-hole symmetry in the models. There is excellent agreement between TB and our Dirac model. Furthermore, it is seen that there are always $N - 1$ subpeaks in the transmittance peak, which is consistent with previous calculations for graphene nanoribbons with antidot arrays [41]. This means that as the number of

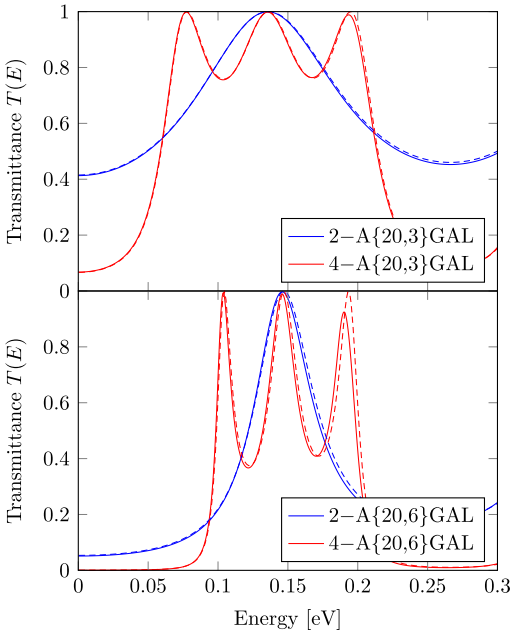

Figure 2. Transmittance of GABs with armchair antidots calculated with TB (solid) and the DE (dashed).

antidots in the unit cell increases, the subpeaks will come closer to each other and eventually merge into a single step-like plateau.

In order to gain insight into the electronic transport through a GAB, we compute the electron probability density for a 4−A{20, 6}GAL barrier at two different electron energies, as shown in figure 3. The two lowest bands in the electronic band structure for the fully periodic structure have energies in the intervals [0.09; 0.24] eV and [0.31; 0.50] eV as given in [12]. We expect low transmittance in the band gap regions of the fully periodic structure and high transmittance elsewhere. At $E = 0.15$ eV, the electron has an energy within the first band, and the probability density inside the barrier is therefore quite high, which results in a very high transmittance of $T \simeq 0.91$. However, at $E = 0.3$ eV, the electron has an energy within a band gap, and the probability density inside the barrier is therefore rather low, which results in a much lower transmittance of $T \simeq 0.02$. This means that the transmittance is low for energies at which the barrier region does not support any electron states.

Armchair antidots do not support localized edge states, which means that, in the limit of very wide barriers, the transport gap should equal the band gap of the fully periodic structure. It is interesting, however, to see if a barrier with only a few antidots in the unit cell is able to block electron transport in the band gap region. Figure 4 shows the transport gap of a large range of GABs with just 4 antidots in the unit cell. In accordance with [12], the results are scaled with the total area of the GAL unit cell $A_{\text{tot}} = 3\sqrt{3}L^2/2$ and the area of a single antidot A_{rem}. It is seen that the transport

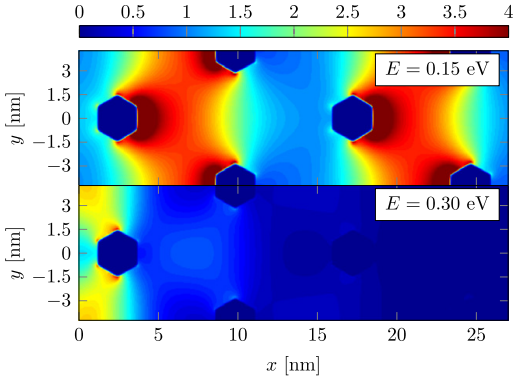

Figure 3. Probability density of electrons in a 4−A{20,6}GAL barrier calculated using the DE. The probability density is measured relative to the incident wave.

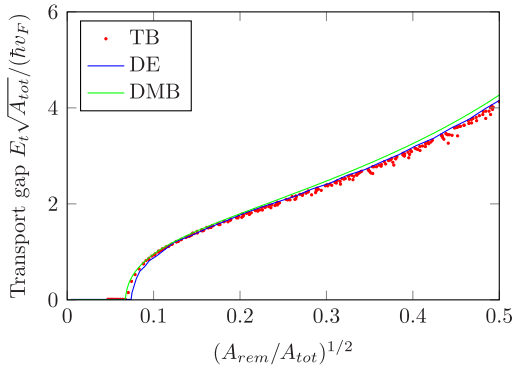

Figure 4. Transport gap of 4−A{L, S}GAL barriers calculated using TB, the DE and the DMB model.

gap opens up for antidots with a size $(A_{\text{rem}}/A_{\text{tot}})^{1/2} > 0.07$. The transport gap is exactly zero for small antidots, as the transmittance is higher than $1/2$ at vanishing energy. The abrupt opening of the transport gap is due to the horizontal slope of the transmittance as a function of energy at small energies. This means that as soon as the structure is large enough for the transmittance at vanishing energy to fall below $1/2$, the transport gap will increase rapidly. The exact location of the onset of the transport gap is, thus, sensitive to the choice of transport gap definition. However, the remaining values are not too sensitive to the exact definition of the transport gap, since the slope of the transmittance spectrum is typically very large near the transport gap. It is seen that both Dirac models are in excellent agreement with TB.

3.2. Zigzag antidots

Transmittance spectra calculated with our Dirac model for two different barriers with zigzag antidots are shown in figure 5 and compared to TB. There is a fairly good agreement between the models for the smaller antidots, but the agreement is very poor for the larger structure. These deviations arise due to the

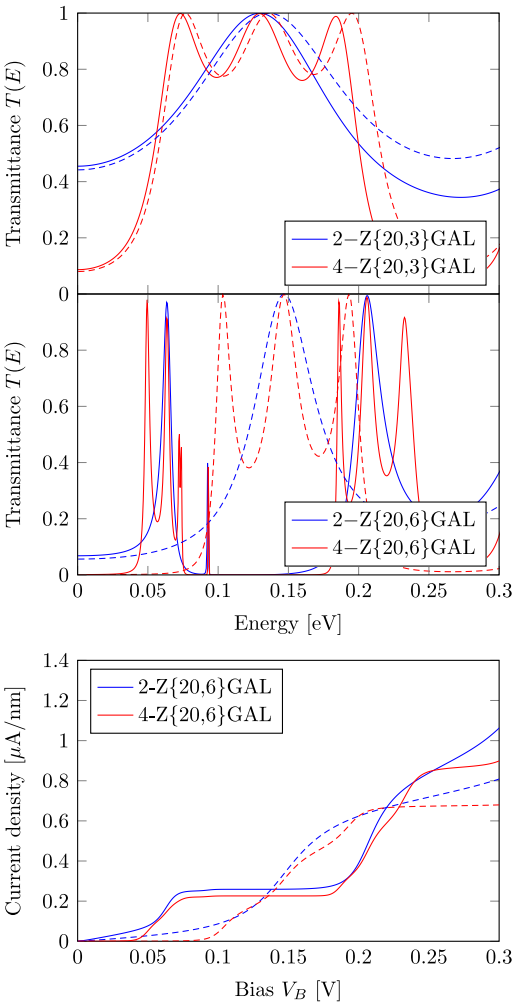

Figure 5. Transmittance (top) and current density (bottom) of GABs with zigzag antidots calculated using TB (solid) and the DE (dashed).

highly localized state in the TB spectrum near 0.09 eV, which is a result of the long zigzag edges. The deviations between TB and the DE have also been observed in the calculation of the band gap of fully periodic GALs [12]. The current density as a function of bias voltage can be calculated from equation (13) by dividing the current with the period of the unit cell. It follows from the equation that the current densities will be similar for similar transmittance functions. This is the case for GABs with armchair antidots. However, for structures like the 4-Z{20,6}GAL, where there is poor agreement of the transmittance function between TB and DE, the current densities will also be in poor agreement. This is illustrated in figure 5, where the current density has been calculated assuming a temperature of 30 K.

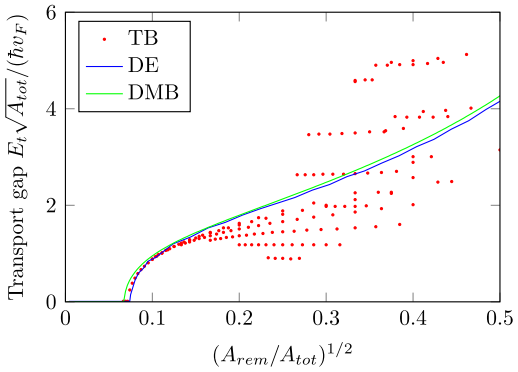

Figure 6. Transport gap of 4−Z{L, S}GAL barriers calculated using TB, the DE, and the DMB model.

It has previously been shown that the band gap shrinks substantially, compared to simple scaling laws, for structures with large zigzag antidots due to the presence of edge states [12]. The shrinking of the band gap is only predicted by the TB model, as the DE with a mass term does not distinguish between zigzag and armchair edges. In the calculation of the transport gap, we overcome some of the effects of very localized edge states in our TB calculations by convolving all TB transmittance spectra with a Gaussian. This smears out very narrow features of the transmittance spectra, while preserving those that are not. We compare the transport gap calculated with the DE with those calculated with TB and the DMB model in figure 6. The Dirac models are in fairly good agreement with TB for small antidots with size $(A_{\rm rem}/A_{\rm tot})^{1/2} < 0.15$. However, for larger antidots, there is generally a poor agreement. This is again due to the presence of localized states in the TB spectra. An interesting aspect of the TB transport gap, however, is that it is generally much higher than the TB band gap, which is given in [12]. TB predicts that the band gap almost closes for large zigzag antidots, whereas the TB transport gap does not. In fact, the TB transport gap is often higher than the one predicted by the Dirac models. This means that the transport gap of zigzag antidots can be higher than that of similarly sized armchair antidots, which contradicts the behavior of the band gap [12]. This is in good accordance with recent studies that showed that localized states in non-commensurate antidot lattices do not contribute to electronic transport [42]. Since the localized edge states typically lie beneath non-localized states, they will generally increase the transport gap. This also agrees with the results of Jippo *et al* [43] who calculated the transport gap for irregularly shaped antidots. They showed that the transport gap generally increases with the length of consecutive zigzag regions in the antidot. The transport gap of armchair antidots is highly predictable, as it follows the simple result from the DMB very accurately, whereas the transport gap of zigzag antidots is much less predictable. Therefore, even though the transport gap can be higher in some cases for zigzag antidots compared to armchair antidots, it may be an advantage to use armchair antidots in an experimental setup.

Brey and Fertig [44] have shown that by using appropriate boundary conditions in the DE, it is possible to obtain an accurate description of edge states in graphene nanoribbons with zigzag edges. They find that the A spinor element of the wave function must vanish on A-terminated edges, while the B spinor element must vanish on B-terminated edges. We can approximate the boundary conditions in the DE by introducing separate mass terms for the two sublattices and then letting the A/B mass term be non-zero only on A/B-terminated edges. Indeed, we find that this gives rise to localized states for fully periodic GALs using the method in [12]. However, the exact energies of the localized states are very sensitive to the magnitude of the mass term. It is therefore only possible to obtain a qualitative description of zigzag antidots with this approach. Unfortunately, implementing mass terms that are localized to the edges is complicated in the present area-based approach. We therefore restrict calculations to simple uniform mass terms.

3.3. Disorder

Up to now, the effect of disorder has been taken into account by convolving the TB spectra with a Gaussian. In reality, the effect of disorder is of course much more complex and needs to be studied in more detail. Ouyang *et al* [45] have shown that GALs with even neck widths, i.e. number of zigzag rows between neighboring antidots, are semiconducting, while those with odd neck widths are semimetallic. This means that randomization of antidot placement may lead to a local closing of the band gap and thus lead to local conduction channels in a GAB. Liu *et al* [46] have demonstrated that randomly oriented fullerene adsorption on pristine graphene gives rise to sizable band gaps on the order of 0.35 eV, due to the breaking of the sublattice symmetry. This indicates that a band gap, which has closed due to disorder, may recover in the presence of adsorbates. Our Dirac model is able to model any distribution of antidots, and we can thus introduce disorder by e.g. introducing randomization of antidot center location. We set up the displacement of the antidots to follow a normal distribution with a certain choice of standard deviation σ. All displacements are then mapped to the nearest graphene hexagon center in order to preserve the shape of the antidots in TB. A property of the normal distribution is that the mean displacement is given by $\sigma\sqrt{2/\pi}$. In figure 7, we show the effect of disorder for different values of σ for a 4-A{20,6}GAL barrier. As there are only 4 antidots in the unit cell, we average over transmittance spectra of several structures until the resulting spectrum does not change significantly. Figure 7 shows that the effect of disorder is more pronounced in TB than in our Dirac model. In fact, the DE spectra are almost unchanged in the presence of these amounts of disorder. In contrast, the TB transmittance maxima generally decrease with increasing disorder and new transmission peaks appear in the spectrum. For instance, a new transmission channel opens up at low energies with a peak at approximately 0.05 eV. This new channel may open due to the presence of odd neck widths between some of the antidots after random displacement, which, according to the results of Ouyang *et al*, could lead

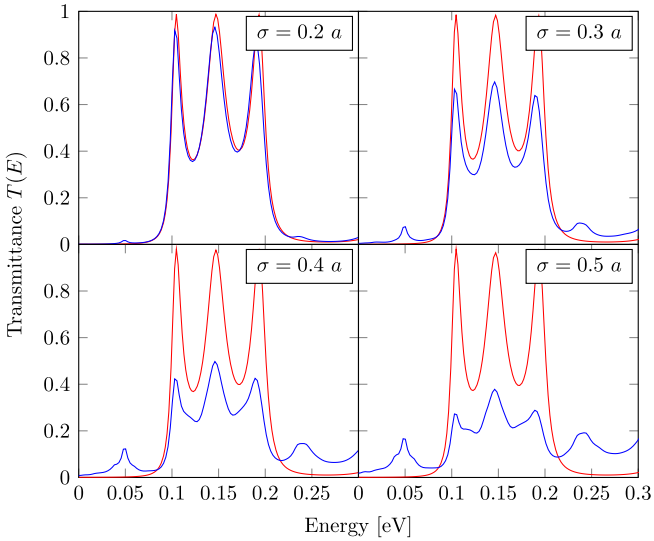

Figure 7. Average transmittance spectra of 4-A{20,6}GAL barriers for different degrees of disorder calculated with the DE (red) and TB (blue). Disorder was introduced by randomly displacing the center of the antidots according to a normal distribution.

to semimetallic regions in the barrier. The DE is a continuum model and can therefore not distinguish between the atomistic details of even and odd neck widths, and is therefore unable to predict the difference between them. It should be noted that a proper analysis of the effects of disorder requires one to construct a large supercell consisting of several disordered subcells. However, this quickly becomes very time consuming and we therefore use the original disordered GAB unit cell and then average over the results.

4. Conclusions

We use a Green's tensor area integral equation method to solve the Dirac equation with a spatially varying mass term. In this way, we are able to calculate the scattering of Dirac electrons on arbitrary graphene antidot structures. We use this method to calculate the transmittance of graphene antidot barriers with hexagonal antidots and compare them with results obtained using tight-binding. Our approach is much more general than previous attempts to use the Dirac equation to calculate scattering of Dirac electrons on antidots. The computational time of our Dirac model is scale invariant, which means that we are able to calculate properties of arbitrarily large structures. We show that our Dirac model is in excellent agreement with tight-binding for antidots with armchair edges. We also show that a simple Dirac mass barrier is able to predict the transport gap with high accuracy for antidots with armchair edges. Tight-binding predicts very localized edge states for large zigzag antidots, whereas the Dirac models do not. Therefore, the agreement between the Dirac models and tight-binding is generally poor when the barrier contains antidots with long zigzag edges. We show that the tight-binding transport gap for zigzag antidots is larger than for armchair antidots with equivalent size for some geometries, while it is lower for others. However, since the transport gap for armchair antidots is much more predictable, it may still be an advantage to use armchair antidots in an experimental setup. Furthermore, we show that a relatively narrow GAB, with only a few antidots in the unit cell, is sufficient to give rise to a transport gap. Finally, we have used our Dirac model to study disordered systems and find that it is not accurate for modeling systems with a large degree of disorder, but remains robust against relatively small amounts of disorder.

Acknowledgments

The authors gratefully acknowledge the financial support from the Center for Nanostructured Graphene (Project No. DNRF58) financed by the Danish National Research Foundation. We thank T. Søndergaard for helpful discussions on the Green's tensor area integral equation method and its numerical implementation.

References

[1] Novoselov K S, Geim a K, Morozov S V, Jiang D, Zhang Y, Dubonos S V, Grigorieva I V and Firsov A A 2004 *Science* **306** 666–9
[2] Du X, Skachko I, Barker A and Andrei E Y 2008 *Nat. Nanotechnol.* **3** 491–5
[3] Bolotin K I, Sikes K J, Jiang Z, Klima M, Fudenberg G, Hone J, Kim P and Stormer H L 2008 *Solid State Commun.* **146** 351–5
[4] Bolotin K I, Sikes K J, Hone J, Stormer H L and Kim P 2008 *Phys. Rev. Lett.* **101** 096802
[5] Han M Y, Özyilmaz B, Zhang Y and Kim P 2007 *Phys. Rev. Lett.* **98** 206805

[6] Zhang Y, Tang T T, Girit C, Hao Z, Martin M C, Zettl A, Crommie M F, Shen Y R and Wang F 2009 *Nature* **459** 820–3
[7] Xia F, Farmer D B, Lin Y m and Avouris P 2010 *Nano Lett.* **10** 715–8
[8] Balog R *et al* 2010 *Nat. Mater.* **9** 315–9
[9] Pedersen T G, Flindt C, Pedersen J G, Mortensen N A, Jauho A P and Pedersen K 2008 *Phys. Rev. Lett.* **100** 136804
[10] Fürst J A, Pedersen T G, Brandbyge M and Jauho A P 2009 *Phys. Rev.* B **80** 115117
[11] Fürst J A, Pedersen J G, Flindt C, Mortensen N A, Brandbyge M, Pedersen T G and Jauho A P 2009 *New J. Phys.* **11** 095020
[12] Brun S J, Thomsen M R and Pedersen T G 2014 *J. Phys: Condens. Matter* **26** 265301
[13] Petersen R and Pedersen T G 2009 *Phys. Rev.* B **80** 113404
[14] Vanević M, Stojanović V M and Kindermann M 2009 *Phys. Rev.* B **80** 045410
[15] Trolle M L, Møller U S and Pedersen T G 2013 *Phys. Rev.* B **88** 195418
[16] Eroms J and Weiss D 2009 *New J. Phys.* **11** 095021
[17] Giesbers A J M, Peters E C, Burghard M and Kern K 2012 *Phys. Rev.* B **86** 045445
[18] Xu Q, Wu M Y, Schneider G F, Houben L, Malladi S K, Dekker C, Yucelen E, Dunin-Borkowski R E and Zandbergen H W 2013 *ACS Nano* **7** 1566–72
[19] Bai J, Zhong X, Jiang S, Huang Y and Duan X 2010 *Nat. Nanotechnol.* **5** 190–4
[20] Kim M, Safron N S, Han E, Arnold M S and Gopalan P 2010 *Nano lett.* **10** 1125–31
[21] Kim M, Safron N S, Han E, Arnold M S and Gopalan P 2012 *ACS Nano* **6** 9846–54
[22] Zeng Z, Huang X, Yin Z, Li H, Chen Y, Li H, Zhang Q, Ma J, Boey F and Zhang H 2012 *Adv. Mater.* **24** 4138–42
[23] Wang M, Fu L, Gan L, Zhang C, Rümmeli M, Bachmatiuk A, Huang K, Fang Y and Liu Z 2013 *Sci. Rep.* **3** 1238
[24] Liang X, Jung Y S, Wu S, Ismach A, Olynick D L, Cabrini S and Bokor J 2010 *Nano Lett.* **10** 2454–60
[25] Jia X *et al* 2009 *Science* **323** 1701–5
[26] Girit Ç Ö *et al* 2009 *Science* **323** 1705–8
[27] Oberhuber F, Blien S, Heydrich S, Yaghobian F, Korn T, Schüller C, Strunk C, Weiss D and Eroms J 2013 *Appl. Phys. Lett.* **103** 143111
[28] Schwierz F 2010 *Nat. Nanotechnol.* **5** 487–96
[29] Pedersen T G and Pedersen J G 2012 *J. Appl. Phys.* **112** 113715
[30] Gunst T, Markussen T, Jauho A P and Brandbyge M 2011 *Phys. Rev.* B **84** 155449
[31] Pedersen J G, Gunst T, Markussen T and Pedersen T G 2012 *Phys. Rev.* B **86** 245410
[32] Berrada S, Nguyen V H, Querlioz D, Saint-Martin J, Alarcón A, Chassat C, Bournel A and Dollfus P 2013 *Appl. Phys. Lett.* **103** 183509
[33] Masir M R, Matulis A and Peeters F M 2011 *Phys. Rev.* B **84** 245413
[34] Heinisch R L, Bronold F X and Fehske H 2013 *Phys. Rev.* B **87** 155409
[35] Gomes J V and Peres N M R 2008 *J. Phys: Condens. Matter* **20** 325221
[36] Søndergaard T 2007 *Phys. Stat. Sol.* **244** 3448–62
[37] Novotny L and Hecht B 2006 *Principles of nano-optics* (Cambridge University Press)
[38] Abramovitz M and Stegun I A (eds) 1965 *Handbook of Mathematical Functions* (New York: Dover Publications)
[39] Yasumoto K and Yoshitomi K 1999 *IEEE Trans. Antennas Propag.* **47** 1050–5
[40] Datta S (ed) 1997 *Electronic Transport in Mesoscopic Systems* (Cambridge: Cambridge University Press)
[41] Zhang Y T, Li Q M, Li Y C, Zhang Y Y and Zhai F 2010 *J. Phys.: Condens. Matter* **22** 315304
[42] Lopata K, Thorpe R, Pistinner S, Duan X and Neuhauser D 2010 *Chem. Phys. Lett.* **498** 334–7
[43] Jippo H, Ohfuchi M and Kaneta C 2011 *Phys. Rev.* B **84** 075467
[44] Brey L and Fertig H A 2006 *Phys. Rev.* B **73** 235411
[45] Ouyang F, Peng S, Liu Z and Liu Z 2011 *ACS nano* **5** 4023–30
[46] Liu X, Wen Y, Chen Z, Lin H, Chen R, Cho K and Shan B 2013 *AIP Adv.* **3** 052126

Paper III

Stability and magnetization of free-standing and graphene-embedded iron membranes

Morten Rishøj Thomsen, Søren Jacob Brun and Thomas Garm Pedersen

The paper has been published in
Physical Review B **91**, 125439 (2015)

Stability and magnetization of free-standing and graphene-embedded iron membranes

M. R. Thomsen, S. J. Brun, and T. G. Pedersen
Department of Physics and Nanotechnology, Aalborg University, DK-9220 Aalborg Øst, Denmark
and Center for Nanostructured Graphene (CNG), DK-9220 Aalborg Øst, Denmark
(Received 19 November 2014; revised manuscript received 13 March 2015; published 30 March 2015)

Inspired by recent experimental realizations of monolayer Fe membranes in graphene perforations, we perform *ab initio* calculations of Fe monolayers and membranes embedded in graphene in order to assess their structural stability and magnetization. We demonstrate that monolayer Fe has a larger spin magnetization per atom than bulk Fe and that Fe membranes embedded in graphene exhibit spin magnetization comparable to monolayer Fe. We find that free-standing monolayer Fe is structurally more stable in a triangular lattice compared to both square and honeycomb lattices. This is contradictory to the experimental observation that the embedded Fe membranes form a square lattice. However, we find that embedded Fe membranes in graphene perforations can be more stable in the square lattice configuration compared to the triangular. In addition, we find that the square lattice has a lower edge formation energy, which means that the square Fe lattice may be favored during formation of the membrane.

DOI: 10.1103/PhysRevB.91.125439 PACS number(s): 75.75.−c, 61.48.Gh, 75.50.Bb, 75.70.Ak

I. INTRODUCTION

In recent years, there has been a tremendous interest in graphene and its derivatives, owing to their remarkable electronic properties, such as ultrahigh mobility of 1 000 000 cm^2/Vs at low temperature [1]. These properties make graphene interesting for electronic and spintronic applications. Carbon-based spintronic devices may have a distinct advantage over many other materials in that carbon has a very low spin-orbit coupling together with an absence of hyperfine interaction in the predominant ^{12}C isotope. This results in long spin lifetimes [2–4], as well as large spin relaxation lengths, which have been found to be on the order of several microns at room temperature [2–5] and make graphene ideal for ballistic spin transport [6].

Pristine graphene is nonmagnetic, but several suggestions on how to give graphene magnetic properties have been put forward. Density functional theory (DFT) calculations have shown that ferromagnetism can be introduced in graphene by, e.g., semihydrogenation [7], adding vacancies [8,9], or adding adatoms [9–14]. Semihydrogenating graphene sheets, where one sublattice is fully hydrogenated while the other is not, leads to a sublattice imbalance, which induces a magnetic moment of $1\mu_B$ per unit cell [7]. Monovacancies in graphene have also been demonstrated to have a magnetic moment between $1.04\mu_B$ [8] and $1.48\mu_B$ [9]. Lehtinen *et al.* [8] find that the spin-polarized state may be unstable, and find that it can be stabilized by adsorption of two hydrogen atoms in the vacancy, with a resulting magnetic moment of $1.2\mu_B$. The spin of a vacancy generally increases with the number of missing carbon atoms, except for the divacancy where the magnetic moment is vanishing [9]. Ferromagnetism can also be induced by transition metal adatoms on graphene or in graphene vacancies. Transition metal adatoms in graphene and single-walled carbon nanotubes were studied by Zanella *et al.* [10] and Fagan *et al.* [15], respectively. In particular, they find that the spin moment of Fe adatoms is largely unaffected by the presence of carbon. Zanella *et al.* find that the spin moment of Fe adsorbed on graphene is either 2 or $4\mu_B$ depending on the adsorption site, while Fagan *et al.* find that the spin moment of Fe adsorbed on a carbon nanotube is about $3.9\mu_B$ independent of adsorption site. DFT calculations show that a single Fe adatom on a graphene monovacancy is nonmagnetic [11–13]. However, by adding a Hubbard U term to the GGA functional, Santos *et al.* [12] showed that this state may, in fact, be magnetic with a spin moment of $1\mu_B$, and that the nonmagnetic properties predicted by the GGA calculation is a consequence of the limitations of the functional itself. Nevertheless, the spin moment of a single Fe adatom on a graphene monovacancy is strongly decreased compared to free Fe, due to the Fe-C interaction. A single Fe adatom in a graphene divacancy, however, has a spin moment of about $3.2\mu_B$ according to Krasheninnikov *et al.* [11], and $3.55\mu_B$ according to He *et al.* [13]. The reason for the increased spin is quite obvious; the larger vacancy increases the Fe-C distance and thus decreases the interaction between Fe and C. As the interaction between Fe and C seems to decrease the spin moment of Fe, we expect Fe-C systems to have decreased spins compared to a pure Fe system. Trapping larger Fe clusters in graphene perforations will lead to a larger spin moment, which combined with the electrical properties of graphene, might make this a suitable system for graphene-based spintronics.

Trapping of metal atoms, such as Fe and Mo, in graphene and carbon nanotube vacancies have been achieved experimentally in transmission electron microscopy (TEM) [14,16]. Vacancies are created under e-beam irradiation, after which mobile metal atoms on the surface move to the vacancy, where they are trapped. These trapped metals are stable for some time, but detrapping of some of the atoms has been observed over time [14,16], which is thought to occur due to weak bonding, e-beam irradiation, or high temperature during the experiments. Recent experimental results by Zhao *et al.* [17] show that monolayer Fe membranes can be grown in graphene perforations. These monolayer membranes both form and collapse under e-beam irradiation in TEM. The Fe is provided via leftover residue from the transfer process, where graphene is transferred from growth substrate to target substrate. Electron energy loss spectroscopy (EELS) and high-angle annular dark-field (HAADF) measurements suggest that the embedded membranes are composed of pure Fe. They find

that the embedded Fe membranes form a square lattice with a lattice constant of about 2.65 Å. Through density functional theory (DFT) calculations, Zhao *et al.* find that monolayer Fe is most stable in a square configuration with a lattice constant of 2.35 Å. They argue that the difference between observed and calculated lattice constant may be a result from straining due to lattice alignment and mismatch between the Fe membrane and graphene.

In this paper, we present a DFT analysis of the structural stability and magnetization of Fe systems in an attempt to obtain a basic understanding of these systems, as well as to explain the experimental results by Zhao *et al.* [17]. In particular, we compare the stability of Fe in square and triangular lattice configurations for both monolayer Fe, monolayer Fe carbide and Fe embedded in graphene perforations. We model embedded Fe membranes as a periodic system, effectively giving rise to graphene antidot lattices (GALs), where the antidots are filled with Fe. GALs, which are periodic perforations in an otherwise pristine graphene sheet, can be produced experimentally by, e.g., e-beam lithography on pristine graphene [18,19]. It is possible that the embedding of iron in graphene perforations can be scaled up to actual Fe-filled GALs. GALs have tunable band gaps that depend on geometric factors [20,21], which make them interesting for electronic and optoelectronic applications. It has been shown that a narrow slice of GAL with just a few rows connected to graphene sheets on either side is sufficient to block electron transport in the energy gap of the GAL [22,23]. By omitting antidots in some regions of such a GAL barrier, electrons can be guided through the unpatterned part, giving rise to an electronic waveguide [24], reminiscent of a photonic waveguide in a photonic crystal.

II. THEORETICAL METHODS

Spin-polarized DFT calculations were performed using the ABINIT package [25–28], which uses a plane-wave basis set to expand the wave function. We have used the Perdew-Burke-Ernzerhof GGA (PBE-GGA) exchange and correlation functional [29] in all calculations. We use a plane-wave cutoff energy of 435 eV combined with the projector-augmented wave (PAW) method [30]. It has previously been demonstrated that the PAW method is able to accurately describe magnetism in transition metal systems [30,31]. We use a Fermi smearing of 0.27 eV in order for a $16 \times 16 \times 1$ Monkhorst-Pack k-point grid to be adequate. The Fermi smearing has the effect of slightly lowering the magnetic moment as electrons will have a probability to occupy states above the Fermi level. An interlayer spacing of 10 Å was used in all calculations. Full relaxation of all atoms in the unit cells were made for all structures, in addition to relaxation of the unit cell size in the case of free-standing monolayer Fe and iron carbide. Atomic coordinates were optimized until the maximum force on atoms was smaller than 0.05 eV/Å. These parameters have previously been shown to be adequate for modeling transition metal adatoms on graphene vacancies [8,11]. The same parameters are used when calculating the edge formation energy, except the k-point sampling is reduced to $16 \times 1 \times 1$, due to a lateral distance between ribbons of 10 Å.

III. FREE-STANDING MONOLAYER SYSTEMS

A. Monolayer iron

In order to obtain an understanding of iron membranes embedded in graphene perforations, we first determine the stability of free-standing monolayer iron in different lattice configurations. Then, we calculate the edge formation energy of monolayer iron, in order to obtain an understanding of the formation kinetics of iron membranes. Lastly, we determine the stability of iron membranes embedded in graphene antidots for certain hole sizes.

The binding energy and magnetization of free-standing monolayer iron in square, triangular, and honeycomb lattice configurations are shown in Fig. 1. The antiferromagnetic square and honeycomb lattices are made such that each atom only has nearest neighbors with opposite spin. This is not possible in the triangular lattice, so we chose an antiferromagnetic lattice that essentially consists of spin-polarized lines, where each atom has opposite spin to four of its six nearest neighbors. We do not expect this configuration to be physically sound, but we include it in order to compare with the other lattice configurations. We use the smallest possible unit cells, which means that the ferromagnetic unit cells of the square and triangular lattice contain one atom and the honeycomb lattice contains two. In the antiferromagnetic case, all three unit cells contain two atoms. The figure shows that ferromagnetic ordering is generally favored over antiferromagnetic ordering, consistent with earlier results which show that monolayer Fe

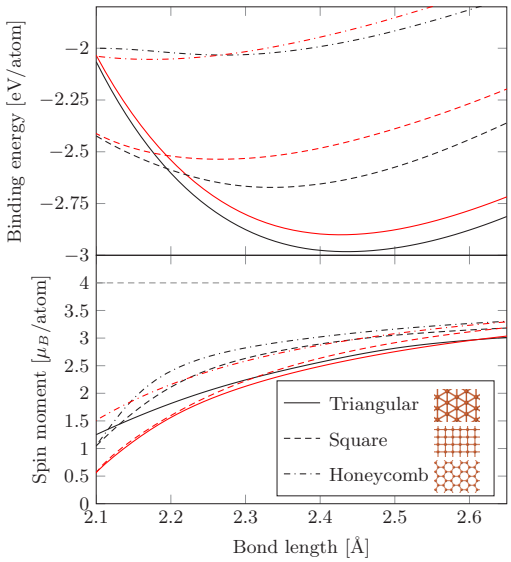

FIG. 1. (Color online) Binding energy (upper panel) and spin moment (lower panel) of monolayer Fe as a function of bond length. The black and red lines are for ferromagnetic and antiferromagnetic ordering, respectively. The magnitude of the spin is shown in case of antiferromagnetic ordering, as it has zero net spin. The dashed gray line indicates the spin of free Fe.

in the square lattice favors ferromagnetic ordering [32]. The figure also shows that the honeycomb lattice is unfavored compared to the square and triangular lattices. We therefore exclude antiferromagnetic ordering as well as the honeycomb lattice in the remaining calculations. In addition, the figure shows that the most stable configuration is the ferromagnetic triangular lattice, as it has the lowest binding energy at equilibrium. However, it is seen that, under compressive strain, the ferromagnetic square lattice eventually becomes favored. The spin moments per atom at equilibrium are $2.73\mu_B$ and $2.68\mu_B$ for the square and triangular lattice, respectively, which is significantly larger than the bulk spin moment of $2.22\mu_B$ [33]. Our results for the spin of the ferromagnetic triangular lattice are in good agreement with previous results [34,35].

As expected, we see that the spin moment increases with increasing distance between the Fe atoms, as the spin tends towards $4\mu_B$ for free Fe. We notice that the bond length at equilibrium of the square lattice is 2.33 Å, which is significantly lower than the experimental results of 2.65 Å by Zhao *et al.* [17], suggesting that the Fe membranes are strained by the surrounding graphene. In addition, it is seen that the energy cost of straining the square lattice to 2.65 Å is only about 0.2 eV per atom. Our predictions of the lattice constant and energy cost of straining for the square monolayer Fe lattice are very close to the theoretical results by Zhao *et al.* The major difference between the results is that we find the triangular lattice to be more stable, whereas Zhao *et al.* find that the square lattice is more stable, in agreement with their experimental observations that Fe embedded in graphene perforations forms a square lattice. The differences in the calculations are that we use a plane wave basis set and a $16 \times 16 \times 1$ k-point sampling, whereas Zhao *et al.* use a localized basis and a $3 \times 3 \times 1$ k-point sampling. The elementary unit cells for monolayer Fe are very small, and we find that a $3 \times 3 \times 1$ k-point sampling is insufficient for obtaining converged spin magnetization and total energy. We therefore believe that the discrepancy arises due to the different k-point sampling.

B. Edge energy of monolayer iron

We have demonstrated that the triangular lattice is energetically favored over the square lattice, so in order to explain why the square lattice is formed experimentally, we now analyze the edge formation energy by comparing the energy of an Fe nanoribbon and monolayer Fe. The edge formation energy per length is given by $E_{\text{edge}} = (E_{\text{ribbon}} - NE_{\text{monolayer}})/2l$, where l is the length of the unit cell in the direction of the ribbon edge, E_{ribbon} is the total energy of the nanoribbon unit cell, N is the number of atoms in the unit cell, and $E_{\text{monolayer}}$ is the energy per atom of the monolayer system. The factor of $1/2$ is due to the fact that a nanoribbon has two edges. For both the square and the triangular lattice, we examine two different rotations of the edges, as shown in Fig. 2.

In Fig. 3(a) we observe that the triangular lattice has a larger edge formation energy than the square lattice for both rotations of both lattices. This means that, during formation of the membrane, the square lattice may be favored due to the lower edge formation energy. The membrane may then be kinetically hindered from subsequently rearranging into the triangular lattice. It is seen in Fig. 3(b) that the bond length contracts on the edges of the ribbon, while the remaining structure is almost unchanged. This indicates that the large experimentally observed lattice constant is not due to formation kinetics.

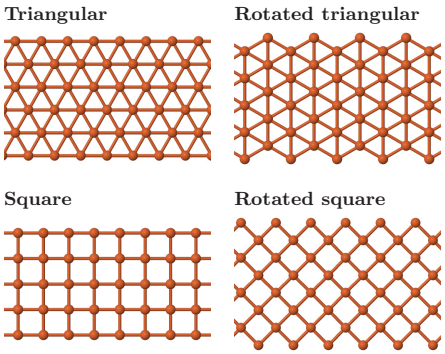

FIG. 2. (Color online) Geometries used for evaluation of edge energies.

C. Iron carbide

Another possibility is that the experimentally observed structure is, in fact, an iron carbide. Zhao *et al.* state that relatively small amounts of carbon may lie beyond the

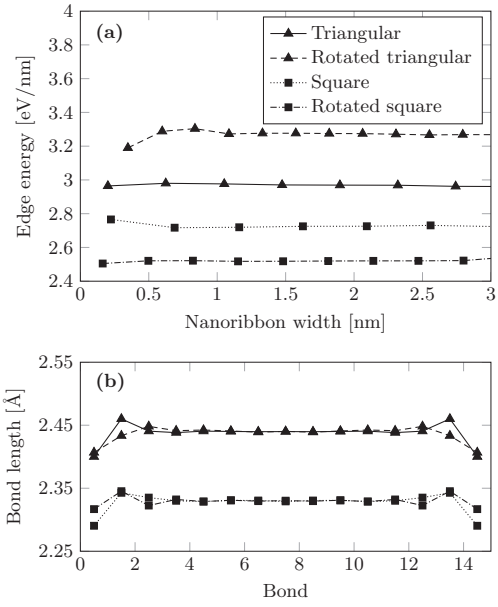

FIG. 3. (a) Edge formation energy for square and triangular Fe nanoribbons as a function of nanoribbon width. (b) Bond lengths through a 16-atom-wide Fe nanoribbon with different orientations and edge rotations.

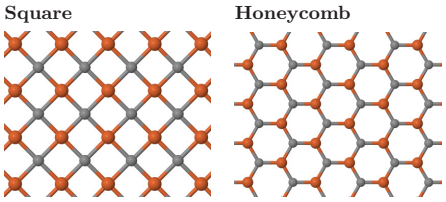

FIG. 4. (Color online) Iron carbides with square and honeycomb arrangements. The gray balls are C and the orange balls are Fe.

detection limits of their EELS setup and therefore cannot exclude the possibility that the membrane is made of iron carbide. It is also very difficult to observe C atoms near Fe in TEM due to the large difference in contrast. The iron carbides shown in Fig. 4 have binding energies per unit cell of -9.91 eV and -9.49 eV for the square and honeycomb lattice, respectively. The square lattice is thus the most stable configuration. The sum of the binding energy of separate monolayer Fe and graphene systems is -10.37 eV. The energy difference between the separate systems and the iron carbide is just 0.46 eV, which suggests that the iron carbide in square arrangement could be metastable. In particular, it is interesting to note that the lattice constant, i.e., the Fe-Fe distance, of the square iron carbide is 2.66 Å, which is extremely close to the experimentally observed value. However, since we find the structure to be, at best, metastable and no carbon signal was observed in EELS experiments, we are still skeptical that the observed structure is, in fact, iron carbide. More accurate measurements are needed in order to exclude the possibility of the membranes consisting of iron carbide.

IV. EMBEDDED IRON

We will now study the structural stability and magnetization of Fe membranes embedded in graphene perforations. In order to model this with DFT, we impose periodic boundary conditions, which means we effectively have a graphene antidot lattice (GAL), where the antidots are filled with Fe. We use the conventional $\{L,S\}$ notation to denote GALs with unit cell side length L and antidot side length S, both in units of the graphene lattice constant, consistent with earlier work [36]. By filling a given antidot with the same amount of Fe atoms in the square and triangular configurations, we can make a direct comparison of the stability of the two systems by comparing their binding energies. In particular, we compare 12 and 21 Fe atoms embedded in a {4,2} and a {5,3} antidot lattice with hexagonal hole geometry, respectively. These antidot lattices are chosen because both square and triangular lattice configurations with an equal amount of Fe atoms can be found that conform fairly well with the antidots. Figure 5 shows the structures after relaxation of all atoms in the unit cell.

The figure shows that the surrounding graphene is almost unaffected by the presence of Fe, due to the large in-plane strength of graphene. It is also seen that the Fe bulges out-of-plane for the small antidots, especially for Fe in square arrangement. This indicates that the square lattice does not conform as well to the graphene lattice as the triangular lattice

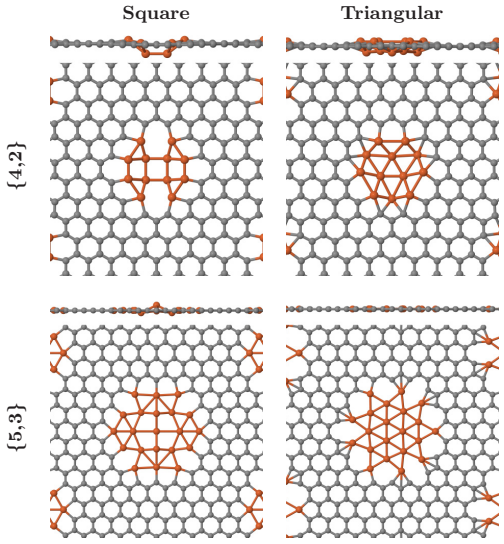

FIG. 5. (Color online) Top and side view of structurally relaxed graphene antidots with embedded Fe.

does for the small antidot. In the larger antidot, the Fe is seen to be mostly co-planer with the graphene, which indicates that both lattice configurations conform better to the graphene lattice. The Fe still bulges slightly out-of-plane in the square lattice configuration, which indicates that the square lattice still conforms worse to the graphene lattice than the triangular lattice. By comparing the binding energies of the two systems, we can determine which of the Fe configurations is more stable.

The unit cells we consider are probably too small for the spins to be decoupled between neighboring cells. This means that the magnitude of the magnetic moment may differ for isolated Fe membranes in graphene. However, due to the high strength of the supporting graphene lattice, we expect that structural properties will be in quantitative agreement with isolated Fe membranes.

We find that the triangular lattice is favored in the {4,2} antidot lattice with a binding energy difference of 2.31 eV, while the square lattice is favored in the {5,3} antidot lattice with a binding energy difference of 1.37 eV. The fact that the square lattice is favored in the large antidot, despite conforming worse to the graphene lattice, indicates that the square lattice has a larger binding energy to graphene than the triangular lattice. We therefore presume that the square lattice will have a greater advantage in larger antidots, where it conforms better to the graphene lattice. However, when the Fe membrane grows too large, the "bulk" behavior should overcome edge or interface effects, which should lead to formation of the triangular Fe lattice. Moreover, there is still the possibility that a 3D nanocrystal could form instead of the triangular monolayer membrane as the 3D structure, in principle, has lower energy than the 2D counterpart for sufficiently large structures. We thus speculate that there is an antidot size regime, where the square Fe lattice is favored, but

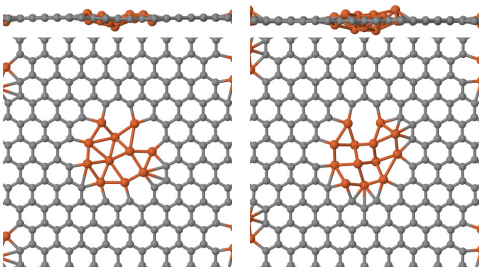

FIG. 6. (Color online) Top and side view of structurally relaxed {4,2} graphene antidot lattices with 11 (left) and 13 (right) Fe atoms.

when the antidots become too large, either the triangular monolayer Fe lattice or a 3D nanocrystal will be formed instead. However, we cannot investigate the extent of this regime further, due to the computational complexity of the DFT calculations.

In the analysis of the {4,2} unit cell, the choice of 12 Fe atoms was made to ensure a symmetric structure in both triangular and square arrangements. In order to substantiate our conclusions regarding the relative stability of these arrangements, we now investigate the {4,2} unit cell with a varying number of Fe atoms. In this case, we place the Fe atoms asymmetrically in the unit cell to obtain convergence to the global structural minimum. For the structure with 12 Fe atoms, the fully relaxed structure is the triangular one shown in the top right in Fig. 5. We find that a structure with 11 Fe atoms is more stable than the structures with either 12, 13, or 14 Fe atoms. The difference in binding energy per atom between the structure with 11 and 12 Fe atoms is only 30 meV, however, which is much smaller than the difference in binding energy obtained by changing the lattice configuration between square and triangular. The relaxed structures in the cases of 11 and 13 Fe atoms are shown in Fig. 6. The figure shows that the structure with 11 Fe atoms approximately forms a triangular

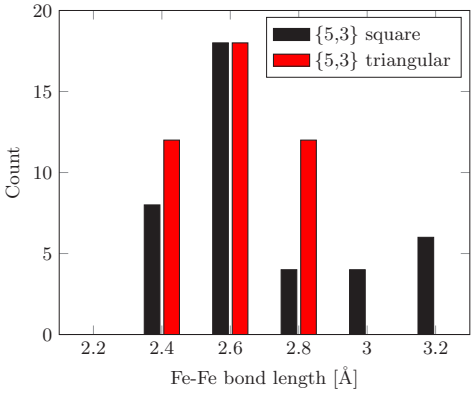

FIG. 7. (Color online) Fe-Fe bond lengths of the two {5,3} structures shown in Fig. 5.

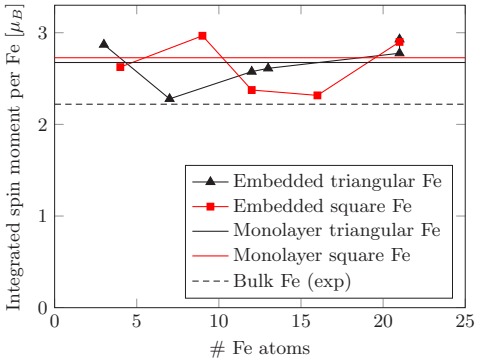

FIG. 8. (Color online) Integrated spin moment per atom for Fe membranes embedded in graphene antidots.

lattice, which is however a bit distorted because there is no longer any symmetric way to arrange the atoms. Furthermore, we see that the structure with 13 Fe atoms forms a square lattice, but it is no longer planar, simply because there is not enough room in the antidot to support a planar structure with this many Fe atoms. The conclusion that the triangular lattice

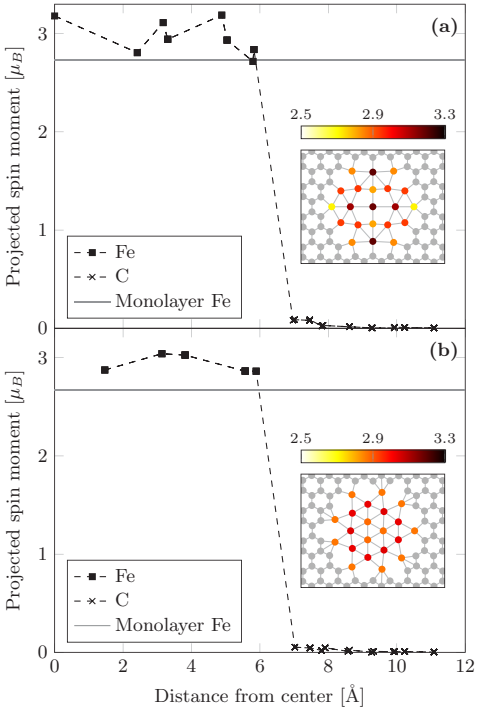

FIG. 9. (Color online) Projected spin moment for a {5,3} graphene antidot lattice with 21 Fe atoms in a hexagonal antidot in (a) square arrangement and (b) triangular arrangement.

is stable in the {4,2} unit cell is thus unchanged when varying the number of Fe atoms by a few units.

We saw previously that there was a rather large discrepancy between the bond lengths of the bulk monolayer Fe and the one measured in the experiments. To further investigate this discrepancy we have counted all the Fe-Fe bond lengths in the two {5,3} antidot structures in Fig. 7. The figure shows that the Fe-Fe bond length inside the graphene antidots is generally quite close to the one measured experimentally, with a mean value of 2.7 Å and 2.6 Å in the square and triangular cases, respectively. The square lattice is thus strained by about 16% on average compared to the bulk monolayer value. By comparison, the mean C-C bond length is almost unaffected by the interface with a mean value of 1.43 Å in both cases.

Figure 8 shows that the spin moment per Fe atom embedded in graphene antidots is around the value of monolayer Fe even for very few embedded Fe atoms. In contrast to Fe in a graphene monovacancy, where the spin moment is vanishing, the spin moment is only weakly affected by the presence of carbon on the edge. In fact, the spin moment may in some cases even exceed the monolayer value, due to the increased bond lengths. This is consistent with the result for Fe in a graphene divacancy, where the spin moment is also only weakly affected by the presence of carbon. This effect can be seen directly in Fig. 9, which shows the projected spin moment as a function of distance from the center of the antidot for a {5,3} graphene antidot lattice with 21 Fe atoms. The projected spin moment is calculated by integrating the difference in spin-up and spin-down electron densities inside the Voronoi volume associated with each atom. The figure shows that there is, in fact, an enhanced spin moment on nearly all Fe atoms in this case.

V. CONCLUSIONS

We have studied the stability of monolayer Fe and graphene-embedded Fe through *ab initio* calculations. We find that the most stable configuration of monolayer Fe is the ferromagnetic triangular lattice with a lattice constant of 2.44 Å. This is in contrast to experimental results of graphene-embedded Fe, which shows that these structures have a square lattice configuration with a bond length of 2.65 Å. However, we find that the square lattice configuration has a lower edge formation energy. This means that, during formation, it might be favorable to form the square lattice and the structure could then be kinetically hindered from subsequently rearranging to the triangular lattice. Furthermore, we have compared the stability of the square and triangular Fe lattices in two different graphene antidot lattices. In the larger one of these, the square lattice is, in fact, more stable than the triangular lattice, with a mean Fe-Fe bond length of 2.7 Å. This result is in very close agreement with the experimental results. Our results show that only a few Fe atoms in the graphene antidots are sufficient to give rise to magnetic moments, which are comparable to the magnetic moment of monolayer Fe.

ACKNOWLEDGMENTS

The authors gratefully acknowledge the financial support from the Center for Nanostructured Graphene (Project No. DNRF58) financed by the Danish National Research Foundation and from the QUSCOPE project financed by the Villum Foundation.

[1] L. Wang, I. Meric, P. Y. Huang, Q. Gao, Y. Gao, H. Tran, T. Taniguchi, K. Watanabe, L. M. Campos, D. A. Muller, J. Guo, P. Kim, J. Hone, K. L. Shepard, and C. R. Dean, Science **342**, 614 (2013).

[2] W. Han, R. K. Kawakami, M. Gmitra, and J. Fabian, Nat. Nanotechnol. **9**, 794 (2014).

[3] M. H. D. Guimarães, P. J. Zomer, J. Ingla-Aynés, J. C. Brant, N. Tombros, and B. J. van Wees, Phys. Rev. Lett. **113**, 086602 (2014).

[4] M. Drögeler, F. Volmer, M. Wolter, B. Terrés, K. Watanabe, T. Taniguchi, G. Güntherodt, C. Stampfer, and B. Beschoten, Nano Lett. **14**, 6050 (2014).

[5] N. Tombros, C. Jozsa, M. Popinciuc, H. T. Jonkman, and B. J. Van Wees, Nature (London) **448**, 571 (2007).

[6] M. Weser, E. N. Voloshina, K. Horn, and Y. S. Dedkov, Phys. Chem. Chem. Phys. **13**, 7534 (2011).

[7] J. Zhou, Q. Wang, Q. Sun, X. Chen, Y. Kawazoe, and P. Jena, Nano Lett. **9**, 3867 (2009).

[8] P. O. Lehtinen, A. S. Foster, Y. Ma, A. V. Krasheninnikov, and R. M. Nieminen, Phys. Rev. Lett. **93**, 187202 (2004).

[9] S. Haldar, B. S. Pujari, S. Bhandary, F. Cossu, O. Eriksson, D. G. Kanhere, and B. Sanyal, Phys. Rev. B **89**, 205411 (2014).

[10] I. Zanella, S. B. Fagan, R. Mota, and A. Fazzio, J. Phys. Chem. C **112**, 9163 (2008).

[11] A. V. Krasheninnikov, P. O. Lehtinen, A. S. Foster, P. Pyykkö, and R. M. Nieminen, Phys. Rev. Lett. **102**, 126807 (2009).

[12] E. J. G. Santos, A. Ayuela, and D. Sánchez-Portal, New J. Phys. **12**, 053012 (2010).

[13] Z. He, K. He, A. W. Robertson, A. I. Kirkland, D. Kim, J. Ihm, E. Yoon, G.-D. Lee, and J. H. Warner, Nano Lett. **14**, 3766 (2014).

[14] J. A. Rodrígues-Manzo, O. Cretu, and F. Banhart, ACS Nano **4**, 3422 (2010).

[15] S. B. Fagan, R. Mota, A. J. R. da Silva, and A. Fazzio, Phys. Rev. B **67**, 205414 (2003).

[16] A. W. Robertson, B. Montanari, K. He, J. Kim, C. S. Allen, Y. A. Wu, J. Olivier, J. Neethling, N. Harrison, A. I. Kirkland, and J. H. Warner, Nano Lett. **13**, 1468 (2013).

[17] J. Zhao, Q. Deng, A. Bachmatiuk, G. Sandeep, A. Popov, J. Eckert, and M. H. Rümmeli, Science **343**, 1228 (2014).

[18] J. Eroms and D. Weiss, New J. Phys. **11**, 095021 (2009).

[19] A. J. M. Giesbers, E. C. Peters, M. Burghard, and K. Kern, Phys. Rev. B **86**, 045445 (2012).

[20] T. G. Pedersen, C. Flindt, J. G. Pedersen, N. A. Mortensen, A.-P. Jauho, and K. Pedersen, Phys. Rev. Lett. **100**, 136804 (2008).

[21] S. J. Brun, M. R. Thomsen, and T. G. Pedersen, J. Phys.: Condens. Matter **26**, 265301 (2014).

[22] T. G. Pedersen and J. G. Pedersen, J. Appl. Phys. **112**, 113715 (2012).
[23] M. R. Thomsen, S. J. Brun, and T. G. Pedersen, J. Phys.: Condens. Matter **26**, 335301 (2014).
[24] J. G. Pedersen, T. Gunst, T. Markussen, and T. G. Pedersen, Phys. Rev. B **86**, 245410 (2012).
[25] X. Gonze, J.-M. Beuken, R. Caracas, F. Detraux, M. Fuchs, G.-M. Rignanese, L. Sindic, M. Verstraete, G. Zerah, F. Jollet, M. Torrent, A. Roy, M. Mikami, Ph. Ghosez, J.-Y. Raty, and D. C. Allan, Comp. Mater. Sci. **25**, 478 (2002).
[26] X. Gonze, B. Amadon, P.-M. Anglade, J.-M. Beuken, F. Bottin, P. Boulanger, F. Bruneval, D. Caliste, R. Caracas, M. Côté, T. Deutsch, L. Genovese, Ph. Ghosez, M. Giantomassi, S. Goedecker, D. R. Hamann, P. Hermet, F. Jollet, G. Jomard, S. Leroux, M. Mancini, S. Mazevet, M. J. T. Oliveira, G. Onida, Y. Pouillon, T. Rangel, G.-M. Rignanese, D. Sangalli, R. Shaltaf, M. Torrent, M. J. Verstraete, G. Zerah, and J. W. Zwanziger, Comput. Phys. Commun. **180**, 2582 (2009).
[27] F. Bottin, S. Leroux, A. Knyazev, and G. Zérah, Comp. Mater. Sci. **42**, 329 (2008).
[28] M. Torrent, F. Jollet, F. Bottin, G. Zérah, and X. Gonze, Comp. Mater. Sci. **42**, 337 (2008).
[29] J. P. Perdew, K. Burke, and M. Ernzerhof, Phys. Rev. Lett. **77**, 3865 (1996).
[30] G. Kresse and D. Joubert, Phys. Rev. B **59**, 1758 (1999).
[31] G. Kresse, W. Bergermayer, and R. Podloucky, Phys. Rev. B **66**, 146401 (2002).
[32] S. Blügel, B. Drittler, R. Zeller, and P. Dederichs, Appl. Phys. A **49**, 547 (1989).
[33] *CRC Handbook of Chemistry and Physics*, 95th ed., edited by W. M. Haynes (CRC Press, Boca Raton, Florida, USA, 2014).
[34] J. C. Boettger, Phys. Rev. B **47**, 1138 (1993).
[35] S. Achilli, S. Caravati, and M. I. Trioni, J. Phys.: Condens. Matter **19**, 305021 (2007).
[36] M. L. Trolle, U. S. Møller, and T. G. Pedersen, Phys. Rev. B **88**, 195418 (2013).

Paper IV

Intense and tunable second-harmonic generation in biased bilayer graphene

Søren Jacob Brun and Thomas Garm Pedersen

The paper has been published in
Physical Review B **91**, 205405 (2015)

Intense and tunable second-harmonic generation in biased bilayer graphene

Søren J. Brun and Thomas G. Pedersen
Department of Physics and Nanotechnology, Aalborg University, DK-9220 Aalborg Øst, Denmark
and Center for Nanostructured Graphene (CNG), DK-9220 Aalborg Øst, Denmark
(Received 2 February 2015; revised manuscript received 20 April 2015; published 8 May 2015)

The centrosymmetric two-dimensional material bilayer graphene (BLG) does not show dipole-allowed second-harmonic generation (SHG) in its pristine form. However, the symmetry can be broken by applying an electric field perpendicular to the layer. Here, we present a theoretical study of SHG from biased BLG. We show that the sheet second-harmonic susceptibility reaches very large values of several hundred nm^2/V in the midinfrared region. The SHG is tunable depending on the strength of the electric field. Furthermore, a strong, tunable double resonance appears in the spectrum. We believe that this study could spark interest in the nonlinear optical properties of biased BLG.

DOI: 10.1103/PhysRevB.91.205405 PACS number(s): 42.65.An, 78.20.−e

I. INTRODUCTION

Since the synthesis of graphene in 2004 [1], two-dimensional (2D) materials have attracted tremendous interest. Graphene has been studied widely due to its remarkable electronic [2,3] and optical properties [4]. However, the semimetallic nature of graphene limits its applicability for semiconductor devices. Several methods for creating a band gap are being pursued, including graphene nanoribbons [5–7], periodic gating [8], and graphene antidot lattices [9]. Another promising method is to use biased bilayer graphene (BLG), for which it has been shown both theoretically [10–12] and experimentally [11–15] that it is possible to obtain band gaps of a few hundred meV. In order to create a band gap, an electric field is applied perpendicularly to the graphene plane. This breaks the sublattice symmetry, which induces a tunable band gap depending on the strength of the electric field. The band gap has been measured by several groups, and has shown values up to 250 meV [14]. The linear optical properties of BLG have been studied theoretically by Abergel and Fal'ko [16] by including the strongest interlayer coupling γ_1 in a tight-binding (TB) model. Unlike monolayer graphene, in which the conductivity has a constant value of $\sigma_0 = e^2/4\hbar$ for a broad range of energies [4], the conductivity of BLG shows distinct features at low energies related to the interlayer coupling strength. A particular feature at an energy equal to γ_1 was observed. Nicol and Carbotte [17] included the influence of the chemical potential and a perpendicular electric field in their study. For a chemical potential $\mu \neq 0$, the feature at γ_1 splits in two. For a nonvanishing bias, a semiconducting gap appears in the conductivity for $\mu = 0$. The linear response is thus greatly affected by changes in the bias and chemical potential. Doped BLG was studied experimentally by Kuzmenko *et al.* [18,19] using infrared spectroscopy and compared with a TB model, where skew coupling parameters are included. This showed good agreement, and enabled them to determine the TB parameters of BLG. Furthermore, they report evidence of a gate-induced band gap.

Second-harmonic generation (SHG) has been demonstrated in the 2D materials MoS_2, WS_2, and WSe_2, where it has been used to identify crystal lattice orientation and grain boundaries in a polycrystalline sample [20–25]. This shows that SHG may act as a useful noninvasive characterization method for atomically thin samples. SHG has also been measured from 2D metallic quantum wells having thicknesses ranging from a few to several tens of monolayers and compared with theory, which showed good agreement [26]. Furthermore, SHG in MoS_2 has been calculated and compared to experiments with reasonable agreement [27]. One-dimensional structures such as carbon nanotubes have also been studied theoretically, where the SHG was shown to depend strongly on diameter and chirality [28]. Dipole-allowed even order optical processes require materials that are noncentrosymmetric. Monolayer graphene has inversion symmetry, meaning that it does not show any dipole-allowed SHG. However, it has been shown theoretically that graphene shows SHG when the valley symmetry is broken [29]. Furthermore, SHG from graphene at oblique incidence of radiation has been studied theoretically, showing large values when compared with typical 2D semiconductor structures [30]. Graphene at oblique incidence of radiation has also been studied experimentally, which shows SHG with fourfold symmetry when rotated around the surface normal due to quadrupole optical transitions [31,32]. Taking into account the photon momentum transfer to electron system, it has been demonstrated theoretically that SHG from graphene using linearly polarized light can be strongly circularly polarized [33]. Strong third-harmonic generation (THG) has been measured from monolayer graphene, and it was reported that the SHG from the same sample was two orders of magnitude lower than the THG [34].

Pristine BLG is centrosymmetric, having an inversion point at the midpoint between the layers (cf. the inset in Fig. 1), which means that it will not show strong SHG unless the symmetry of the material is broken, which may be achieved by applying a perpendicular electric field. The nonlinear optical properties of BLG have only been studied to a limited extent. In the low-energy regime, BLG has been shown theoretically to display efficient high harmonic generation [35]. Using a Dirac model description, Wu *et al.* [36] have shown that BLG will show SHG when an in-plane current is included in order to break the symmetry and thereby enable SHG from the material. In their paper, they reported very large and tunable second-harmonic (SH) susceptibilities. They also found that the SH susceptibility is zero when omitting the in-plane current, and argue that the contributions from opposite momenta (K and K' valleys) cancel. In the present paper, we

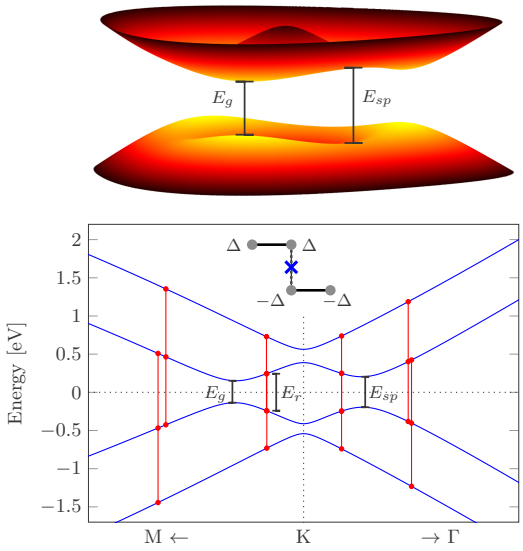

FIG. 1. (Color online) Band structure of biased BLG near the K point for $\Delta = 0.4$ eV. The top part shows the energy surfaces of the top valence band and bottom conduction band near the K point. The bottom part shows the band structure (blue), where double-resonance transitions are shown (red). The inset shows the four-atom unit cell of BLG with shifted on-site potentials. The blue cross marks the inversion point when the electric field is zero.

show analytically that this is indeed the case, but only within the Dirac model. In the full TB model, the K, K' contributions do not cancel, provided a perpendicular electric field is applied. The band gap of BLG can be tuned by varying the applied field, which also affects the SHG as the band structure changes. The band gap reaches values in the midinfrared (MIR) region, where few materials have a strong nonlinear response, thus making BLG a promising platform for nonlinear optical applications.

In this paper, we calculate the SHG in biased BLG using a nearest-neighbor TB model based on the Slonczewski-Weiss-McClure (SWMc) parametrization of graphite [12,37]. For simplicity, we include only the interband contribution to the SH susceptibility. Furthermore, we restrict our analysis to the in-plane response only. The SH response is calculated for different values of the applied bias, which is found to significantly alter the spectrum. We find that the SH susceptibility is nonzero when the perpendicular electric field is nonvanishing. The SH response reaches very large values in the MIR, and a strong double resonance appears at a tunable photon energy depending on the applied electric field. Additionally, we study graphene on hexagonal boron nitride (G/hBN) as an alternative way of breaking the symmetry of graphene. We find that G/hBN shows SHG, although the strength is much weaker than for biased BLG. Finally, we employ an integration method for nonlinear response functions based on the improved triangle method [38]. This method provides convergence at a much lower k-point sampling, especially near double-resonance transition energies.

II. THEORY AND METHODS

The electronic properties of BLG are well described by a simple TB approach. The band structure of biased BLG has been measured using angle-resolved photoemission spectroscopy, where TB was shown to accurately describe the low-energy properties [13]. In this paper, we employ TB with the SWMc parametrization developed for graphite [12,37]. The Hamiltonian for biased BLG may then be expressed as

$$\mathbf{H} = \begin{pmatrix} -\Delta - \frac{\Delta'}{2} & -\gamma_0 f(\mathbf{k}) & \gamma_4 f(\mathbf{k}) & -\gamma_3 f^*(\mathbf{k}) \\ -\gamma_0 f^*(\mathbf{k}) & -\Delta + \frac{\Delta'}{2} & \gamma_1 & \gamma_4 f(\mathbf{k}) \\ \gamma_4 f^*(\mathbf{k}) & \gamma_1 & \Delta + \frac{\Delta'}{2} & -\gamma_0 f(\mathbf{k}) \\ -\gamma_3 f(\mathbf{k}) & \gamma_4 f^*(\mathbf{k}) & -\gamma_0 f^*(\mathbf{k}) & \Delta - \frac{\Delta'}{2} \end{pmatrix}, \tag{1}$$

where $f(\mathbf{k}) = \exp(ik_x \frac{a}{\sqrt{3}}) + 2\exp(-ik_x \frac{a}{2\sqrt{3}})\cos(k_y \frac{a}{2})$ and $a = 2.46$ Å is the graphene lattice constant. The effect of the bias is incorporated by shifting the on-site potentials of the two layers by $\pm\Delta$. The inset in Fig. 1 shows the four-atom unit cell of BLG with the shifted on-site potentials. The structure is clearly centrosymmetric for $\Delta = 0$ with the inversion point at the blue cross, however, for $\Delta \neq 0$ the centrosymmetry is broken. The SWMc TB parameters for BLG used in our calculations are shown in Table I [37]. Here, γ_0 is the in-plane hopping parameter, γ_1 is the hopping parameter between atoms stacked directly on top of one another, while γ_3 and γ_4 are skew interlayer hopping parameters. Δ' is the difference in on-site potential between atoms stacked on top of each other and atoms above and below hexagon centers.

In order to calculate the SHG, we employ the independent-particle approximation and consider first the limit of low temperatures. The expression for the imaginary part of the sheet SH susceptibility is then [27,28]

$$\chi^{(2)\,\prime\prime}_{abc}(\omega) = \frac{e^3}{2\pi m_e^3 \hbar^2 \omega^3} \sum_{c,v,l} \int \left[\frac{P_{vcl}}{\omega - \omega_{lv}} \delta(2\omega - \omega_{cv}) + \left(\frac{P_{vlc}}{\omega + \omega_{cl}} + \frac{P_{clv}}{\omega + \omega_{lv}} \right) \delta(\omega - \omega_{cv}) \right] d^2k, \tag{2}$$

where $P_{ijl} = \mathrm{Im}\{p^a_{ij}(p^b_{jl}p^c_{li} + p^c_{jl}p^b_{li})\}/2$, p^a_{ij} is the a component of the momentum matrix element between states i and j, and $\omega_{ij} = \omega_i - \omega_j$. The momentum matrix elements are given by $p^a_{ij} = \mathbf{v}_i^\dagger \mathbf{P_a} \mathbf{v}_j$, where $\mathbf{P_a} = \frac{m}{\hbar}\frac{\partial \mathbf{H}}{\partial k_a}$ is the momentum matrix in the a direction and $\mathbf{v}_i$ is the ith eigenvector. The indices of the sum are restricted such that c runs over all conduction bands, v runs over all valence bands, and $l \neq (c,v)$. If the

TABLE I. TB parameters used for BLG in units of eV.

γ_0	γ_1	γ_3	γ_4	Δ'
3.16	0.381	0.38	0.14	0.022

temperature is nonvanishing, the response function becomes

$$\chi^{(2)\prime\prime}_{abc}(\omega) = \frac{e^3}{2\pi m_e^3 \hbar^2 \omega^3} \sum_{c,v,l} \int \left[\left(\frac{f_{vl} P_{vcl}}{\omega - \omega_{lv}} + \frac{f_{cl} P_{vcl}}{\omega - \omega_{cl}} \right) \delta(2\omega - \omega_{cv}) + \left(\frac{f_{vc} P_{vlc}}{\omega + \omega_{cl}} + \frac{f_{vc} P_{clv}}{\omega + \omega_{lv}} \right) \delta(\omega - \omega_{cv}) \right] d^2k, \quad (3)$$

where $f_{ij} = f_i - f_j$ and f_i is the Fermi occupation factor of state i. An important difference is that the band indices v and c are now unrestricted. All calculations are carried out in the low-temperature limit unless stated otherwise. From symmetry the only nonvanishing elements of the SH tensor are $\chi^{(2)}_{xxx} = -\chi^{(2)}_{xyy} = -\chi^{(2)}_{yyx} = -\chi^{(2)}_{yxy} \equiv \chi^{(2)}$. Note that we consider only the in-plane response of the system. The real part of the SH susceptibility is calculated by Kramers-Kronig transformation. Broadening of the spectra is introduced by convolving with a Lorentzian.

We begin by addressing the finding by Wu *et al.* that the SHG is vanishing when using the Dirac model unless an in-plane current is included. In their paper, they include nearest-neighbor interlayer coupling, such that the Dirac Hamiltonian is

$$\mathbf{H} = \begin{pmatrix} -\Delta & q_- & 0 & 0 \\ q_+ & -\Delta & \gamma_1 & 0 \\ 0 & \gamma_1 & \Delta & q_- \\ 0 & 0 & q_+ & \Delta \end{pmatrix}, \quad (4)$$

where $q_\pm = \hbar v_F (q_x \pm \xi i q_y)$ and $q_{x/y} = k_{x/y} - K_{x/y}$. The parameter ξ determines the K valley ($\xi = +1$ for K and $\xi = -1$ for K'). Changing from K to K' thus corresponds to a complex conjugation of the Hamiltonian, and consequently the eigenvectors are conjugated. We consider the SH tensor element $\chi^{(2)}_{xxx}$, which means that the momentum matrix elements needed are of the type p^x_{ij}. As $\mathbf{P_x}$ is unchanged when conjugated, changing from K to K' entails a complex conjugation of p^x_{ij}, leading to $P_{ijl}(K') = \mathrm{Im}\{(p^x_{ij})^*(p^x_{jl})^*(p^x_{li})^*\} = -P_{ijl}(K)$. This is valid not only at the K, K' points, but for all k points belonging to the K, K' valleys. Contributions to the SH susceptibility from the K valley are thus canceled by contributions from the K' valley. In the TB model used in this paper, the Hamiltonian becomes complex conjugated when changing the k point from $\mathbf{k}$ to $-\mathbf{k}$. However, this does not lead to a complex conjugation of the momentum matrix. Therefore, the analysis from the Dirac model does not apply, and the contributions do not cancel in the TB model.

Other models including, e.g., exciton effects and spin-orbit coupling have also been used for 2D materials such as MoS_2. We neglect spin-orbit coupling, as this effect is very weak in graphene [39]. Exciton effects are also omitted, meaning that the computational effort needed for the calculations is significantly lowered. This enables a more thorough analysis of the effects of the bias as well as other parameters. Moreover, it has been shown that the SH response increases when exciton effects are included [27].

It is well known that applying an electric field perpendicular to BLG opens up a band gap that depends on the magnitude of the electric field [10–15]. The band structure near the K point calculated using the Hamiltonian in Eq. (1) is shown in Fig. 1, where the shift of the on-site potentials has been set to $\Delta = 0.4$ eV. Experimentally, electric fields up to 3 V/nm, corresponding to $\Delta = 0.5$ eV, have been obtained [14]. The top part of the figure shows the energy surfaces of the top valence band and bottom conduction band near the K point, where the band gap E_g and saddle point transition energy E_{sp} are illustrated. The band structure is shown in the bottom part. Here, the red lines show double resonances in the band structure, which occur at fundamental photon energies E_r where $\omega = \omega_{lv}$ and $2\omega = \omega_{cv}$ are fulfilled simultaneously. Double-resonance transitions generally appear at two energies for biased BLG, in this case at 0.49 and 0.87 eV.

The behavior of the double resonances may be described by considering the simple Dirac model given by Eq. (4). The eigenvalues of this Hamiltonian are

$$E = \pm \frac{1}{\sqrt{2}} \sqrt{2\Delta^2 + \gamma_1^2 + 2q^2 \pm \sqrt{16\Delta^2 q^2 + \gamma_1^4 + 4\gamma_1^2 q^2}}, \quad (5)$$

where $q^2 = \hbar^2 v_F^2 (q_x^2 + q_y^2)$. The four bands are sorted such that $E_1 < E_2 < E_3 < E_4$, meaning that the resonance condition becomes $E_3 - E_2 = E_2 - E_1$. Solving this for the q closest to the K point leads to

$$q = \frac{1}{4\sqrt{2}} \sqrt{68\Delta^2 + 9\gamma_1^2 - 5\sqrt{144\Delta^4 + 8\Delta^2\gamma_1^2 + 9\gamma_1^4}}, \quad (6)$$

which is only real when $\Delta \geqslant \gamma_1/\sqrt{8} \simeq 0.135$ eV. Using this value of Δ, the photon energy at which the resonance appears becomes $E_{r,\min} = E_2 - E_1 = \gamma_1/\sqrt{2} \simeq 0.269$ eV.

The integral in Eq. (2) may be calculated numerically using the improved triangle method described in Ref. [38]. For numerical reasons, broadening is introduced through $\hbar\omega \to \hbar\omega + i\Gamma$, where Γ should be small. In the full TB model, the response is generally not divergent at the double resonance except at a few specific energies and is well behaved otherwise. However, as Γ decreases, the integral requires a huge amount of k points for the results to be converged at photon energies near the double resonances. The reason for the slow convergence is that the linearization used in the triangle method becomes inaccurate near the double resonances. We have developed a modified triangle method for nonlinear response functions, in which both the numerator and denominator in the integral are linearized (see the Appendix for the derivation). This method provides converged results at the double resonances without any broadening and at much lower k-point sampling.

III. RESULTS

The SH susceptibility of BLG for selected values of Δ is shown in Fig. 2. The gray dotted lines are located at the energies of $E_g/2$, $E_{sp}/2$, E_g, E_{sp}, and E_r, where special features in the spectra are observed. The SH susceptibility always changes abruptly at $E_g/2$ and E_g, and has van Hove singularities at $E_{sp}/2$ and E_{sp}. It is seen that the susceptibility reaches very large values exceeding 1000 nm^2/V for low values of Δ, and several hundred nm^2/V at larger values. Such large values are located at photon energies just above

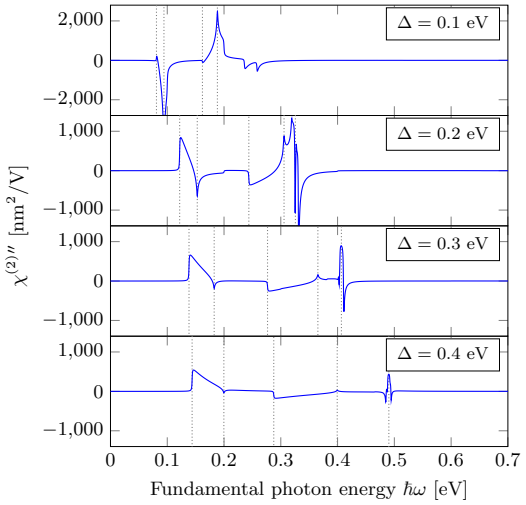

FIG. 2. (Color online) Sheet SH susceptibility of BLG for different values of Δ. The gray dotted lines correspond to (from left to right) $E_g/2$, $E_{sp}/2$, E_g, E_{sp}, and E_r. All spectra have been broadened by 1 meV.

$E_g/2$ and at the double resonance. The first double resonance (the one at the lowest photon energy) shows up very clearly in the three bottom panels. However, no significant features in the spectra are observed at the second resonance. The first resonance is observed in all panels, except for $\Delta = 0.1$ eV, which is in agreement with the condition derived in Sec. II that $\Delta \geqslant 0.135$ eV is required for the double resonance to appear. Additionally, the resonance is seen to shift to higher energies as Δ increases, while the overall amplitude of the susceptibility decreases.

The TB description of BLG is often approximated by only including the nearest-neighbor in-plane coupling γ_0 and the strongest interlayer coupling γ_1 [10,11,15]. By including the other interlayer coupling parameters, the energy surface at low energies near the K point changes from the Mexican hat dispersion to one with three valence (conduction) band maxima (minima) and three saddle points as shown in Fig. 1. We have found (not shown) that approximating the Hamiltonian by omitting γ_3 and γ_4 from the calculations still produces a nonzero response, but this approximation is too crude for second-order nonlinear optical calculations, as we see notable changes in the SH susceptibility.

Figure 2 shows the SH susceptibility at selected values of Δ. The color plot in Fig. 3 shows the absolute value of the SH susceptibility for varying Δ and fundamental photon energy. At energies below half the band gap, no second-order transitions between valence and conduction bands are possible, and the imaginary part of the SH response is consequently zero in this region. At $E_g/2$, and again at E_g, the susceptibility increases abruptly to very large values, as observed in Fig. 2. The sharp features from the saddle point transition are also easily recognized. At larger energies, the double resonance appears clearly as a sharp line approaching $\Delta = \hbar\omega$. The response is observed to generally be much lower at large photon energies compared with the response at photon energies below ∼1 eV. From the plot, we note that the double resonance does not extend all the way down to $\Delta = 0$, but only appears at

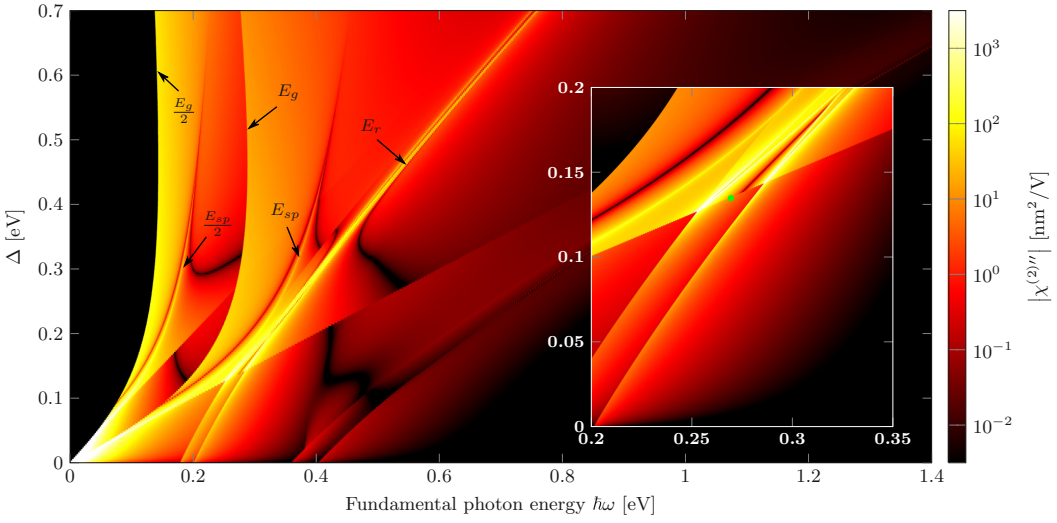

FIG. 3. (Color online) Absolute value of the imaginary part of the sheet SH susceptibility of biased BLG without broadening. The response is exactly zero at photon energies below $E_g/2$. Sharp features from band gap and saddle point transitions appear clearly in the plot. A double resonance appears as an approximately straight line approaching $\Delta = \hbar\omega$. The inset shows a zoom of the region where the double resonance appears. The green dot is at $(\hbar\omega, \Delta) = (\gamma_1/\sqrt{2}, \gamma_1/\sqrt{8})$, which is the analytical prediction of the onset of the double resonance. The color scale has been changed in the inset to enhance the contrast of the double resonance.

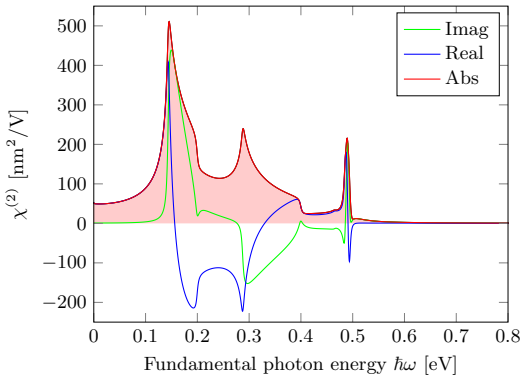

FIG. 4. (Color online) SHG in BLG with the on-site potentials of the two layers shifted by $\Delta = 0.4$ eV. The real part of the SH susceptibility is calculated from Kramers-Kronig transformation. The spectrum is broadened by 5 meV.

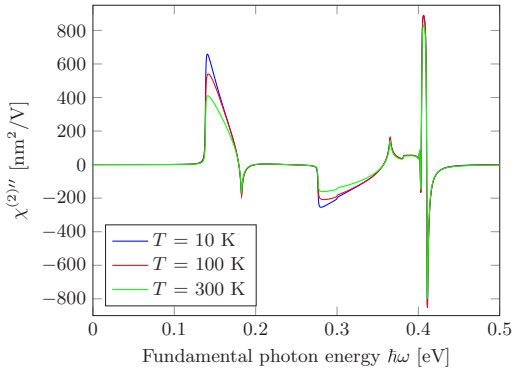

FIG. 5. (Color online) SH susceptibility for $\Delta = 0.3$ eV for different temperatures. The Fermi level is located 10 meV below the conduction band edge. For $T = 10$ K the spectrum is practically identical to the zero-temperature limit. All spectra are broadened by 1 meV.

values of Δ over a certain threshold. This is in accordance with the Dirac analysis in Sec. II, and the inset in Fig. 3 shows a zoom of the region where the resonance appears. The green dot marks the analytical prediction of the onset of the resonance. In this region, the resonance splits in two, and the analytical expression of the onset is seen to be in excellent agreement with the full TB results, as it lies almost perfectly between the onsets of the two branches. From the inset it is also evident that the SH response vanishes as Δ approaches zero, which is expected as the system becomes centrosymmetric in this limit. The results in Fig. 3 clearly show that biased BLG has strong SHG that is tunable by the applied electric field.

The results in Fig. 2 show the imaginary part of the SH susceptibility. The real part may be found by Kramers-Kronig transformation of the spectrum. Figure 4 shows the SHG of BLG with $\Delta = 0.4$ eV where the absolute value of the SH susceptibility is also shown. The spectrum has been broadened by 5 meV. Again, the SHG is seen to reach values of several hundred nm^2/V, and a sharp feature from the double resonance shows up clearly in the spectrum near a photon energy of 0.5 eV.

Next, we study the influence of temperature by calculating the SH susceptibility using Eq. (3). We do this for a fixed electric field given by $\Delta = 0.3$ eV and vary the temperature from zero to room temperature. If the Fermi level is located in the middle of the band gap, the spectrum is nearly unchanged even at high temperatures. The calculated band gap is 276 meV, meaning that the occupancy is only changed slightly even at room temperature. By placing the Fermi level closer to the conduction or valence band, the response becomes more sensitive to temperature changes. Figure 5 shows the temperature dependence of the SH susceptibility for a Fermi level located 10 meV below the conduction band edge. The curve for $T = 10$ K is practically identical to the case of zero temperature. The spectrum changes as the temperature increases, and the features related to the band edge transitions become less dominant, which is expected as this is where the change in occupancy is most significant. However, the double resonance is related to states at energies further away from the Fermi level, and therefore only minor changes are observed in this part of the spectrum.

As demonstrated above, the optical properties are sensitive to the Fermi level of the system. At Fermi levels intersecting bands in the band structure, the allowed transitions between valence and conduction bands are changed locally (near the K and K' points) due to the Pauli principle, thus changing the optical spectrum. Figure 6 shows examples of the SH susceptibility at different Fermi levels, where the shift of the on-site potentials has again been set to $\Delta = 0.3$ eV. Again, the band gap is 276 meV, meaning that a Fermi level of ± 138 meV will be at the edge of the valence or conduction band. From the figure it is seen that increasing the Fermi level to 0.15 eV only marginally changes the spectrum. The spectrum is only affected in regions caused by transitions near the band gap, i.e., at photon energies just above $E_g/2$ and E_g. However, increasing the Fermi level to 0.2 eV significantly reduces the response, and although the resonance remains, its amplitude is also reduced. Note that the scale bars in the two bottom panels are different from the two top panels. At a Fermi level of 0.25 eV, the response is even lower, and basically no features of the original spectrum remain. The reason for this significant reduction in the response is that when the Fermi level is changed, the occupation at the valence or conduction band edge is changed, and indeed contributions from transitions near the band edges are causing the very high susceptibility.

The absolute value of the zero-temperature SH susceptibility for varying Fermi levels and photon energies is shown in Fig. 7. As expected, the spectrum remains unchanged when the Fermi level is within $\pm E_g/2$. However, as the Fermi level moves into the valence or conduction band, the amplitude of the SH susceptibility is seen to rapidly decrease, although it still displays values of a few nm^2/V. Furthermore, the expected Pauli blockades at slopes of $\pm 1/2$ and ± 1 are observed in the plot. This shows that in order for biased BLG to show strong SHG, the Fermi level should be in the band gap region.

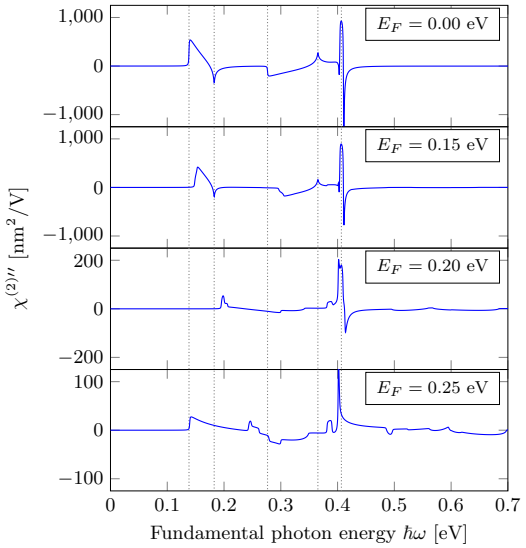

FIG. 6. (Color online) Sheet SH susceptibility of biased BLG using $\Delta = 0.3$ eV for different values of the Fermi level. The gray dotted lines are (from left to right) $E_g/2$, $E_{sp}/2$, E_g, E_{sp}, and E_r of BLG using $\Delta = 0.3$ eV and $E_F = 0$ eV. The spectra are broadened by 1 meV.

An alternative way of breaking the symmetry in a graphene system is by AB stacking a single layer of graphene on top of a single layer of hexagonal boron nitride, forming graphene on hexagonal boron nitride (G/hBN). This creates sublattice

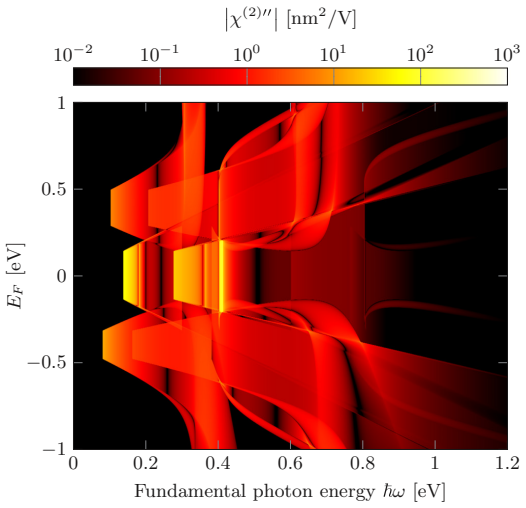

FIG. 7. (Color online) Absolute value of the imaginary part of the sheet SH susceptibility of biased BLG for different Fermi levels using $\Delta = 0.3$ eV. The calculations are made without broadening.

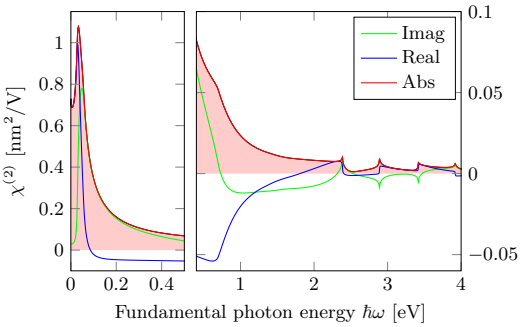

FIG. 8. (Color online) SHG in G/hBN with a broadening of 5 meV. The left part shows the relatively large values at energies close to the band gap while the right part shows the spectrum at larger photon energies.

asymmetry in graphene, making SHG possible. Additionally, a band gap opens up, which has a theoretical value of 53 meV and an experimental value of 31 meV [40,41]. We calculate the SHG from G/hBN using the TB parameters from Ref. [42]. This parametrization only includes the strongest interlayer coupling γ_1. However, we have seen that neglecting the skew coupling parameters strongly affects the SHG, as the system becomes more symmetric. Therefore, we also include the skew coupling parameters from BLG, which should be a good approximation as the two systems are closely related. The SHG from G/hBN is shown in Fig. 8. The left part shows the response at low photon energies, where a peak is observed close to the band gap of the material reaching a value slightly larger than 1 nm^2/V. The right part shows the response at larger photon energies, where the values are much lower than at low photon energies, and only reaches values around 0.01 nm^2/V. This means that G/hBN will show SHG, although the values of the SH susceptibility are orders of magnitude lower than that of biased BLG. The present results demonstrate that SHG can be an excellent probe of the electronic structure of carbon-based 2D materials, similarly to previous studies of metallic 2D materials [26].

IV. CONCLUSION

In this paper, we have presented a theoretical study of SHG from biased BLG using nearest-neighbor TB. When the centrosymmetry is broken by applying a perpendicular electric field, BLG shows a SH response which is tunable by the strength of the electric field. The SH susceptibility reaches very large values, typically several hundred nm^2/V, in the MIR region where few materials show intense SHG. A strong and tunable resonance appears above a certain threshold of the electric field. An analytical estimate of the threshold was shown to be in excellent agreement with the full TB calculations. The SH response is strongly reduced when the Fermi level is moved into the valence or conduction band, although still showing values of a few nm^2/V. We also studied graphene on hexagonal boron nitride, which is another approach to breaking the symmetry of graphene and enabling

SHG. This showed low values of the SH susceptibility at large photon energies and a response around 1 nm^2/V at very low energies, meaning that the response is around two orders of magnitude lower than biased BLG. Additionally, a different triangle integration method capable of handling nonlinear response functions was developed. Due to the very large and tunable SH susceptibility of biased BLG, which also shows a strongly resonant behavior, we believe that this could encourage experimental work on different nonlinear optical graphene-based devices.

ACKNOWLEDGMENTS

The authors gratefully acknowledge the financial support from the Center for Nanostructured Graphene (Project No. DNRF58) financed by the Danish National Research Foundation and from the QUSCOPE project financed by the Villum Foundation.

APPENDIX: IMPROVED TRIANGLE METHOD FOR NONLINEAR RESPONSE FUNCTIONS

The improved triangle method [38] is useful when integration over a 2D Brillouin zone is required. This method relies on linearization of the k-dependent energies as well as the weight function. The method works well when the weight function is well behaved. However, it struggles to handle singularities in highly nonlinear weight functions. Here, we present a modified triangle method for integrating nonlinear response functions. We consider integrals with weight function F/G of the form

$$S(\omega) = \int \frac{F(\mathbf{k})}{G(\mathbf{k})}\delta(E_{cv}(\mathbf{k}) - \hbar\omega)d^2k = \sum_\Delta \int_\Delta \frac{F(\mathbf{k})}{G(\mathbf{k})}\delta(E_{cv}(\mathbf{k}) - \hbar\omega)d^2k = \sum_\Delta S_\Delta(\omega), \quad \text{(A1)}$$

where the integral is divided into a number of triangles denoted by "Δ." By linearizing $E_{cv}(\mathbf{k})$, the integral is rewritten as a line integral along l_Δ where $E_{cv}(\mathbf{k}) = \hbar\omega$, such that each contribution to the sum becomes

$$S_\Delta(\omega) \simeq \frac{1}{|\nabla_k E_{cv}|}\int_{l_\Delta} \frac{F(\mathbf{k})}{G(\mathbf{k})}dl. \quad \text{(A2)}$$

The functions F and G are then linearized along l_Δ, such that $F = F_a + \frac{l}{L}(F_b - F_a)$, where $F_a = F(\mathbf{k}_a)$, $F_b = F(\mathbf{k}_b)$, and L is the length of l_Δ. Important k points for the triangle method as well as the integration line l_Δ are shown in Fig. 9. $G(\mathbf{k})$ is linearized in the same way. The contribution then becomes

$$S_\Delta(\omega) = \frac{2A_\Delta C}{(G_b - G_a)^2}\Big[(F_b - F_a)(G_b - G_a) + (F_bG_a - F_aG_b)\ln\left(\left|\frac{G_a}{G_b}\right|\right)\Big], \quad \text{(A3)}$$

where A_Δ is the area of the triangle. We use the notation $E_i = E_{cv}(\mathbf{k}_i)$ and sort the energies such that $E_0 \leqslant E_1 \leqslant E_2$. The parameters F_a, F_b and C are given by

$$F_b = F_0 + (\hbar\omega - E_0)\frac{F_{20}}{E_{20}}, \quad \text{(A4)}$$

$$F_a = \begin{cases} F_0 + (\hbar\omega - E_0)\frac{F_{10}}{E_{10}}, & E_0 \leqslant \hbar\omega < E_1, \\ F_1 + (\hbar\omega - E_1)\frac{F_{21}}{E_{21}}, & E_1 \leqslant \hbar\omega < E_2, \end{cases} \quad \text{(A5)}$$

$$C = \begin{cases} \frac{\hbar\omega - E_0}{E_{20}E_{10}}, & E_0 \leqslant \hbar\omega < E_1, \\ \frac{E_2 - \hbar\omega}{E_{21}E_{20}}, & E_1 \leqslant \hbar\omega < E_2, \end{cases} \quad \text{(A6)}$$

where $E_{ij} = E_i - E_j$ and $F_{ij} = F_i - F_j$. The parameters for G are calculated similarly.

The effect of using this method is illustrated in Fig. 10, where the SH susceptibility of BLG has been calculated near a double resonance using the normal triangle method and our method. The top part shows the normal method, where a complex frequency $\hbar\omega \to \hbar\omega + i\Gamma$ is required for convergence. The spectra in the bottom part are calculated using the method with $\Gamma = 0$. The figure clearly shows that the method provides converged results using significantly fewer k points compared with the normal triangle method, which requires three orders of magnitude more k points for convergence.

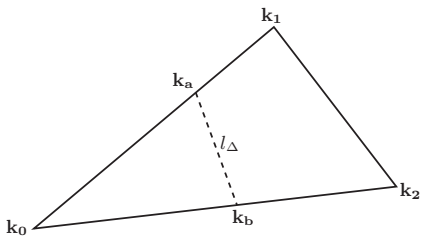

FIG. 9. Important k points for the triangle integration method.

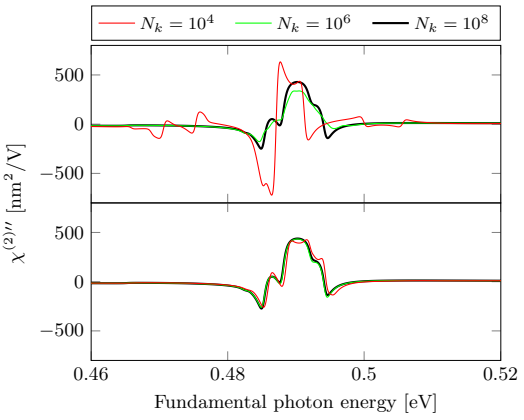

FIG. 10. (Color online) Convergence of the SH response near a double resonance for $\Delta = 0.4$ eV calculated using the normal triangle method (top) and our method (bottom). N_k denotes the total number of k points in the irreducible Brillouin zone. A complex frequency $\hbar\omega \to \hbar\omega + i\Gamma$ with $\Gamma = 0.1$ meV is used for the normal method. After integration, a broadening of 1 meV has been applied to both methods.

It is important to note that this method is only advantageous when the linearization in the regular triangle method is not a good approximation, i.e., near double resonances. In the remaining part of the spectrum, the two methods perform almost equally well. However, double resonances are handled much better using this method where broadening is not required and convergence is obtained using much lower k-point sampling.

[1] K. S. Novoselov, A. K. Geim, S. Morozov, D. Jiang, Y. Zhang, S. Dubonos, I. Grigorieva, and A. Firsov, Science **306**, 666 (2004).

[2] K. Novoselov, D. Jiang, F. Schedin, T. Booth, V. Khotkevich, S. Morozov, and A. Geim, Proc. Natl. Acad. Sci. U.S.A. **102**, 10451 (2005).

[3] K. I. Bolotin, K. Sikes, Z. Jiang, M. Klima, G. Fudenberg, J. Hone, P. Kim, and H. Stormer, Solid State Commun. **146**, 351 (2008).

[4] R. Nair, P. Blake, A. Grigorenko, K. Novoselov, T. Booth, T. Stauber, N. Peres, and A. Geim, Science **320**, 1308 (2008).

[5] B. Obradovic, R. Kotlyar, F. Heinz, P. Matagne, T. Rakshit, M. Giles, M. Stettler, and D. Nikonov, Appl. Phys. Lett. **88**, 142102 (2006).

[6] Y.-W. Son, M. L. Cohen, and S. G. Louie, Phys. Rev. Lett. **97**, 216803 (2006).

[7] M. Y. Han, B. zyilmaz, Y. Zhang, and P. Kim, Phys. Rev. Lett. **98**, 206805 (2007).

[8] J. G. Pedersen and T. G. Pedersen, Phys. Rev. B **85**, 235432 (2012).

[9] T. G. Pedersen, C. Flindt, J. Pedersen, N. A. Mortensen, A.-P. Jauho, and K. Pedersen, Phys. Rev. Lett. **100**, 136804 (2008).

[10] E. McCann, Phys. Rev. B **74**, 161403 (2006).

[11] E. V. Castro, K. Novoselov, S. Morozov, N. Peres, J. L. Dos Santos, J. Nilsson, F. Guinea, A. Geim, and A. C. Neto, Phys. Rev. Lett. **99**, 216802 (2007).

[12] L. Zhang, Z. Li, D. N. Basov, M. Fogler, Z. Hao, and M. C. Martin, Phys. Rev. B **78**, 235408 (2008).

[13] T. Ohta, A. Bostwick, T. Seyller, K. Horn, and E. Rotenberg, Science **313**, 951 (2006).

[14] Y. Zhang, T.-T. Tang, C. Girit, Z. Hao, M. C. Martin, A. Zettl, M. F. Crommie, Y. R. Shen, and F. Wang, Nature (London) **459**, 820 (2009).

[15] K. F. Mak, C. H. Lui, J. Shan, and T. F. Heinz, Phys. Rev. Lett. **102**, 256405 (2009).

[16] D. Abergel and V. I. Fal'ko, Phys. Rev. B **75**, 155430 (2007).

[17] E. Nicol and J. Carbotte, Phys. Rev. B **77**, 155409 (2008).

[18] A. Kuzmenko, E. Van Heumen, D. Van Der Marel, P. Lerch, P. Blake, K. Novoselov, and A. Geim, Phys. Rev. B **79**, 115441 (2009).

[19] A. Kuzmenko, I. Crassee, D. Van Der Marel, P. Blake, and K. Novoselov, Phys. Rev. B **80**, 165406 (2009).

[20] L. M. Malard, T. V. Alencar, A. P. M. Barboza, K. F. Mak, and A. M. de Paula, Phys. Rev. B **87**, 201401 (2013).

[21] N. Kumar, S. Najmaei, Q. Cui, F. Ceballos, P. M. Ajayan, J. Lou, and H. Zhao, Phys. Rev. B **87**, 161403 (2013).

[22] X. Yin, Z. Ye, D. A. Chenet, Y. Ye, K. O'Brien, J. C. Hone, and X. Zhang, Science **344**, 488 (2014).

[23] C. Janisch, Y. Wang, D. Ma, N. Mehta, A. L. Elías, N. Perea-López, M. Terrones, V. Crespi, and Z. Liu, Sci. Rep. **4**, 5530 (2014).

[24] H. Zeng, G.-B. Liu, J. Dai, Y. Yan, B. Zhu, R. He, L. Xie, S. Xu, X. Chen, W. Yao *et al.*, Sci. Rep. **3**, 1608 (2013).

[25] W.-T. Hsu, Z.-A. Zhao, L.-J. Li, C.-H. Chen, M.-H. Chiu, P.-S. Chang, Y.-C. Chou, and W.-H. Chang, ACS Nano **8**, 2951 (2014).

[26] T. G. Pedersen, K. Pedersen, and T. B. Kristensen, Phys. Rev. B **60**, R13997 (1999).

[27] M. L. Trolle, G. Seifert, and T. G. Pedersen, Phys. Rev. B **89**, 235410 (2014).

[28] T. G. Pedersen and K. Pedersen, Phys. Rev. B **79**, 035422 (2009).

[29] L. Golub and S. Tarasenko, Phys. Rev. B **90**, 201402 (2014).

[30] S. Mikhailov, Phys. Rev. B **84**, 045432 (2011).

[31] J. J. Dean and H. M. van Driel, Appl. Phys. Lett. **95**, 261910 (2009).

[32] M. Glazov and S. Ganichev, Phys. Rep. **535**, 101 (2014).

[33] M. Glazov, JETP Lett. **93**, 366 (2011).

[34] S.-Y. Hong, J. I. Dadap, N. Petrone, P.-C. Yeh, J. Hone, and R. M. Osgood, Jr., Phys. Rev. X **3**, 021014 (2013).

[35] H. Avetissian, G. Mkrtchian, K. Batrakov, S. Maksimenko, and A. Hoffmann, Phys. Rev. B **88**, 165411 (2013).

[36] S. Wu, L. Mao, A. M. Jones, W. Yao, C. Zhang, and X. Xu, Nano Lett. **12**, 2032 (2012).

[37] E. McCann and M. Koshino, Rep. Prog. Phys. **76**, 056503 (2013).

[38] T. G. Pedersen, C. Flindt, J. Pedersen, A.-P. Jauho, N. A. Mortensen, and K. Pedersen, Phys. Rev. B **77**, 245431 (2008).

[39] M. Gmitra, S. Konschuh, C. Ertler, C. Ambrosch-Draxl, and J. Fabian, Phys. Rev. B **80**, 235431 (2009).

[40] G. Giovannetti, P. A. Khomyakov, G. Brocks, P. J. Kelly, and J. van den Brink, Phys. Rev. B **76**, 073103 (2007).

[41] C. Woods, L. Britnell, A. Eckmann, R. Ma, J. Lu, H. Guo, X. Lin, G. Yu, Y. Cao, R. Gorbachev *et al.*, Nat. Phys. **10**, 451 (2014).

[42] J. Sławińska, I. Zasada, and Z. Klusek, Phys. Rev. B **81**, 155433 (2010).

Paper V

Boron and nitrogen doping in graphene antidot lattices

Søren Jacob Brun, Vitor Manuel Pereira and Thomas Garm Pedersen

The paper has been published in
Physical Review B **93**, 245420 (2016)

Boron and nitrogen doping in graphene antidot lattices

Søren J. Brun,[1,2] Vitor M. Pereira,[3] and Thomas G. Pedersen[1,2]
[1]*Department of Physics and Nanotechnology, Aalborg University, DK-9220 Aalborg Øst, Denmark*
[2]*Center for Nanostructured Graphene (CNG), DK-9220 Aalborg Øst, Denmark*
[3]*Centre for Advanced 2D Materials and Department of Physics, National University of Singapore, 2 Science Drive 3, 117542 Singapore*
(Received 9 February 2016; revised manuscript received 7 May 2016; published 20 June 2016)

Bottom-up fabrication of graphene antidot lattices (GALs) has previously yielded atomically precise structures with subnanometer periodicity. Focusing on this type of experimentally realized GAL, we perform density functional theory calculations on the pristine structure as well as GALs with edge carbon atoms substituted with boron or nitrogen. We show that *p*- and *n*-type doping levels emerge with activation energies that depend on the level of hydrogenation at the impurity. Furthermore, a tight-binding parametrization together with a Green's function method are used to describe more dilute doping. Finally, random configurations of impurities in moderately doped systems are considered to show that the doping properties are robust against disorder.

DOI: 10.1103/PhysRevB.93.245420

I. INTRODUCTION

Since its discovery [1], graphene has shown many interesting properties such as ultrahigh electron mobility [1–3], high transparency [4], and record-breaking mechanical strength [5]. However, one major drawback is the lack of a band gap, which is required for obtaining high on/off ratios in field-effect transistors [6]. Therefore, immense effort has been put into turning graphene into a semiconductor while preserving as much as possible its intrinsic characteristics. A popular method is dimensional narrowing, forming graphene nanoribbons (GNRs), which has been shown to introduce a tunable band gap dependent on the width and chirality [7–9]. Another promising and widely studied method is to periodically alter graphene in two dimensions. Hydrogen adsorption onto graphene on an iridium surface has been shown experimentally to create a periodic pattern and open a band gap [10]. Periodic gating has been studied as well, but was found to not open a band gap large enough for practical applications [11]. Finally, graphene antidot lattices (GALs) can be defined by means of periodic two-dimensional patterning in the form of perforations, which opens a widely tunable band gap depending on the geometry, characteristic dimensions, and chirality that define each element (unit cell) of these superlattices [12].

The above-mentioned methods for opening a band gap have been studied experimentally to a great extent using top-down methods [13–18]. However, fabricating GNRs along this route can lead to scattering from edge imperfections, which has been shown to degrade the transport properties [19,20]. GNRs may also be fabricated by unzipping carbon nanotubes which leads to much more regular edges [21,22]. Electron-beam lithography has been utilized to create GALs with periods down to a few dozen nanometers, and experimentally determined gaps as high as 102 meV have been reported [16]. However, GALs suffer from the same problems as GNRs when fabricated using top-down methods. The structures lack full periodicity and imperfections lead to scattering. Calculations have shown that disorder is detrimental to the electronic properties of GALs, as the band gap vanishes or is significantly lowered [23]. Transport calculations support this finding and show that leakage currents may form through disordered graphene antidot devices [24].

A promising method that can overcome the problems of disorder is to use bottom-up self-assembly for fabrication, which provides much better control of the formed structures. However, research utilizing bottom-up methods to fabricate graphene nanostructures is still in its infancy. Nonetheless, several groups have successfully synthesized various atomically precise nanostructures using such methods. Cai *et al.* [25] have fabricated GNRs and chevron-shaped GNRs, so-called graphene nanowiggles (GNWs), using surface-assisted coupling of two different precursors on an Au(111) surface followed by cyclodehydrogenation. This yielded narrow, fairly long GNRs and GNWs on the surface. Modified versions of the GNW precursor with pyridinelike nitrogen at one or two sites have been used by Bronner *et al.* [26] to fabricate doped GNWs. Later, Cai *et al.* [27] used these precursors to fabricate GNW heterojunctions and heterostructures by changing between pristine and doped precursors during synthesis. These structures were recently studied theoretically by Lherbier *et al.* [28], who reported reasonably high mobilities as well as charge carrier separation. Two-dimensional structures have also been prepared using bottom-up procedures. A nitrogenated GAL with C_2N stoichiometry has been synthesized by Mahmood *et al.* [29] via a wet-chemical technique, producing a network of aromatic rings with nitrogen between them, where they measured a band gap of 1.96 eV. Sánchez-Sánchez *et al.* [30] utilized cyclodehydrogenation to produce BN-substituted heteroaromatic networks from another precursor. Finally, Bieri *et al.* [31] have used the precursor hexaiodo-substituted macrocycle cyclohexa-m-phenylene (CHP) to produce a GAL on an Ag(111) surface with subnanometer periodicity. These new results on bottom-up techniques for producing atomically precise and even doped graphene structures bring hope that graphene could be used for semiconductor electronics. Despite the high level of control on the atomic scale, these methods have some drawbacks as well. The domain size is still limited, and the synthesis takes place on metallic surfaces, requiring the structures to be transferred after fabrication. However, further optimization of the synthesis could improve the structures for device feasibility.

As mentioned above, doping has been actively pursued in graphene nanostructures in order to fabricate, e.g., junctions for device application. Usual dopants are boron and nitrogen,

as they fit in the lattice easily, but other types of doping have also been studied, such as aluminum, sulfur, and phosphorus [32]. Nitrogen doped graphene has been synthesized by several groups from methods such as chemical vapor deposition (CVD) on copper using methane and ammonia [33] or CVD on nickel using triazine [34]. The transport properties of boron or nitrogen doped graphene were studied theoretically by Lherbier *et al.* [35], while the effect of unbalanced sublattice nitrogen doping was studied by Lherbier and other co-workers [36]. Isolated boron and nitrogen doping in graphene and near graphene edges has also been studied theoretically [37,38]. Nitrogen doped carbon nanotubes [39] and GNRs [40] have been realized experimentally, and doped GNRs have been studied theoretically to a large extent [6,41–43]. It was shown that the most stable configuration of boron and nitrogen doping is at the edges of the nanoribbon and that nitrogen doping can be either pyridine or pyridiniumlike. Scanning Raman spectroscopy has indicated *p*-type doping in GALs after fabrication from electron-beam lithography and oxygen reactive ion etching [44]. These GALs were similar to other top-down fabricated ones, and it was suggested that the doping stems from the patterning process.

In this paper we study the effect of introducing doping in the GAL synthesized by Bieri *et al.* [31] in the form of boron or nitrogen impurities. As pointed out by Sánchez-Sánchez *et al.* [30], the method of cyclodehydrogenation may be extended to more complex systems, provided the precursor can be synthesized. For our study, we assume that a precursor similar to CHP used by Bieri *et al.* [31] can be synthesized, the only difference being that one of the inner carbons of each molecule is replaced by a nitrogen or boron impurity. We study the electronic properties of these structures using density functional theory (DFT) and employ a tight-binding (TB) parametrization to study the case of more dilute doping. Additionally, a Green's function formalism is used to determine the activation energy for isolated dopants at a low computational cost. We also introduce impurities randomly and compare the density of states (DOS) with the ordered case to determine the effect of disorder. To our knowledge, there has been no theoretical work on doped GALs, and we thus report the first theoretical evidence of *p*- and *n*-type GAL semiconductors.

II. THEORY AND METHODS

The atomic structure of the pristine GAL used in our study is shown in Fig. 1(a), where the dashed red lines mark the primitive unit cells. The properties of GALs have been studied theoretically by several groups [12,23,45–52]. In the notation in Ref. [48], the one synthesized by Bieri *et al.* is a rotated GAL (RGAL). It turns out that two thirds of RGALs are semimetals, while every third is a semiconductor. Petersen *et al.* [48] have presented a rule based on structural parameters determining if an RGAL is a semimetal or semiconductor and, according to their rule, the antidot lattice described here is semiconducting. Here we will not study doping in other types of antidot lattices than the experimentally realized one in Fig. 1(a). Therefore, we refer to this type of antidot lattice simply as GAL through the rest of the paper.

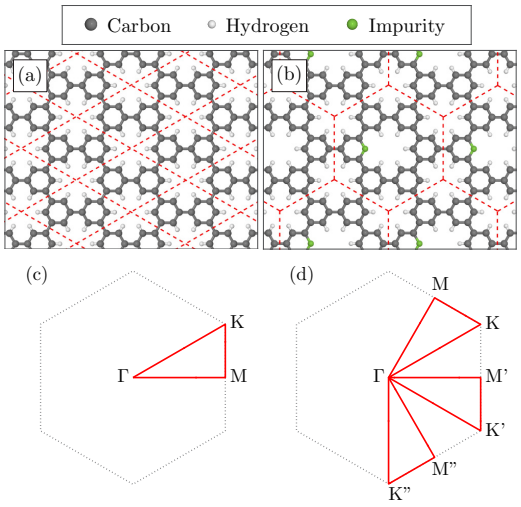

FIG. 1. Structural unit cells and corresponding Brillouin zones of the GALs studied in this paper. (a) Unit cell of the pristine system and (c) its Brillouin zone and k path for the band structure. (b) Unit cell for a doped system (in the case of no hydrogen termination at the impurity) with (d) the k path for this structure.

We construct the doped systems from modified CHP molecules, where one carbon atom on the inner edge of the molecule is replaced with either boron or nitrogen. We choose the edge site, as this has been shown to be the most stable site for doping in GNRs [6,42,43]. An example of the structure for this unit cell is shown in Fig. 1(b). The figure also shows the Brillouin zones and corresponding band structure k paths for both the pristine and doped systems. Because of broken symmetry in the unit cell containing an impurity, the route for the band structure is different than for the pristine system. We place the impurity at an edge site and vary the hydrogen termination between zero, one, and two hydrogens at the impurity. Previously, Huang *et al.* [53] have made theoretical studies of boron and nitrogen doping at graphene edges and shown that the favorable termination for edge doping is one hydrogen (pyridiniumlike) both for boron and nitrogen doping. However, Wang *et al.* [43] have shown that the most stable configuration may be changed to no hydrogen at the impurity (pyridinelike) by varying the ratio between monohydrogenated and dihydrogenated edge carbon. This suggests that the synthesis may be controlled to yield different degrees of hydrogenation at the impurity, for which reason we choose to study all three kinds of hydrogen termination. Doped structures are studied in the fully ordered configuration, meaning that all precursor molecules are oriented in the same direction. Systems with more dilute doping are also studied, for which some molecules are left undoped. We realize that the orientation would be random for practical synthesis, but we focus on ordered cases to keep the computational cost manageable. All structures are planar except for those with dihydrogenated impurities, where only the two hydrogen atoms on the impurity are out of the plane.

The pristine and fully ordered doped GALs are studied via DFT using the ABINIT package [54–57], in which a plane-wave basis set is used to expand the wave function. We use the Perdew-Burke-Ernzerhof generalized gradient approximation (PBE-GGA) functional [58] and the projector augmented wave (PAW) method [59] to solve for the eigenstates of the systems. We use a plane-wave cutoff energy of nearly 600 eV together with an $11\times11\times1$ Monkhorst-Pack k-grid sampling. The distance between the layers is 10 Å in order to decouple them electronically, and we use a fairly low Fermi smearing of 68 meV. We perform full structural relaxation of all unit cells before calculating band structures. The structures are relaxed until the maximum force is less than 2.6 meV/Å. We have found that these parameters provide sufficient convergence together with a tolerable computational effort.

In order to investigate the effects of more dilute doping, we employ a π-orbital TB model to describe the system, meaning that we concentrate on the electronic processes arising from hopping between the p_z orbitals at each carbon/impurity atom, and disregard bands arising from other orbitals further removed in energy from the Fermi level. The Hamiltonian of the pristine system is given by

$$\mathbf{H}_0 = \sum_i \varepsilon_p |i\rangle\langle i| + \sum_{i,j} t_{ij} |i\rangle\langle j|, \tag{1}$$

where ε_p is the carbon on-site energy and t_{ij} is the hopping integral between atoms i and j. We include interactions up to third-nearest neighbors and allow for nonorthogonality in the overlap matrix $\mathbf{S}$. The impurity is modeled solely by shifting the on-site potential on the impurity with respect to ε_p. The impurity Hamiltonian, which must be added to Eq. (1), then becomes $\mathbf{H}_1 = \Delta|l\rangle\langle l|$, where the impurity is located at site l and Δ is the shift of the on-site potential. Other reports include a change in the hopping integral between the impurity and up to its third-nearest neighbors [28,36]. However, we find that this only changes the fit marginally.

We begin by calculating the band structure of the pristine system using DFT and obtaining the optimal TB parametrization. The fit is carried out using the three valence and three conduction bands closest to the Fermi level. Figure 2 shows that the DFT band structure can be fitted with excellent agreement by this TB parametrization. We find it necessary to include third-nearest neighbors in a nonorthogonal model for the fit to be in good agreement with DFT. The parameters for the TB model are listed in the table in Fig. 2. Here subscripts 1, 2, and 3 denote nearest, second-nearest, and third-nearest neighbors, respectively. The structure is a semiconductor, consistent with the rule presented in Ref. [48], and has a rather large band gap of 2.30 eV. This is good agreement with previous DFT calculations for the same structure, i.e., 2.34 eV [60] and 2.48 eV [61]. For reference, we have also fitted the band structure of pristine graphene to this TB model and, again, find excellent agreement. Moreover, the obtained parameters are in good agreement with those reported by Grüneis *et al.* [62].

Having an accurate TB parametrization of the electronic structure allows us to efficiently employ a Green's function formalism to analyze the doping level in the case of completely isolated dopants. This formalism for nonorthogonal models

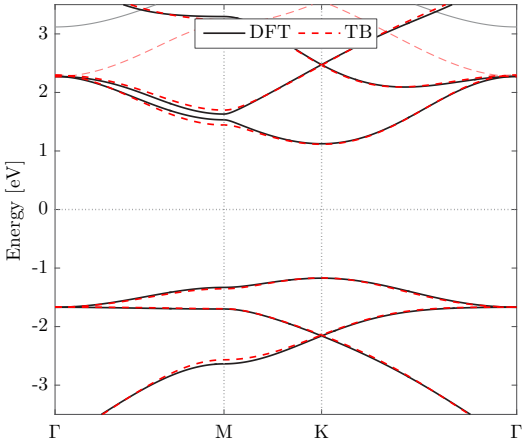

ε_p	t_1	t_2	t_3	s_1	s_2	s_3
-2.18	-2.58	-1.11	-0.29	0.36	0.08	0.07

FIG. 2. Band structure of the pristine GAL shown in Fig. 1(a), calculated using DFT. The best third-nearest neighbor nonorthogonal TB parametrization is also shown. Full colors/lines show the bands used for the TB fit, while weak colors/lines show the rest of the band structures. The TB parameters are listed in the table, where the on-site energy and hopping integrals are in units of eV.

was previously developed and used to describe bulk and edge doping in graphene, see Refs. [37,38] for further details on the derivation. Although the Green's functions in these papers are simplified due to the nearest neighbor TB model employed, Green's functions may be calculated for nonorthogonal TB models with an arbitrary number of neighbors. Therefore, we may use this formalism together with our third-nearest neighbor model as well. The theory shows that modeling the impurity by only adjusting its on-site potential yields the following particularly simple expression for the impurity perturbed Green's function at lattice site l:

$$\mathbf{G}_{ll}(z) = \frac{\mathbf{G}^0_{ll}(z)}{1 - \Delta\widetilde{\mathbf{G}}^0_{ll}(z)}, \tag{2}$$

where the Green's functions are given by $\mathbf{G}_0(z) = (z - \mathbf{S}^{-1}\mathbf{H}_0)^{-1}$ and $\widetilde{\mathbf{G}}_0(z) = (z\mathbf{S} - \mathbf{H}_0)^{-1}$. For a semiconductor, the doping level shows up as a pole contribution in the band gap of the impurity local density of states (LDOS). In the limit of vanishing broadening, this approaches a Dirac delta function. The energy of this state, i.e., the doping level, may be evaluated in a simple manner by considering Eq. (2). The impurity LDOS is given by $L(\omega) = -\pi^{-1}\mathrm{Im}\{\mathbf{G}_{ll}(\omega)\}$, which diverges when $\mathrm{Re}\{\widetilde{\mathbf{G}}^0_{ll}(z)\} = 1/\Delta$ and $\mathrm{Im}\{\widetilde{\mathbf{G}}^0_{ll}(z)\} = 0$ are both satisfied. This means that the doping level may be determined by evaluating the Green's function, assuming the impurity on-site energy shift is known.

The above methods treat independent electrons only. The theory may be elaborated to include electron-electron interactions. This gives rise to a complex self-energy manifesting itself in a quasiparticle energy shift and a finite lifetime. This

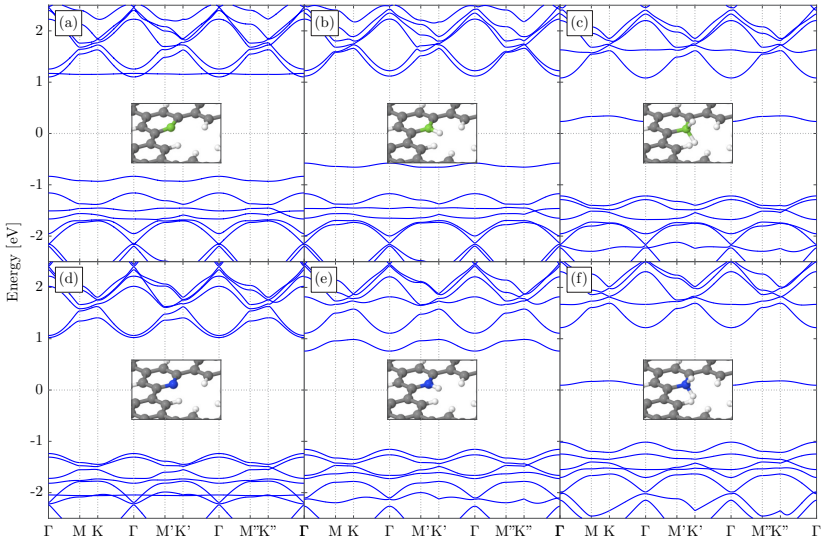

FIG. 3. DFT band structures of boron or nitrogen doped GALs for different hydrogen termination on the impurity. (a)–(c) Boron doping and (d)–(f) show nitrogen doping, in both cases terminated by zero, one, and two hydrogen atoms at the impurity, respectively.

was studied in Ref. [38], where it was found that the occupancy changes marginally for nitrogen doping and up to a few percent for boron doping. Because the changes are so small, we restrict our analysis to treat independent electrons only.

III. RESULTS

We now proceed to study the effect of replacing one edge carbon in the unit cell with either a boron or nitrogen atom as illustrated in Fig. 1(b). Figure 3 shows DFT band structures for both boron and nitrogen doped GALs with different hydrogen termination. From the top panels, we see that, as expected, boron doping introduces an acceptor level near the highest valence band, which moves closer to the conduction bands as the number of hydrogen atoms on the impurity increases. In the case of two hydrogen atoms, the doping level has even moved across the Fermi level of the pristine structure. Similarly, nitrogen doping introduces a donor level close to the lowest conduction band which moves towards the valence bands as the number of hydrogen atoms at the impurity increases. In the case of no impurity hydrogenation, the doping level is very close to the conduction band edge. Furthermore, we note that the remaining band structure does not change appreciably.

We use the parametrization of the pristine system as the basis for the TB model describing the perturbed systems. In our effort to make a good, yet simple model for the perturbed systems, we model the impurity by only adjusting the on-site element at the impurity site, making Δ the only fitting parameter for the perturbed systems. Examples of fits for boron and nitrogen doping, both terminated by one hydrogen (corresponding to Figs. 3(b) and 3(e), respectively), are shown in Fig. 4. In the fit we include only the two valence (conduction) bands closest to the Fermi level for boron (nitrogen) doping. The fits demonstrate that such a simple model still yields a very good description of the bands in the vicinity of the Fermi energy for both types of doping. The fitted values of Δ are listed in Table I. Only for boron terminated by two hydrogen atoms were we unable to obtain a satisfactory fit. From the trend of nitrogen doping and boron with lower degrees of hydrogenation, we expect the on-site energy shift to be large for boron terminated by two hydrogen. This suggests that the correction from electron-electron interactions due to a complex self-energy could be more significant. However, especially for low values of the on-site energy shift as found for most of the systems studied here, the correction will be small [38].

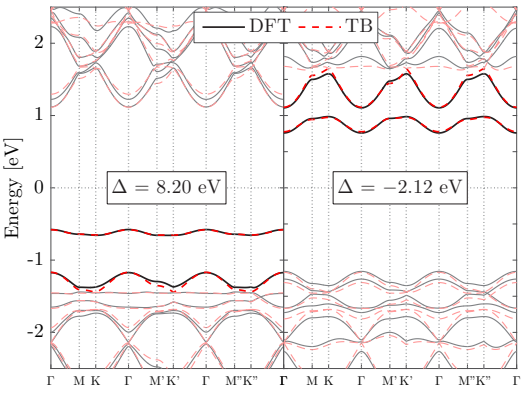

FIG. 4. DFT and fitted TB band structures of boron (left) and nitrogen (right) doped GALs, both terminated by one hydrogen atom at the impurity. Full colors/lines show the bands used for the TB fit, while weak colors/lines show the rest of the band structure.

TABLE I. Fitted values of Δ for boron and nitrogen doping and for different hydrogen terminations at the impurity.

Impurity hydrogenation	0	1	2
Boron Δ (eV)	3.22	8.20	–
Nitrogen Δ (eV)	−0.88	−2.12	−6.94

The unit cells in Fig. 1(b) used for the DFT calculations are relatively small and place the impurities only 12.8 Å apart. This is also evident from the significant dispersion of the impurity bands seen in the band structures of Fig. 3. The TB parametrization allows us to go comfortably beyond that, and calculate band structures for supercells consisting of $N\times N$ precursor unit cells, where each supercell contains only one impurity. Specifically, we study the doping level as the doping concentration decreases. Figure 5 shows band structures of 1×1, 2×2, and 3×3 supercells containing only one impurity for which $\Delta = -2$ eV. It is clear that the midgap impurity band becomes increasingly flatter as the cell size increases. In this case, a 3×3 supercell is enough to get a nearly dispersionless impurity band. However, for values of Δ closer to zero, the convergence is worse and a much larger cell is required. This is not surprising because the extent of the wave function associated with these impurity levels is determined by their distance to the nearest band and, consequently, shallower donors/acceptors tend to be hybridized over larger spatial scales. Note that the most striking impact of changing the supercell size takes place in the impurity band. The denser nature of the conduction and valence bands as we go from Figs. 5(a) to 5(c) is simply due to band folding, as the unit cell size is increased.

Once the doping level in the TB band structure is sufficiently flat, we are able to determine the activation energy of the system. However, we may also calculate the doping level of completely isolated impurities using the Green's function technique described in Sec. II. The local Green's function at the impurity site is shown in Fig. 6, where the band gap is clearly seen as the region where the imaginary part is zero. The real

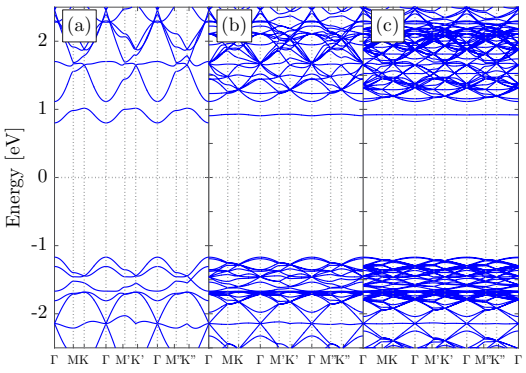

FIG. 5. TB band structures of supercells containing (a) 1×1, (b) 2×2, and (c) 3×3 precursor unit cells [see Fig. 1(b)] with only one impurity per supercell. The impurity is modeled using $\Delta = -2$ eV.

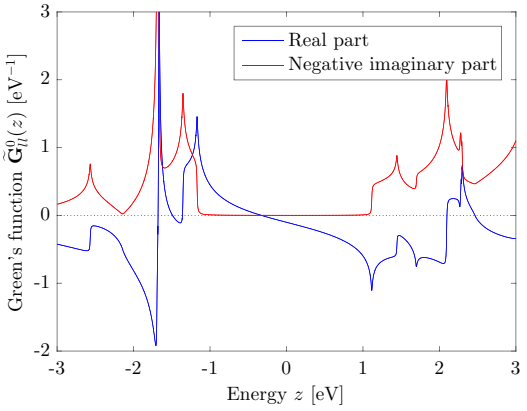

FIG. 6. Green's function for the impurity site of the GAL with a broadening of 5 meV.

part of the Green's function is used to calculate the activation energy. For negative values of Δ (corresponding to n-type doping), the activation energy is given by $E_A = E_c - E_d$, while it is $E_A = E_d - E_v$ for positive values (corresponding to p-type doping). Here E_d refers to the energy of the doping level, while E_v and E_c are the highest (lowest) energy of the valence (conduction) bands, respectively. The doping level is found by solving $\mathrm{Re}\{\widetilde{\mathbf{G}}^0_{ll}(z)\} = 1/\Delta$ for the energy z within the band gap region. This calculation is very fast when a converged Green's function is provided. Due to the relatively simple structure of the pristine GAL, calculating the Green's function is computationally straightforward. The activation energy as a function of Δ is shown in Fig. 7, where the fitted values from Table I are marked with green asterisks. The activation energies from the supercell band structures are also

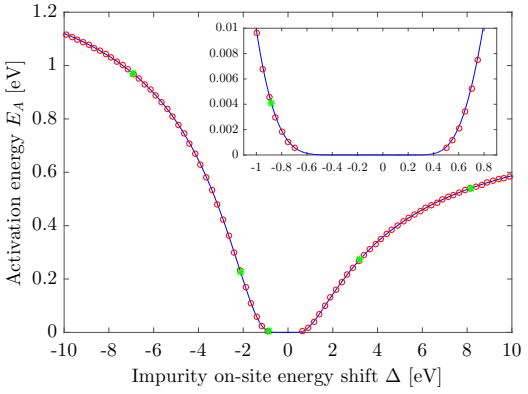

FIG. 7. Activation energy for different values of the impurity on-site shift Δ, where the Green's function method (solid blue line) is compared with the supercell band structure method (red circles). The actual values of Δ obtained *ab initio* and listed in Table I are also shown (green asterisks).

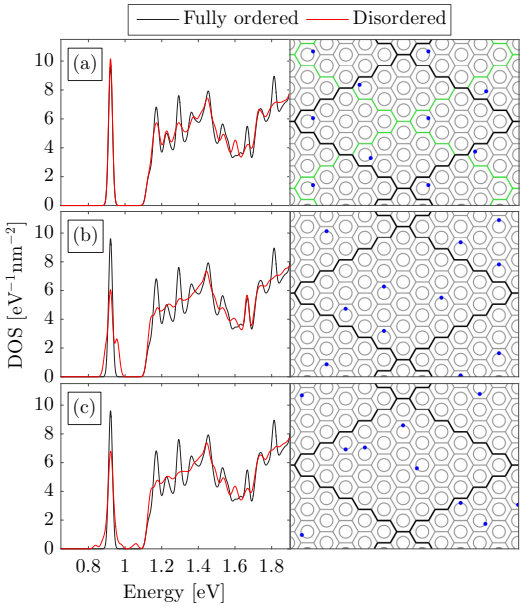

FIG. 8. Density of states using TB for doped GALs with various types of disorder. The unit cell in (a), marked by black lines, consists of four 3×3 subcells (green lines), each with a doped molecule at a fixed position with random orientation. (b) Fixed orientation and random position, while (c) is both random position and orientation. Disordered results are averages from numerous random configurations. All calculations are for $\Delta = -2$ eV with a broadening of 25 meV.

shown, although we emphasize that this latter method is much more computationally demanding, as several band structures have to be calculated for each value of Δ. Furthermore, a dispersionless impurity level requires very large supercells for values of Δ close to zero, making them extremely time consuming. The results from the supercell band structures (red circles) are in excellent agreement with the curve obtained using the Green's function method, thus verifying the result. Because of the slow convergence for Δ close to zero, the supercell method has only been used for values outside the ± 0.5 eV regime. This is shown in the inset of the figure, where the agreement is seen to continue for all the values provided. We also note that nitrogen doping with no impurity hydrogenation results in a very low activation energy of 4.1 meV.

In this paper we have focused on very dilute and ordered doping in GALs. However, in an experiment, the doped molecules are not expected to be evenly separated or ordered. Therefore, we study the effect of introducing various types of disorder in moderately doped systems. Figure 8 shows the density of states (DOS) for various types of disorder in a GAL, where one out of nine molecules contain an impurity, meaning that 0.31% of the carbon atoms are replaced by impurities. We consider three types of disorder: (a) fixed position and random orientation, (b) random position and fixed orientation, and (c) full disorder with both random position and orientation. For the first type of disorder (a), the impurities are never close together and their coupling is therefore weak. The average DOS for the disordered structures shows a peak at the doping level that is nearly identical to the ordered case and a slightly smoothed curve for other energies. In the case of random position and fixed orientation (b), the dopants may be much closer and a broadening of the peak is observed. Notably, the peak is broadened more to the right, where a small peak is observed, which is attributed to the cases where doped molecules are adjacent. Full disorder (c) introduces two smaller peaks on either side of the main peak. However, for this doping concentration, these peaks are much smaller than the main peak. The extra peak in (b) is not observed for full disorder. Impurities in adjacent molecules in (b) will always be separated by the same distance, giving rise to a more pronounced feature in the DOS, whereas the distance between impurities in adjacent molecules in (c) may take several different values because of random orientation. This causes the disorder in (b) to seemingly affect the peak more than in (c) even though the type of disorder in (c) resembles the expected result from experiments more. The results from Fig. 8 show that introducing doped molecules randomly in an otherwise pristine lattice only affects the doping properties to a small extent.

The above results point to the advantage of using the Green's function method even when the system is not in the strictly dilute limit. Its application is not limited in any way to the specific structure we considered here, and is applicable to any system of dilute impurities in a crystal lattice, such as other antidot lattice geometries, provided an accurate TB model is available. We are convinced that our analysis of the properties of doped GALs will be useful for future studies of electronic and transport properties of junctions in graphene nanostructures.

IV. CONCLUSION

We have studied the effect of substituting an edge carbon atom in a GAL with either boron or nitrogen. By means of DFT, we calculate electronic band structures for GALs where the impurity is terminated by zero, one, or two hydrogen atoms. We perform TB parametrizations describing both the pristine and doped systems with high accuracy, which are used together with a Green's function method to study more dilute doping. Boron doping introduces an acceptor level near the valence band edge, which moves towards the conduction bands as the hydrogenation on the impurity increases. Similarly, nitrogen introduces a donor level near the conduction band, which moves towards the valence bands with increasing hydrogenation. This indicates that the properties of doped GALs may be tuned, provided the impurity hydrogenation is controllable during synthesis, as suggested in Ref. [43]. Furthermore, we studied the effect of disorder at moderate doping concentration and found that such systems are fairly robust against disorder. Our work is the first step on the way to understanding doping in GALs. We believe that the parametrizations reported here, together with the activation energy analysis, are useful tools for further studies of this and other types of doped GALs.

ACKNOWLEDGMENTS

S.J.B. and T.G.P. gratefully acknowledge the financial support from the Center for Nanostructured Graphene (Project No. DNRF103) financed by the Danish National Research Foundation and from the QUSCOPE project financed by the Villum Foundation. S.J.B. further acknowledges the hospitality and support of the NUS Centre for Advanced 2D Materials, where part of this research was conducted. V.M.P. acknowledges the support by the National Research Foundation (Singapore) through the CRP grant "Novel 2D materials with tailored properties: beyond graphene" (R-144-000-295-281).

[1] K. S. Novoselov, A. K. Geim, S. Morozov, D. Jiang, Y. Zhang, S. Dubonos, I. Grigorieva, and A. Firsov, Science **306**, 666 (2004).
[2] K. Novoselov, D. Jiang, F. Schedin, T. Booth, V. Khotkevich, S. Morozov, and A. Geim, Proc. Natl. Acad. Sci. USA **102**, 10451 (2005).
[3] K. I. Bolotin, K. Sikes, Z. Jiang, M. Klima, G. Fudenberg, J. Hone, P. Kim, and H. Stormer, Solid State Commun. **146**, 351 (2008).
[4] R. Nair, P. Blake, A. Grigorenko, K. Novoselov, T. Booth, T. Stauber, N. Peres, and A. Geim, Science **320**, 1308 (2008).
[5] C. Lee, X. Wei, J. W. Kysar, and J. Hone, Science **321**, 385 (2008).
[6] B. Huang, Q. Yan, G. Zhou, J. Wu, B.-L. Gu, W. Duan, and F. Liu, Appl. Phys. Lett. **91**, 253122 (2007).
[7] B. Obradovic, R. Kotlyar, F. Heinz, P. Matagne, T. Rakshit, M. Giles, M. Stettler, and D. Nikonov, Appl. Phys. Lett. **88**, 142102 (2006).
[8] Y.-W. Son, M. L. Cohen, and S. G. Louie, Phys. Rev. Lett. **97**, 216803 (2006).
[9] M. Y. Han, B. Özyilmaz, Y. Zhang, and P. Kim, Phys. Rev. Lett. **98**, 206805 (2007).
[10] R. Balog, B. Jørgensen, L. Nilsson, M. Andersen, E. Rienks, M. Bianchi, M. Fanetti, E. Lægsgaard, A. Baraldi, S. Lizzit *et al.*, Nat. Mater. **9**, 315 (2010).
[11] J. G. Pedersen and T. G. Pedersen, Phys. Rev. B **85**, 235432 (2012).
[12] T. G. Pedersen, C. Flindt, J. Pedersen, N. A. Mortensen, A.-P. Jauho, and K. Pedersen, Phys. Rev. Lett. **100**, 136804 (2008).
[13] J. Eroms and D. Weiss, New J. Phys. **11**, 095021 (2009).
[14] J. Bai, X. Zhong, S. Jiang, Y. Huang, and X. Duan, Nat. Nanotech. **5**, 190 (2010).
[15] X. Liang, Y.-S. Jung, S. Wu, A. Ismach, D. L. Olynick, S. Cabrini, and J. Bokor, Nano Lett. **10**, 2454 (2010).
[16] M. Kim, N. S. Safron, E. Han, M. S. Arnold, and P. Gopalan, Nano Lett. **10**, 1125 (2010).
[17] A. J. M. Giesbers, E. C. Peters, M. Burghard, and K. Kern, Phys. Rev. B **86**, 045445 (2012).
[18] F. Oberhuber, S. Blien, S. Heydrich, F. Yaghobian, T. Korn, C. Schüller, C. Strunk, D. Weiss, and J. Eroms, Appl. Phys. Lett. **103**, 143111 (2013).
[19] D. A. Areshkin, D. Gunlycke, and C. T. White, Nano Lett. **7**, 204 (2007).
[20] E. R. Mucciolo, A. H. Castro Neto, and C. H. Lewenkopf, Phys. Rev. B **79**, 075407 (2009).
[21] D. V. Kosynkin, A. L. Higginbotham, A. Sinitskii, J. R. Lomeda, A. Dimiev, B. K. Price, and J. M. Tour, Nature (London) **458**, 872 (2009).
[22] L. Jiao, L. Zhang, X. Wang, G. Diankov, and H. Dai, Nature (London) **458**, 877 (2009).
[23] S. Yuan, R. Roldán, A.-P. Jauho, and M. I. Katsnelson, Phys. Rev. B **87**, 085430 (2013).
[24] S. R. Power and A.-P. Jauho, Phys. Rev. B **90**, 115408 (2014).
[25] J. Cai, P. Ruffieux, R. Jaafar, M. Bieri, T. Braun, S. Blankenburg, M. Muoth, A. P. Seitsonen, M. Saleh, X. Feng *et al.*, Nature (London) **466**, 470 (2010).
[26] C. Bronner, S. Stremlau, M. Gille, F. Brauße, A. Haase, S. Hecht, and P. Tegeder, Angew. Chem., Int. Ed. Engl. **52**, 4422 (2013).
[27] J. Cai, C. A. Pignedoli, L. Talirz, P. Ruffieux, H. Söde, L. Liang, V. Meunier, R. Berger, R. Li, X. Feng *et al.*, Nat. Nanotech. **9**, 896 (2014).
[28] A. Lherbier, L. Liang, J.-C. Charlier, and V. Meunier, Carbon **95**, 833 (2015).
[29] J. Mahmood, E. K. Lee, M. Jung, D. Shin, I.-Y. Jeon, S.-M. Jung, H.-J. Choi, J.-M. Seo, S.-Y. Bae, S.-D. Sohn *et al.*, Nat. Commun. **6**, 6486 (2015).
[30] C. Sánchez-Sánchez, S. Brüller, H. Sachdev, K. Müllen, M. Krieg, H. F. Bettinger, A. Nicolaï, V. Meunier, L. Talirz, R. Fasel *et al.*, ACS Nano **9**, 9228 (2015).
[31] M. Bieri, M. Treier, J. Cai, K. Aït-Mansour, P. Ruffieux, O. Gröning, P. Gröning, M. Kastler, R. Rieger, X. Feng *et al.*, Chem. Commun. **45**, 6919 (2009).
[32] H. Terrones, R. Lv, M. Terrones, and M. S. Dresselhaus, Rep. Prog. Phys. **75**, 062501 (2012).
[33] D. Wei, Y. Liu, Y. Wang, H. Zhang, L. Huang, and G. Yu, Nano Lett. **9**, 1752 (2009).
[34] D. Usachov, O. Vilkov, A. Gruneis, D. Haberer, A. Fedorov, V. Adamchuk, A. Preobrajenski, P. Dudin, A. Barinov, M. Oehzelt *et al.*, Nano Lett. **11**, 5401 (2011).
[35] A. Lherbier, X. Blase, Y.-M. Niquet, F. Triozon, and S. Roche, Phys. Rev. Lett. **101**, 036808 (2008).
[36] A. Lherbier, A. R. Botello-Mendez, and J.-C. Charlier, Nano Lett. **13**, 1446 (2013).
[37] T. G. Pedersen and J. G. Pedersen, Phys. Rev. B **87**, 155433 (2013).
[38] T. G. Pedersen, Phys. Rev. B **91**, 085428 (2015).
[39] R. Czerw, M. Terrones, J.-C. Charlier, X. Blase, B. Foley, R. Kamalakaran, N. Grobert, H. Terrones, D. Tekleab, P. Ajayan *et al.*, Nano Lett. **1**, 457 (2001).
[40] X. Wang, X. Li, L. Zhang, Y. Yoon, P. K. Weber, H. Wang, J. Guo, and H. Dai, Science **324**, 768 (2009).
[41] Q. Yan, B. Huang, J. Yu, F. Zheng, J. Zang, J. Wu, B.-L. Gu, F. Liu, and W. Duan, Nano Lett. **7**, 1469 (2007).
[42] Y. Li, Z. Zhou, P. Shen, and Z. Chen, ACS Nano **3**, 1952 (2009).
[43] X. Wang, Z. Hou, T. Ikeda, S.-F. Huang, K. Terakura, M. Boero, M. Oshima, M.-a. Kakimoto, and S. Miyata, Phys. Rev. B **84**, 245434 (2011).
[44] S. Heydrich, M. Hirmer, C. Preis, T. Korn, J. Eroms, D. Weiss, and C. Schüller, Appl. Phys. Lett. **97**, 043113 (2010).

[45] J. A. Fürst, J. G. Pedersen, C. Flindt, N. A. Mortensen, M. Brandbyge, T. G. Pedersen, and A.-P. Jauho, New J. Phys. **11**, 095020 (2009).
[46] R. Petersen and T. G. Pedersen, Phys. Rev. B **80**, 113404 (2009).
[47] M. Vanević, V. M. Stojanović, and M. Kindermann, Phys. Rev. B **80**, 045410 (2009).
[48] R. Petersen, T. G. Pedersen, and A.-P. Jauho, ACS Nano **5**, 523 (2010).
[49] M. Dvorak, W. Oswald, and Z. Wu, Sci. Rep. **3** 2289 (2013).
[50] M. L. Trolle, U. S. Møller, and T. G. Pedersen, Phys. Rev. B **88**, 195418 (2013).
[51] S. J. Brun, M. R. Thomsen, and T. G. Pedersen, J. Phys.: Condens. Matter **26**, 265301 (2014).
[52] M. R. Thomsen, S. J. Brun, and T. G. Pedersen, J. Phys.: Condens. Matter **26**, 335301 (2014).
[53] S.-F. Huang, K. Terakura, T. Ozaki, T. Ikeda, M. Boero, M. Oshima, J.-i. Ozaki, and S. Miyata, Phys. Rev. B **80**, 235410 (2009).
[54] X. Gonze, J.-M. Beuken, R. Caracas, F. Detraux, M. Fuchs, G.-M. Rignanese, L. Sindic, M. Verstraete, G. Zerah, F. Jollet *et al.*, Comput. Mater. Sci. **25**, 478 (2002).
[55] X. Gonze, B. Amadon, P.-M. Anglade, J.-M. Beuken, F. Bottin, P. Boulanger, F. Bruneval, D. Caliste, R. Caracas, M. Cote *et al.*, Comput. Phys. Commun. **180**, 2582 (2009).
[56] F. Bottin, S. Leroux, A. Knyazev, and G. Zérah, Comput. Mater. Sci. **42**, 329 (2008).
[57] M. Torrent, F. Jollet, F. Bottin, G. Zérah, and X. Gonze, Comput. Mater. Sci. **42**, 337 (2008).
[58] J. P. Perdew, K. Burke, and M. Ernzerhof, Phys. Rev. Lett. **77**, 3865 (1996).
[59] G. Kresse and D. Joubert, Phys. Rev. B **59**, 1758 (1999).
[60] A. Du, Z. Zhu, and S. C. Smith, J. Am. Chem. Soc. **132**, 2876 (2010).
[61] Y. Li, Z. Zhou, P. Shen, and Z. Chen, Chem. Commun. **46**, 3672 (2010).
[62] A. Grüneis, C. Attaccalite, L. Wirtz, H. Shiozawa, R. Saito, T. Pichler, and A. Rubio, Phys. Rev. B **78**, 205425 (2008).

ISSN (online): 2246-1248
ISBN (online): 978-87-7112-806-2

AALBORG UNIVERSITY PRESS